Spring 1993

Grid Sensitivity for Aerodynamic Optimization and Flow Analysis

Ideen Sadrehaghighi
Old Dominion University

GRID SENSITIVITY FOR AERODYNAMIC OPTIMIZATION AND FLOW ANALYSIS

by
Ideen Sadrehaghighi
B.S., May 1983, Department of Mechanical Engineering and Mechanics
Old Dominion University, Norfolk, Virginia
M.E., December 1986, Department of Mechanical Engineering and Mechanics
Old Dominion University, Norfolk, Virginia

A Dissertation Submitted to the Faculty of Old Dominion University in Partial Fulfillment of the Requirements for the Degree of

DOCTOR OF PHILOSOPHY
MECHANICAL ENGINEERING
OLD DOMINION UNIVERSITY
May, 1993

Approved by:

Dr. Surendra N. Tiwari (Director)

Dr. Robert E. Smith

Dr. Arthur C. Taylor III

Dr. John J. Swetits

Dr. Gene J.W. Hou

ABSTRACT

GRID SENSITIVITY FOR AERODYNAMIC OPTIMIZATION AND FLOW ANALYSIS

Ideen Sadrehaghighi
Old Dominion University, 1993
Director: Dr. Surendra N. Tiwari

An algorithm is developed to obtain the grid sensitivity with respect to design parameters for aerodynamic optimization. Two distinct parameterization procedures are developed for investigating the grid sensitivity with respect to design parameters of a wing-section as an example. The first procedure is based on traditional (physical) relations defining NACA four-digit wing-sections. The second is advocating a novel (geometrical) parameterization using spline functions such as NURBS (Non-Uniform Rational B-Splines) for defining the wing-section geometry. An interactive algebraic grid generation technique, known as Two-Boundary Grid Generation (TBGG) is employed to generate C-type grids around wing-sections. The grid sensitivity of the domain with respect to design and grid parameters has been obtained by direct differentiation of the grid equations. A hybrid approach is proposed for more geometrically complex configurations. A comparison of the sensitivity coefficients with those obtained using a finite-difference approach is made to verify the feasibility of the approach. The aerodynamic sensitivity coefficients are obtained using the compressible two-dimensional thin-layer Navier-Stokes equations. An optimization package has been introduced into the algorithm in order to optimize the wing-section surface using both physical and geometric parameterization. Results demonstrate a substantially improved design, particularly in the geometric parameterization case.

ACKNOWLEDGEMENTS

I would like to take this opportunity to express my appreciation to my advisors Dr. Surendra N. Tiwari of Old Dominion University and Dr. Robert E. Smith of NASA Langley Research Center for their valuable guidance and support during the entire course of this study. Special thanks are also extended to members of my dissertation committee for their assistance and suggestions. I also extend my appreciation to Mr. Eric L. Everton of NASA Langley and Mr. Vamshi M. Korivi of Old Dominion University for their assistance in various stages of this investigation. Further, I wish to thank Dr. Jamshid S. Abolhassani, Dr. Michael K. Bockelie, and Mr. John E. Stewart of Computer Sciences Corperation for their suggestions and guidance throughout this investigation . This work was supported by the NASA Langley Research Center through Cooperative Agreement NCC1 - 68 and Grant NAG-1-363.

TABLE OF CONTENTS

LIST OF TABLES

LIST OF FIGURES

LIST Of SYMBOLS

a = local speed of sound

B_i = stretching parameter

C = location of maximum camber

C_D = drag coefficient

C_f = skin friction coefficient

C_L = lift coefficient

C_P = pressure coefficient

C_X, C_Y = force coefficients in x and y directions

$\mathbf{D}_i$ = NURBS control point coordinate

e = energy per unit volume

F = physical model

f = objective function

G = dependent parameter

$\bar{\mathbf{F}}, \bar{\mathbf{G}}$ = inviscid fluxes

$\bar{\mathbf{G}}_v$ = viscous flux vector

g = optimization constraints

H = independent parameter

J = jacobian of transformation

K_1, K_2 = magnitude of orthogonality vectors

L = far-field boundary location

M = maximum camber

$\mathbf{M}$ = banded part of coefficient matrix

m = number of knots of a NURBS curve

M_∞ = free-stream Mach number

$N_{i,p}(r)$ = B-spline basis function

$\mathbf{N}$ = off-banded part of coefficient matrix

n = number of control points of NURBS

$\mathbf{n}$ = unit normal vector

$\mathbf{P}$ = vector of independent parameters

P_i = local pressure

p = degree of a NURBS curve

Pr = Prandtl number

$\mathbf{Q}$ = vector of field variables

$\mathbf{Q}^*$ = steady-state field variables

$R(r)$ = bottom boundary orthogonality vector

$\mathbf{R}$ = steady-state residual

$R_{i,p}(r)$ = NURBS basis function

$R^{\pm}$ = Riemann invariants

Re_∞ = free-stream Reynolds number

r = bottom boundary grid distribution

$\mathbf{r}$ = uniform knot vector of NURBS

s = top boundary grid distribution

$S(s)$ = top boundary orthogonality vector

$\bar{S}$ = vector of search direction

T = maximum thickness

t = grid stretching parameter

$\mathbf{U}$ = horizontal interpolant

U_∞ = free-stream velocity component

U, V = contravariant velocity vectors

u, v, w = velocity components in physical domain

$\mathbf{V}$ = vertical interpolant

$\mathbf{X}$ = vector of physical coordinates

$\mathbf{X}_B$ = vector of surface coordinates

$\mathbf{X}_D$ = vector of design parameters

$\mathbf{X}_G$ = vector of grid parameters

X_i, Y_i = control point coordinates

x, y, z = physical coordinates

x_1, y_1 = surface coordinates

x_2, y_2 = far-field boundary coordinates

y_c, y_T = camber and thickness curve ordinates

Greek Symbols

α = angle of attack

α_I^n = x-direction blending parameter

β_J^m = y-direction blending parameter

γ = scalar move parameter

δ = Kronecker delta

θ = surface slope

ξ, η, ζ = computational coordinates

ρ = density

ρ_∞ = free-stream density

$\sum$ = summation

τ_i = local shear stress

τ = viscous stress term

ω_i = NURBS curve weighting parameter

Chapter 1

INTRODUCTION

1.1 Motivation

Integrated design and optimization of airplane components has become a primary objective for most researchers in aerodynamic community. The sudden interest can be attributed to the introduction of complex and composite materials required by advanced aerospace vehicles, such as National AeroSpace Plane (NASP) and High Speed Civil Transport (HSCT) aircraft where, because of extreme flight conditions, the interdisciplinary interactions are particularly important. The process requires many analyses over a wide range of engineering disciplines. Each analysis is based on solving mathematical models describing physical laws associated with a discipline. For a vehicle confined to atmospheric flight conditions, the primary engineering disciplines are: aerodynamics, structures, control, and propulsion. These disciplines are interconnected and affect each other.

A Multidisciplinary Design Optimization (MDO) would provide the designer with sufficient information to predict the influence of a design parameter on all relevant disciplines. The traditional approach to MDO is to perform the analysis and optimization by each discipline in a sequential manner where one discipline uses the information from the preceding analysis of another discipline. This tedious and lengthy process, although acceptable for loosely-coupled systems, is likely to produce suboptimal results. For systems which are more tightly coupled, a relatively new approach is to perform the analysis and optimization at each discipline concurrently.

As opposed to a sequential approach, this technique supplies the designer with first order (i.e., derivative) information, thus enables him to to predict the influence of a design change on all the disciplines involved. The interaction among disciplines are achieved by a system of equations known as Global Sensitivity Equations (GSE), which communicate the system response due to design perturbations among all disciplines. On the local level, within each discipline, the Local Sensitivity Equations (LSE) are responsible for similar response. Both GSE and LSE are linear and algebraic, regardless of the mathematical nature of the governing equations associated with each discipline.

A complete design and optimization analysis using all the relevant disciplines is still a formidable task even for an isolated airplane component such as a wing or fuselage. The computational cost associated with such analysis can easily strain the capabilities of current supercomputers. The magnitude of this problem can be best appreciated when a discrete aerodynamic or structural design analysis can exhaust the computational capability of a medium size supercomputer. The underlying problem is the expensive cost of the analysis for each discipline involved. Clearly the aerodynamics involve non-linear physics and use of composite materials would require non-linear structural analysis as well. For a simple aero-elastic problem, the entire system matrix must be simultaneously solved using mostly implicit solvers. The extensive computational demand for such coupling of the governing equations, will likely limit MDO to only individual components such as a wing or wing-section. The cost of optimization operations are relatively small and manageable. Two general directions to overcome these difficulties have been proposed by different research groups. The first direction leads toward modifying the existing computational tools in order to obtain a relatively cheap and reliable technique for design and optimization. The usually favored direct solvers with all their advantages, require extremely large computer storage even for 2D applications.

Recent efforts concentrated on development and implementation of efficient iterative techniques and improvement of existing ones. The conditioning of the coefficient matrix, resulting from linearization of the governing equations, are prone to affect the convergence criteria and the propagation of error through the system. The second direction points to the advent of next generation of supercomputers with parallel processing capabilities. Parallel computing would be ideal for MDO analysis where each discipline could be assigned to a particular processor for greater efficiency. Consequently, the problem formulation and algorithm design (i.e., software development) should change in order to adapt to new computer architecture. Recognizing this need, the High Performance Computing and Communication Program (HPCCP) has been established by the federal government to confront such problems. This program is focused on developing the technology for TeraFLOP computing, an improvement of almost 1000 times over current technology.

For the present, a more realistic task would be to consider a discrete design and optimization model for simple configurations. The aerodynamic optimization, being an important component of MDO, has become an area of interest for many researchers. An essential element in design and optimization of aerodynamic surfaces is acquiring the sensitivity of functions of CFD solutions with respect to design parameters. Several methods concerning the derivation of sensitivity equations (LSE) are currently available. Among the most frequently mentioned are Direct Differentiation (DD), Adjoint Variable (AV), Symbolic Differentiation (SD), Automatic Differentiation (AD), and Finite Difference (FD). Each technique has its own unique characteristics. The Direct Differentiation, adopted in this study, has the advantage of being exact, due to direct differentiation of governing equations with respect to design parameters. The Adjoint Variable, having its roots in structural analysis, produces equally impressive results. For Symbolic Differentiation, a symbolic manipulator such as MACSYMA can be used to carry out these differentiations. Automatic Differen-

tiation, still at preliminary stages, exploits the fact that exact derivatives can be computed easily for all elementary arithmetic operations and intrinsic functions. The finite difference approach, simple and until recently the most popular, is based upon finite difference approximation of the derivatives. In this approach, a design parameter is perturbed from the nominal value, a new solution is obtained, and the difference between the new and old solution is used to obtain the sensitivity derivatives. This brute force technique has the disadvantage of being computationally intensive, especially when the number of parameters involved is large.

Design parameters can be classified according to whether or not they are coupled. Uncoupled design parameters influence the solution independently and would be the major contributors to optimization process. These parameters could be geometric, flow-dependent, or grid-dependent. The geometric design parameters specify the primary shape of a typical aerodynamic surface. Flow-dependent parameters are usually free-stream conditions such as free-stream Mach number or angle of attack. The grid-dependent parameters, relatively new in aerodynamic optimization, affect the interior and boundary grids; therefore, influencing the solution and optimization process. Traditionally, geometric parameters are considered the most affluent in aerodynamic optimization, although, optimization with respect to other design parameters is gaining respectability. For optimization with respect to geometric design parameters, a perturbation in parameters affect the surface grid and the field grid which, in turn, affect the flow-field solution. There are two basic components in obtaining aerodynamic sensitivity. They are: (1) obtaining the sensitivity of the governing equations with respect to the state variables, and (2) obtaining the sensitivity of the grid with respect to the design parameters. The sensitivity of the state variables with respect to the design parameters are described by a set of linear-algebraic relation. These systems of equations can be solved directly by a LU decomposition of the coefficient matrix. This direct inversion procedure becomes extremely expen-

sive as the problem dimension increases. A hybrid approach of an efficient banded matrix solver with influence of off-diagonal elements iterated can be implemented to overcome this difficulty.

1.2 Literature Survey

The literature on sensitivity analysis and optimization is quite extensive. The pioneering work on sensitivity analysis for MDO started with a plea from Sobieski [1,2][1] to the CFD community for extending their present capabilities to include sensitivity analysis of aerodynamic forces. Yates [3] developed an analytical approach using an implicit differentiation in combination with linearized lifting-surface theory to evaluate the sensitivity coefficients. This can be used as a benchmark criteria for assessing the accuracy of approximate methods. A semi-analytical technique, using linear unsteady aerodynamics, has been applied to an isolated wing-section and rotating propfan blades by Murthy and Kaza [4]. Some aeroelastic analysis for a transport wing has been investigated by Grossman et al. [5], where a coupled aerodynamic and structure model influences the design. Livne et al. [6] and a few other researchers focus on more complex interactions such as inclusion of active controls on the overall optimization process. Elbanna and Carlson [7] developed a quasi-analytical technique for evaluating wing-section aerodynamic sensitivity coefficients in transonic and supersonic flight regimes. Later, they extended the technique to 3D full potential equations using the symbolic manipulator MACSYMA to obtain the sensitivity coefficients. The procedure was applied to a ONERA M6 wing planform with NACA 1406 wing-sections [8]. For non-linear aerodynamics, most of the efforts are concentrated on involvement of CFD for both flow and sensitivity analyses. Baysal and Eleshaky [9,10] presented an aerodynamic design strategy using direct differentiation of Euler equations. The procedure was applied to design a scramjet-afterbody configuration

[1]Numbers in brackets indicate references

for an optimized axial thrust. This scheme was later extended to include domain decomposition capabilities in order to reduce the computational costs associated with complex configurations [11].

Taylor et al. [12] conducted a feasibility study of sensitivity analysis involving Euler equations. The method was successfully applied to two test problems, including a subsonic nozzle and a supersonic inlet. The sensitivity derivatives are obtained by direct differentiation of governing equations with respect to geometric design parameters. The authors later expanded the formulation to include thin-layer Navier-Stokese equations and a optimizer. Aerodynamic sensitivity derivatives were obtained for an internal flow through a double-throat nozzle and an external flow over a NACA four-digit wing-section [13]. Both geometries were optimized with new design having a significantly improved performance. The flow and flow sensitivity analysis module (ANSERS), developed by these authors, have been implemented in this study. Burgreen et al. [14] improved the efficiency of an aerodynamic shape optimization on two fronts. The first improvement involves replacing a previously grid point-based approach for surface parameterization with a Bezier-Bernstein polynomial parameterization. The second improvement includes the use of Newton's method instead of familiar and expensive Alternating Direction Implicit (ADI) technique to calculate the flow solutions. Other notable schemes include variable- complexity design strategies, developed by Hutchison et al. [15,16], to combine conceptional and preliminary-design approaches. The strategy has been used to optimize the HSCT wing configuration. Verhoff et al. [17,18] developed a method for optimal aerodynamic design of wing-sections using analytically computed aerodynamic sensitivities. The scheme also utilizes Chebyshev polynomials together with parametric stretching functions to define camber and thickness distribution of wing-section. Due to analytical parameterization of surface, the package produces an efficient optimal results.

1.3 Objectives of Present Study

After reviewing relevant literature, it is apparent that one aspect of aerodynamic sensitivity analysis, namely grid sensitivity, has not been investigated extensively. The grid sensitivity algorithms in most of these studies are based on structural design models. Such models, although sufficient for preliminary or conceptional design, are not acceptable for detailed design analysis. Careless grid sensitivity evaluations, would introduce gradient errors within the sensitivity module, therefore, infecting the overall optimization process [19]. Development of an efficient and reliable grid sensitivity module with special emphasis on aerodynamic applications appears essential.

Unlike aerodynamic considerations, the grid sensitivity analysis has been used on structural design models for a number of years. In this context, grid sensitivity can be thought as perturbation of structural loads, such as displacement or natural frequency, with respect to finite element grid point locations [20]. Two basic approaches have been cited for grid sensitivity derivatives. The first approach, known as implicit differentiation, is based on implicit differentiation of discretized finite element system. The other, which is based on the variation of continuum equations, is known as variational or material derivative approach. The main objective here is to develop a fast and inexpensive method for grid sensitivity to be used on an automated aerodynamic optimization cycle.

Among two major classes of grid generation systems (Algebraic, Differential), algebraic grid generation systems are ideally suited for achieving this objective. The explicit formulation, resulting in a fast and suitable grid, enables direct differentiation of grid coordinates with respect to design parameters [21,22]. The underlying effort here is to avoid the time consuming and costly numerical differentiation. In

addition, the analytical derivatives are exact, a desirable feature for sensitivity analysis. An important ingredient of grid sensitivity is the surface parameterization. The most general parameterization would be to specify every grid point on the surface as a design parameter. This, although convenient, is unacceptable due to high computational cost. It is essential to keep the number of parameters as low as possible to avoid a surge on computational expenses. An analytical parameterization, may alleviate that problem but it suffers from lack of generality. A compromise would be using spline functions such as a Bezier or Non-Uniform Rational B-Spline (NURBS) function to represent the surface [23,24]. In this manner, most aerodynamically inclined surfaces can be represented with few control (design) parameters.

Another important aspect of grid sensitivity, grid sensitivity with respect to grid parameters, also deserves more attention. This concept, leading to grid optimization, can be used to enhance the quality of grid in optimization cycle, resulting in better flow analysis and faster convergence rates. The accuracy, stability, and general reliability of most flow solvers for any problem may be strongly influenced by the choice and quality of grid. This implies that the problem of generating a suitable grid is no longer only restricted to generating a valid grid, but also the related issue of manipulating that grid to achieve certain objectives. Among those objectives, grid smoothness, orthogonality, clustering, and far-field boundary location are considered most significant. For example, grid smoothness is an important property since an abrupt change in grid size may prompt inaccuracy, ill-conditioning, and instability in the flow solution. The orthogonality factor can play an essential role in finite-difference computations where near orthogonality of grid lines are desirable. Also, the accuracy and efficiency of most computational schemes are enhanced by grid clustering in regions of high gradients (e.g., boundary layer, shocks, etc.). The far-field boundary location has been identified as a dominant factor in influencing the solution for a fixed initial conditions. For example, previous investigations indicate

that for a symmetrical wing-section, the error in lift coefficient has an inverse radial dependency on the boundary extent [33]. As required by most optimization techniques, the sensitivity of the grid with respect to those parameters influencing these objectives is required.

The organization of this study is as follows. The physical and geometric representations of a typical model are derived in Chap. 2. The grid generation algorithm and boundary grid distribution are developed in Chap. 3. Chapter 4 discusses the theoretical formulation and aerodynamic sensitivity equation. The method of solution is provided in Chap. 5. The results are presented and discussed in Chap. 6. Finally, some concluding remarks are provided in Chap. 7.

Chapter 2

PHYSICAL MODEL

2.1 Wing-Section Example

The physical model considered for this study is an isolated wing-section since much research has been devoted to its development and representation. This design is essential for the performance of an advanced aircraft for both subsonic and supersonic speeds. Other applications could be helicopter rotor blades, and high performance fans. Two approaches have been chosen to generate the desired wing-sections. The first approach is a physical (i.e., analytical) representation resulting in classical NACA four-digit wing-sections. The second approach is a geometric (i.e., approximative) representation of the wing-sections using NURBS.

2.1.1 Physical Representation

The NACA four-digit wing sections are examined for grid-generation parameterization. Families of wing sections are described by combining a mean line and a thickness distribution. The resultant expressions possess the necessary features that suit the problem, mainly the concise description of a wing section in terms of several design parameters. Reference 25 provides the general equations which define a mean line and a thickness distribution about the mean line. The design parameters are: $T \equiv$ the maximum thickness, $M \equiv$ the maximum ordinate of the mean line or camber, and $C \equiv$ chordwise position of maximum ordinate. The numbering system for NACA four-digit wing-section is based on the geometry of the section. The first and

second integers represent M and C respectively, while the third and fourth integers represent T. Symmetrical sections are designated by zeros for the first two integers, as in the case of NACA 0012 wing-section. Figure 2.1 provides a schematic of the section definition. The ξ-coordinate is mapped into the chord line $x = x(r) = x(f_1(\xi))$ covering both the top and bottom of the section. Details of mapping will be discussed in the next chapter. The mean line equation is

$$y_c(x) = \frac{M}{C^2}(2Cx - x^2), \quad x \leq C \tag{2.1}$$

$$y_c(x) = M\frac{(1 - 2C + 2Cx - x^2)}{(1 - C)^2}, \quad x \geq C. \tag{2.2}$$

The section thickness is given by

$$y_T(x) = \frac{T}{0.2}(0.2969x^{\frac{1}{2}} - 0.126x - 0.3516x^2 + 0.2843x^3 - 0.1015x^4). \tag{2.3}$$

The section coordinates are

$$x_1(r, \mathbf{P}_1^{\xi}) = x \qquad y_1(r, \mathbf{P}_1^{\xi}) = y_c(x) \pm y_T(x) \tag{2.4}$$

where $\mathbf{P}_1^{\xi}$ represents the vector of independent parameters to be defined later.

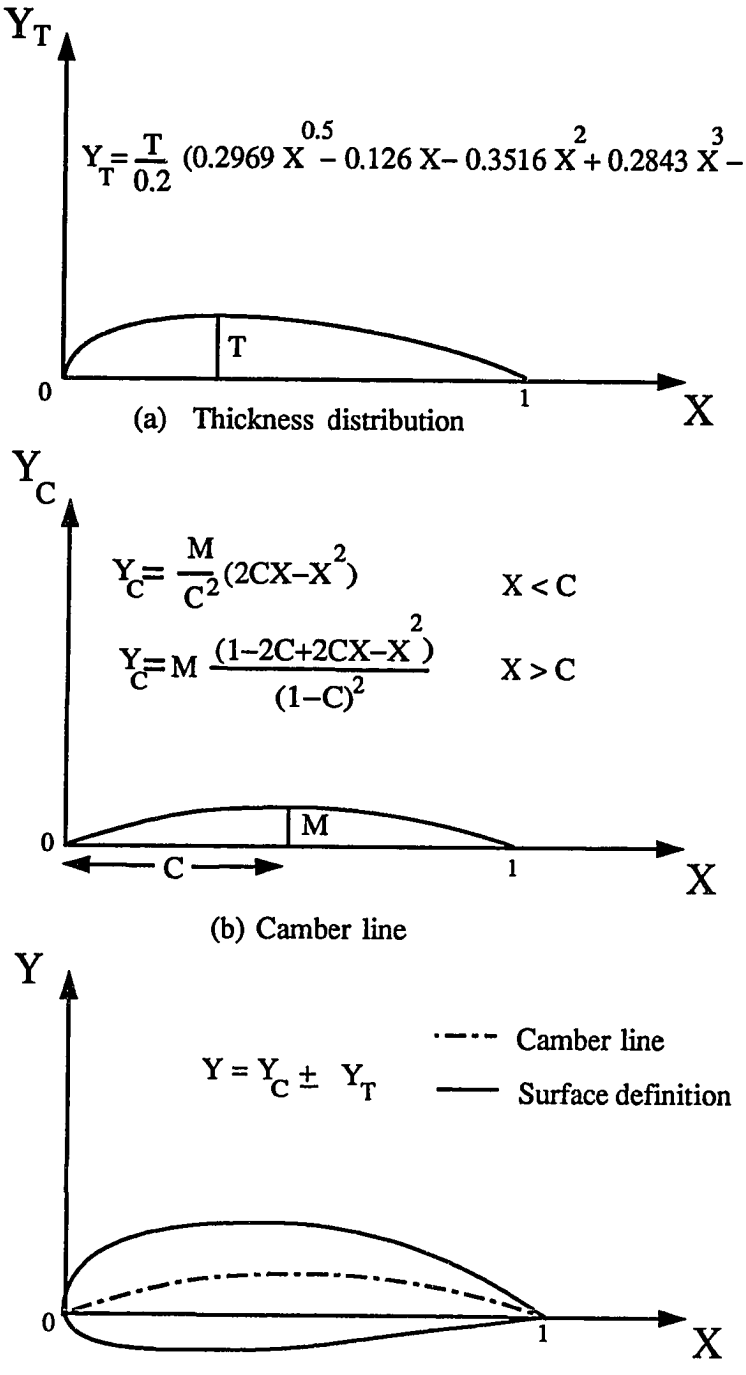

Fig. 2.1 Wing–section specification for NACA four–digit series.

2.1.2 Geometric Representation

Another approach for representing a wing-section model is using a spline function to approximate the surface. The most commonly used approximative representation is the *Non-Uniform Rational B-Spline* (NURBS) function. The NURBS provide a powerful geometric tool for representing both analytic shapes (conics, quadrics, surfaces of revolution, etc.) and free-form surfaces [26-28]. The relation for a NURBS curve is

$$\mathbf{X}(r) = \frac{\sum_{i=0}^{n} N_{i,p}(r)\omega_i \mathbf{D}_i}{\sum_{i=0}^{n} N_{i,p}(r)\omega_i} \qquad \mathbf{X}(r) = \begin{Bmatrix} x(r) \\ y(r) \end{Bmatrix} \qquad \mathbf{D}_i = \begin{Bmatrix} X_i \\ Y_i \end{Bmatrix} \tag{2.5}$$

$$i = 0, ..., n$$

where $\mathbf{X}(r)$ is the vector valued surface coordinate in the r-direction, $\mathbf{D}_i$ are the control points (forming a control polygon), ω_i are weights, and $N_{i,p}(r)$ are the p-th degree B-Spline basis function defined recursively as

$$N_{i,0}(r) = \begin{cases} 1 & r_i \leq r \leq r_{i+1} \\ 0 & otherwise \end{cases}$$

$$N_{i,p}(r) = \frac{r - r_i}{r_{i+p} - r_i} N_{i,p-1}(r) + \frac{r_{i+p+1} - r}{r_{i+p+1} - r_{i+1}} N_{i+1,p-1}(r). \tag{2.6}$$

The r_i are the so-called knots forming a uniform knot vector

$$\mathbf{r} = \left\{ \underbrace{a \cdots a}_{p+1}, r_{p+1}, ..., r_{m-p-1}, \underbrace{b \cdots b}_{p+1} \right\} \tag{2.7}$$

where the end knots a and b are repeated with multiplicity $p + 1$. The degree, p, number of knots, $m + 1$, and number of control points, $n + 1$, are related by

$$m = n + p + 1. \tag{2.8}$$

For most practical applications the knot vector is normalized and the basis function is defined on the interval $(a = 0, b = 1)$. Equation (2.5) can be rewritten as

$$\mathbf{X}(r) = \sum_{i=0}^{n} R_{i,p}(r)\mathbf{D}_i \qquad R_{i,p}(r) = \frac{N_{i,p}(r)\omega_i}{\sum_{i=0}^{n} N_{i,p}(r)\omega_i} \qquad i = 0, ..., n \tag{2.9}$$

where $R_{i,p}(r)$ are the *Rational Basis Functions*, satisfying the the following properties among many others found in [22]

$$\sum_{i=0}^{n} R_{i,p}(r) = 1 \qquad R_{i,p}(r) \geq 0. \tag{2.10}$$

Three options are available to define a wing-section using the NURBS algorithm. In the first option, the camber line is defined by a NURBS curve using three control points. The thickness distribution, Eq.(2.3), is then added and subtracted to the camber. The first and last control points are fixed for the section chord. The design parameters using this option are the location of the middle control point, its weight, and the maximum thickness T as shown in Fig. 2.2. Figure 2.3 shows the corresponding quadratic basis function (p=2,n=2) with weights set to 1 (i.e., $\omega_i = 1, i = 0, 2$). The choice of number of control points is a trade-off between complexity and functionality [4]. Figures 2.4 and 2.5 illustrate the effect of increasing the number of control points on camber, wing-section, and the basis function.

The second option is to define both camber and thickness distribution curves using NURBS representation. The new wing-section can be obtained using Eq. (2.4). Both camber and thickness distribution curves are defined using three control points. This approach, although promises more design control, it also increases the number of design parameters as shown in Fig. 2.6.

The third option is to bypass the camber and thickness distributions completely and control the wing-section directly with NURBS control points and weights. Figure 2.7 illustrates a seven control point representation of a wing-section. The points at the leading and trailing edges are fixed. Two control points at the 0% chord

are used to affect the bluntness of the section. The movement of control points as shown in Fig 2.8 creates the effect of camber in the wing-section. The cubic basis function (p=3) using this approach is shown in Fig. 2.9 with weights set to 1.

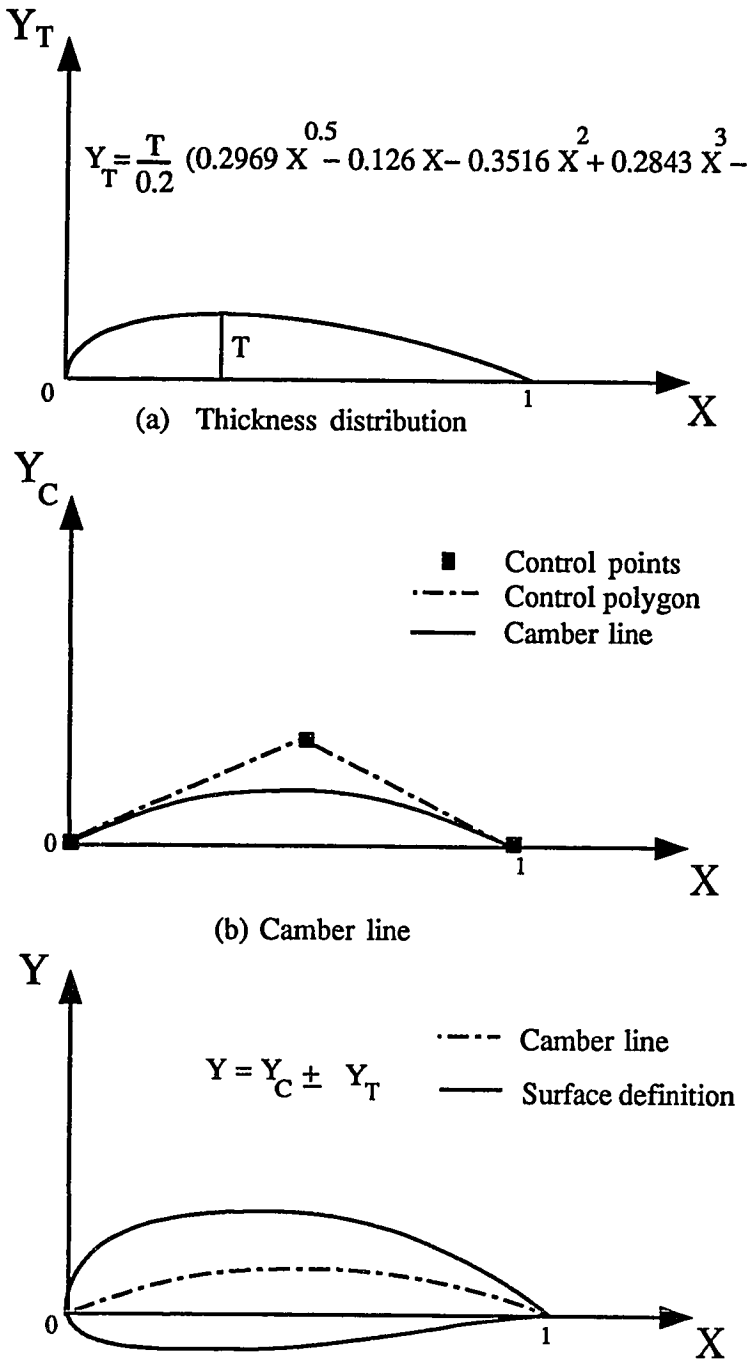

Fig. 2.2 Wing-section specification using NURBS (option 1).

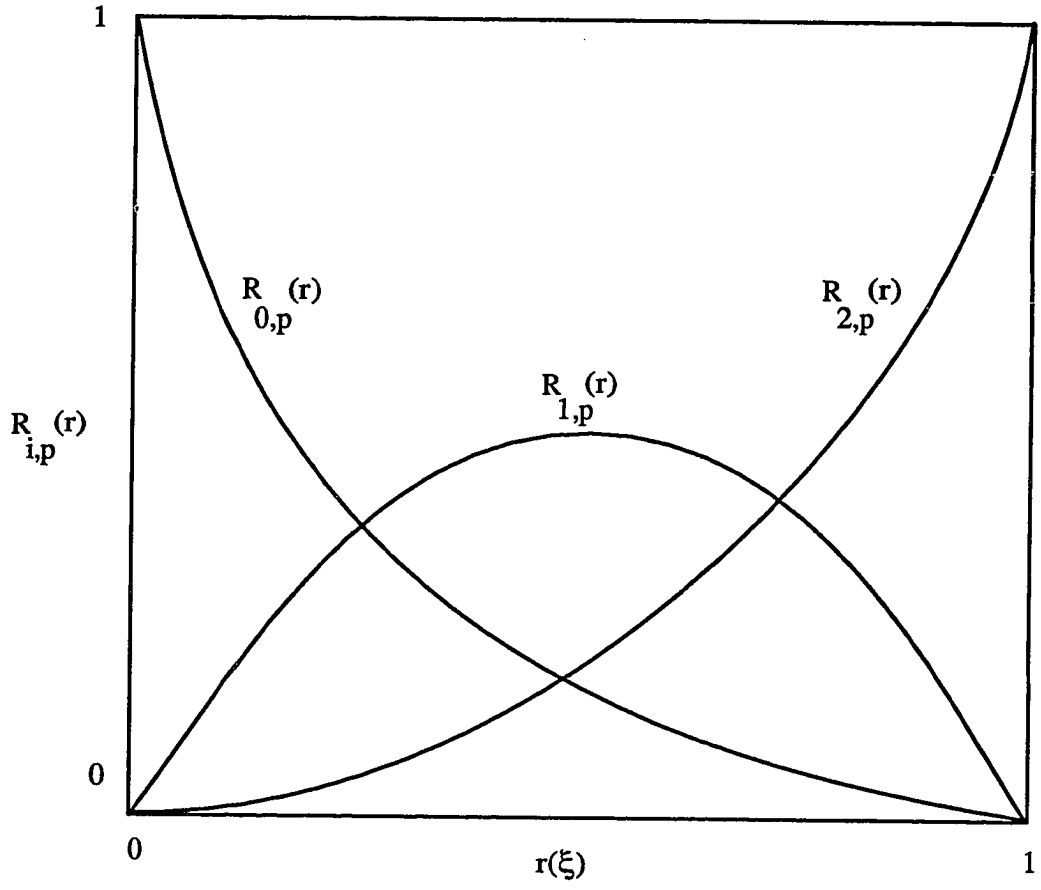

Fig. 2.3 Quadratic basis function (p=2) for camber line (option 1).

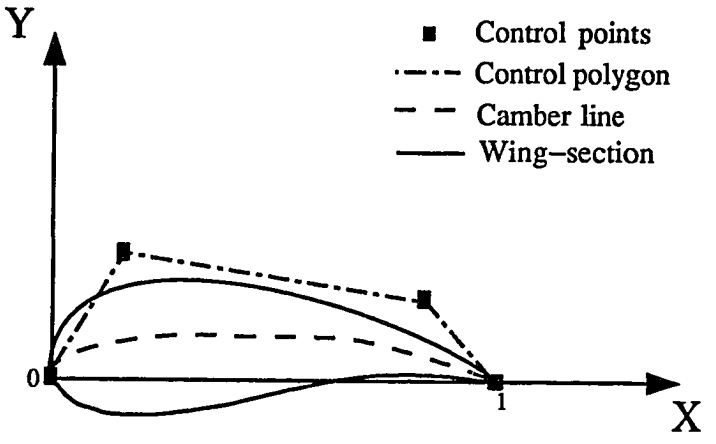

Fig. 2.4 Effects of increasing the number of control points on camber and wing–section.

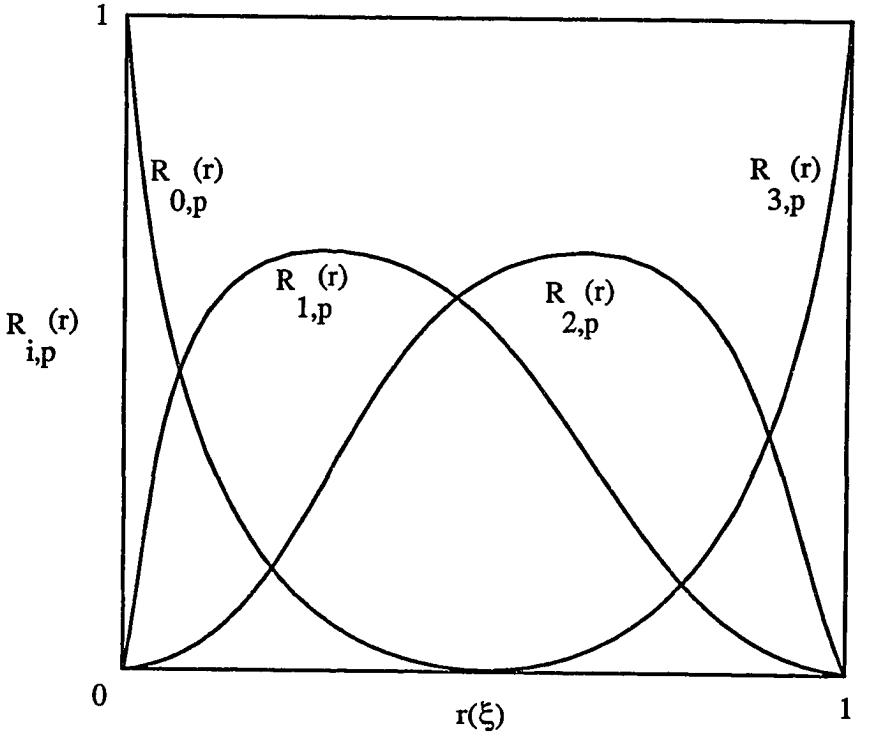

Fig. 2.5 Effects of increasing the number of control points on a quadratic basis function.

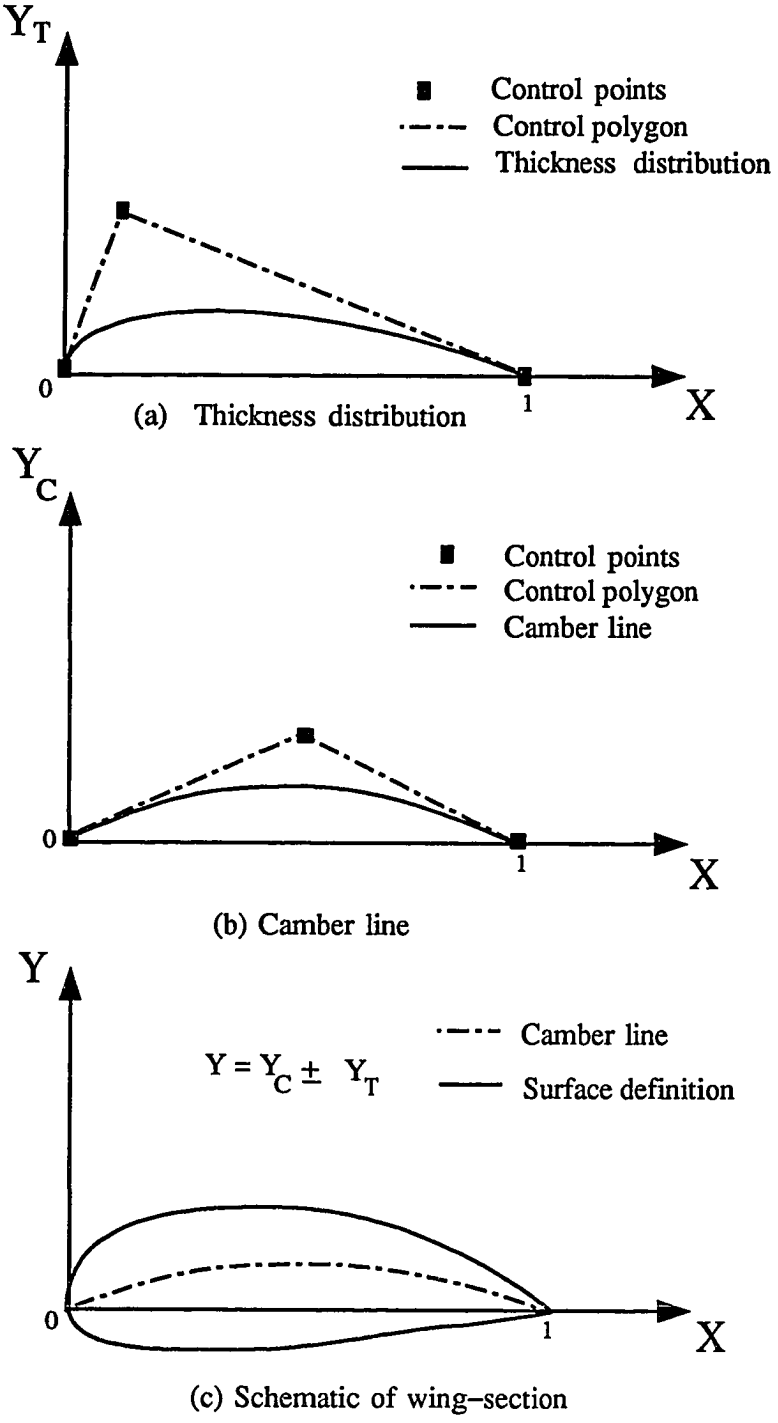

Fig. 2.6 Wing–section specification using NURBS (option 2).

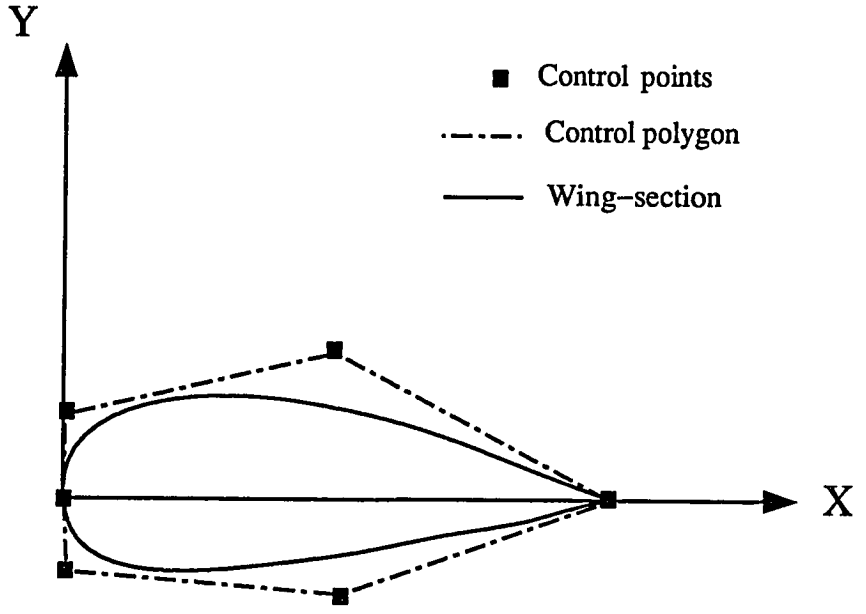

Fig. 2.7 Seven control points wing–section specification using NURBS (option 3).

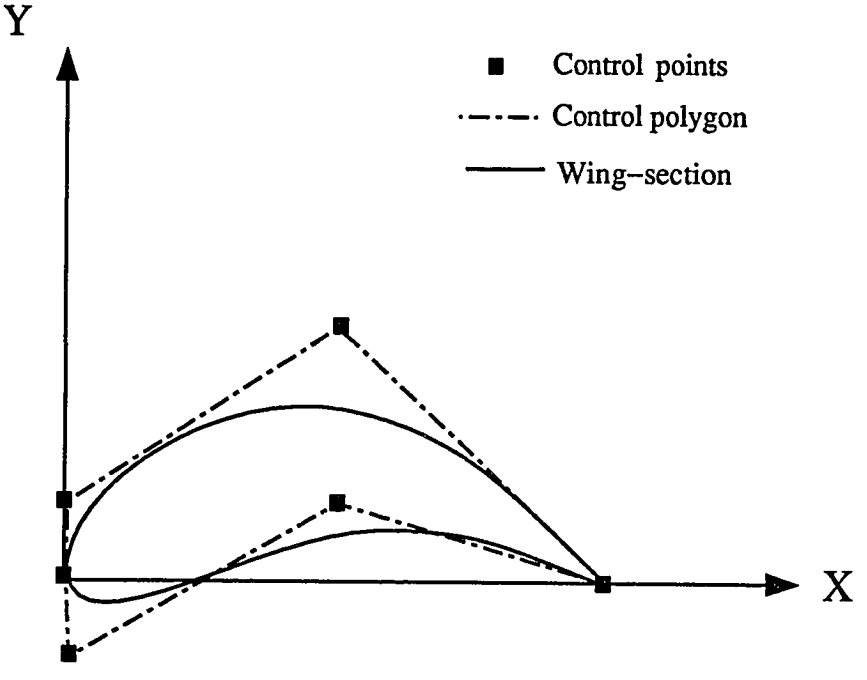

Fig. 2.8 Effect of control point movement.

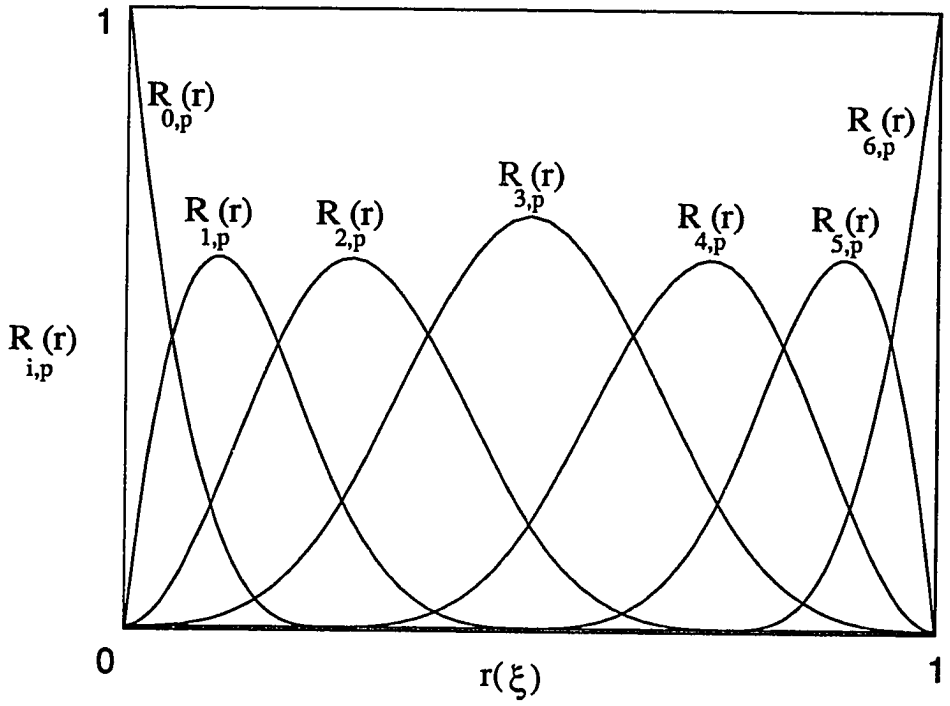

Fig. 2.9 Cubic basis function(p=3).

Chapter 3

GRID GENERATION

3.1 Introduction

In order to study the flow-field around any aerodynamic configuration, a system of nonlinear partial differential equations must be solved over a highly complex geometry [29]. The domain of interest should be descretized into a set of points where an implied rule specifies the connectivity of the points. This discretization, known as *grid generation*, is constrained by underlying physics, surface geometry, and the topology of the region where the solution is desired [30-32]. A poorly constructed grid with respect to any of the above constraints, may fail to reveal critical aspects of the true solution.

The discretization of the field requires some organization in order for the solution to be efficient. The logistic structure of the data such as grid spacing, the location of outer boundaries, and the orthogonality can influence the nature of the solution [33,34]. Furthermore, the discretization must conform to the boundaries of the region in such a way that boundary condition can be accurately represented [35]. This organization can be provided by a curvilinear coordinate system where the need for alignment with the boundary is reflected in routine choice of cartesian coordinate system for rectangular region, cylindrical coordinate for circular region, etc. This curvilinear coordinate system covers the field and has coordinate lines coincident with all boundaries. To minimize the number of grid points required for a desired accuracy, the grid spacing should be smooth, with concentration in regions of high

solution gradients. These regions may be the result of geometry (large surface slopes or corners), compressibility (entropy and shock layers), and viscosity (boundary and shear layers). A complex flow may contain a variety of such regions of various length scales, and often of unknown location.

Two primary categories for arbitrary coordinate generation have been identified. There are algebraic systems and partial differential systems. The algebraic systems are mainly composed of interpolative schemes such as *Transfinite Interpolation* [36], *Multi-Surface Interpolation* [37], and *Two-Boundary Interpolation* techniques [38]. The basic mathematical structure of these methods are based on interpolation of the field values from the boundary. For partial differential equation systems, a set of partial differential equations must be solved to obtain the field values. The differential methods may be *elliptic*, *parabolic*, or *hyperbolic*, depending on the boundary specification of the problem. Each of these grid generation systems has its own advantages and drawbacks depending on geometry and application of the problem. Algebraic generating systems offer speed and simplicity while providing an explicit control of the physical grid shape and grid spacing. However, they might produce skewed grids for boundaries with strong curvature or slope discontinuity. Partial differential systems, although offer relatively smooth grids for most applications, are computer intensive, specially for three-dimensional cases. An alternative, a common practice in recent years, has been to originate the grid using an algebraic system and then smooth the field using a differential system. Such hybrid approach proven to be successful and cost effective for most applications.

An array of general purpose grid generation softwares have been emerged over past few years. Among many others, the GRAPE2D of Sorenson [39], the EAGLE of Thompson [40], and GRIDGEN by Steinbrenner et al. [41], are the most widely used. The GRAPE2D solves Poisson's equation in two-dimension and utilizes a novel approach for determination of the boundary control functions. The

EAGLE code combines techniques in surface grid generation as well as two or three-dimensional field grid generation. The GRIDGEN series is a more recent appearance with both algebraic and differential generation capabilities on an interactive environment. Another new arrival, called ICEM/CFD, has the capability of combining a full Computer Aided Design system (CAD), with grid generation module [42]. This, provides an efficient and also quick procedure to reflect the CAD model changes on grids. Most of these packages furnish a host of options with a high degree of flexibility. However, intelligent use of the majority of these options requires the user to be well versed in current grid generation techniques.

Due to directness and relative simplicity of algebraic systems, the remainder of this chapter would be devoted to their development. The relevant aspects of algebraic generation system such as boundary coordinate transformation, mapping, boundary discretization, and surface grid generation are discussed in the following sections.

3.2 Boundary-Fitted Coordinate Transformation

Structured algebraic grid generation techniques can be thought of as transformation from a rectangular computational domain to an arbitrarily -shaped physical domain as shown in Fig. 3.1 [43]. The transformation is governed by vector of control parameters, $\mathbf{P}$, and can be expressed as

$$\mathbf{X}(\xi,\eta,\zeta,\mathbf{P}) = \begin{Bmatrix} x(\xi,\eta,\zeta,\mathbf{P}) \\ y(\xi,\eta,\zeta,\mathbf{P}) \\ z(\xi,\eta,\zeta,\mathbf{P}) \end{Bmatrix} \tag{3.1}$$

where

$$0 \leq \xi \leq 1, \;\; 0 \leq \eta \leq 1, \;\; \textit{and} \;\; 0 \leq \zeta \leq 1.$$

The control parameter $\mathbf{P}$, is composed of parameters which control the primary shape of the boundary (design parameters), and parameters which control the grid

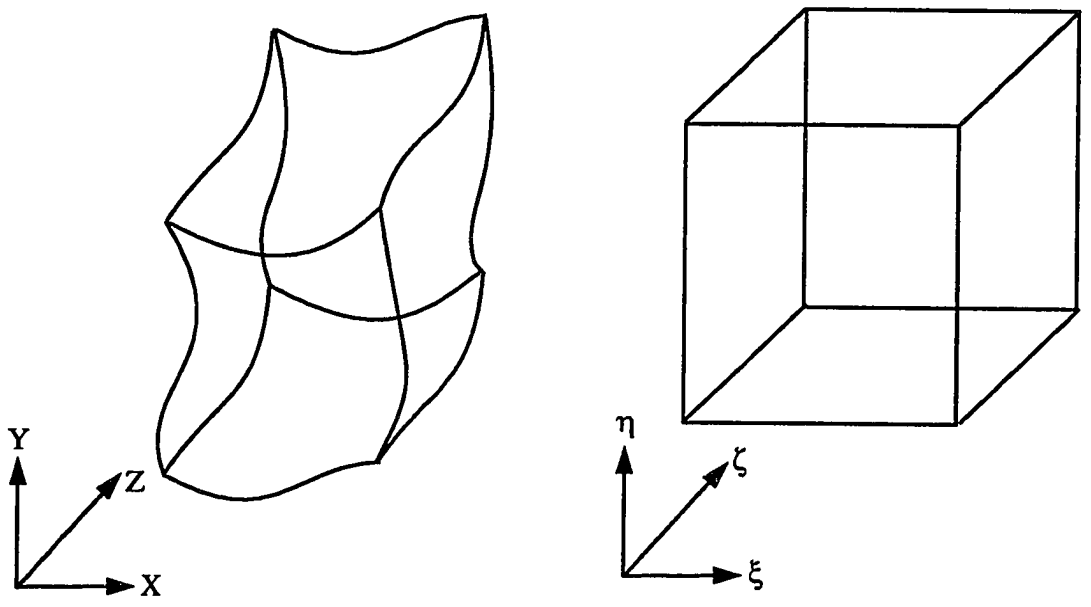

(a) Physical domain (b) Computational domain

Fig. 3.1 Physical and computational coordinates.

(grid parameters). A discrete subset of the vector-valued function $\mathbf{X}(\xi_i, \eta_j, \zeta_k, \mathbf{P}) \equiv \mathbf{X}\{\, x\ y\ z\,\}^T_{i,j,k} \equiv \mathbf{X}^*$ is a structured grid for $\xi_i = \frac{i-1}{L-1}, \eta_j = \frac{j-1}{M-1}, \zeta_k = \frac{k-1}{N-1}$, where $i = 1, 2, 3 \cdots, L,\ \ j = 1, 2, 3, \cdots, M$ and $k = 1, 2, 3, \cdots, N$.

The orientation of the computational coordinates relative to physical coordinate, known as *grid topology*, is an important aspect of the transformation procedure. In order to establish a grid topology for any geometry, it is essential to examine each component separately [44,45]. For any given geometry, there are several possible topologies with different characteristics in terms of efficiency, coordinate cuts, singularities, etc. For example a typical wing-section geometry, may have at least three types of different topologies (e.g., C-, O-, or H-types) as illustrated in Fig. 3.2. The C- and O-type topologies usually produce the most efficient grid. For present study a C-type topology has been chosen and the mapping is shown in Fig. 3.2(a). This topology produces no singularity and it is relatively simple to implement. For wing-sections with sharp noses, a H-type topology would be more appropriate. For more complex geometries, selection of different computational coordinate systems for different regions of physical domain might be required. In this case, physical domain is mapped into several computational sub-domains, where each sub-domain is refered as a *block*. Therefore, it is possible to have a boundary-fitted coordinate system for a highly complex configurations. For example, a typical airplane geometry has two main components: the fuselage and the wing. A fuselage has a circular like cross-section which suggests a natural O-type (cylindrical coordinate) grids. This topology produces a nearly orthogonal grid with one line polar singularity at the nose. For the streamwise direction, it is feasible to have either a C-type or a H-type grid depending on the slope of the nose. For a fuselage with small nose slope, a H-type grid in the streamwise direction would be more appropriate. A wing has its own natural coordinates which are usually not compatible with the fuselage's coordinate system. It is possible to generate a H-, O-, or a C-type grids in the streamwise direction, and a C-

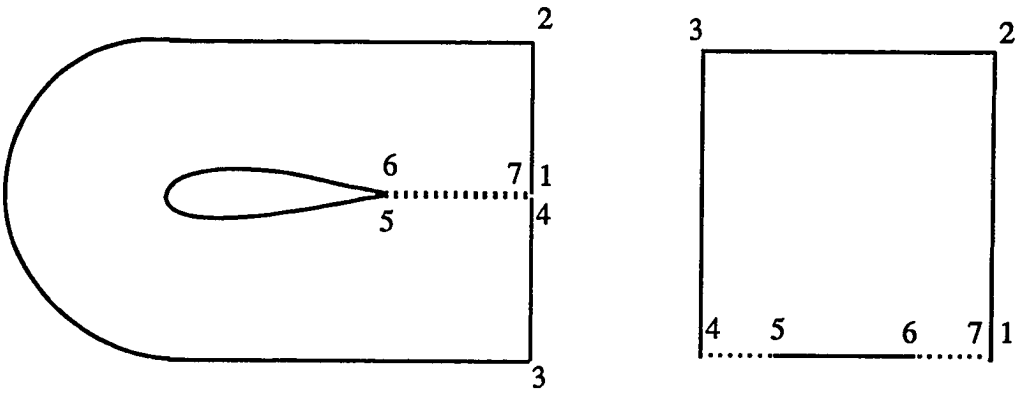

(a) C–type mapping

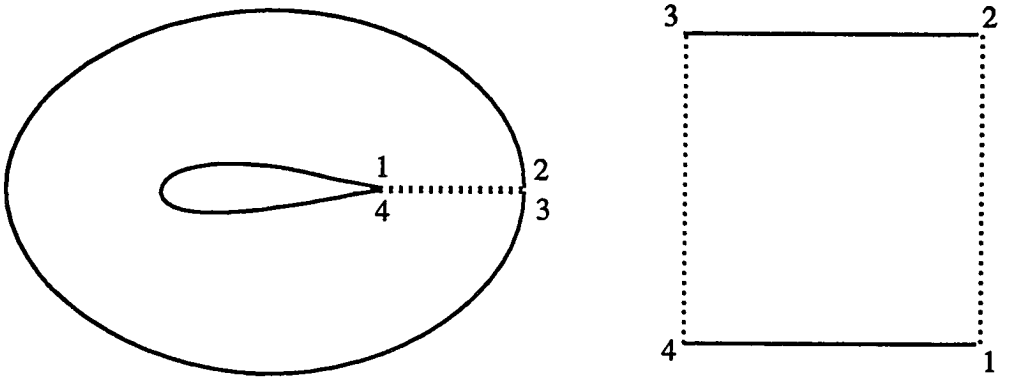

(b) O–type mapping

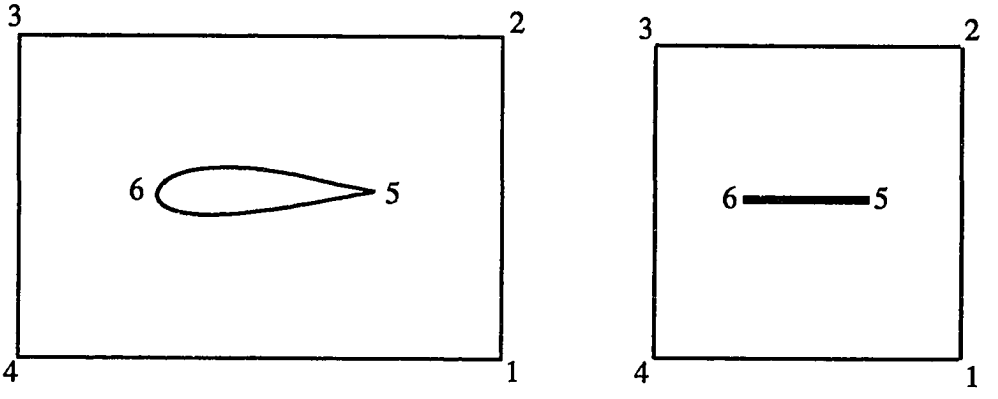

(c) H–type mapping

Fig. 3.2 Different mapping types of a wing–section.

or a H-type in crosswise direction. To maintain a minimum of C^0 continuity at the interfaces, it is essential to select a compatible topology for the wing and fuselage. For most cases it is conceivable to generate a single block grid about these components, but this grid tends to be skewed for any practical purposes. A dual-block grid possesses much less skewness than a single-block grid. It consists of two large blocks, one covering the top portion of the physical domain, and the other covering the bottom portion of the physical domain. The dual-block topology is a direct consequence of using a H-type grid for the wing of zero wing-tip area. Figure 3.3 illustrates the mapping of a generic airplane geometry using a dual-block topology. A C-O type grid have been chosen for a fuselage while the wing, horizontal, and vertical tails mapped to a H-H type grids.

Once the grid topology has been selected, then the grid on the boundary can be generated. The boundary discretization techniques will be discussed in following section.

3.3 Boundary Discretization

Before generating the interior grid, the grid-point distribution along the boundary edges should be computed. A discrete uniform distribution of the computational coordinate can be mapped into an arbitrary distribution of the physical coordinate, using a specified control function. The essence of mapping is that the abscissa corresponds to the percentage of grid points and the ordinate corresponds to a particular control function which, in turn, relates to the geometric definition of the physical domain. The control functions must be monotonic in parametric space, and can be computed by an analytical function or by a numerical approximation. Analytical functions are generally limited to simple boundary curves. However, a complex boundary can be decomposed to several sections, and analytical functions

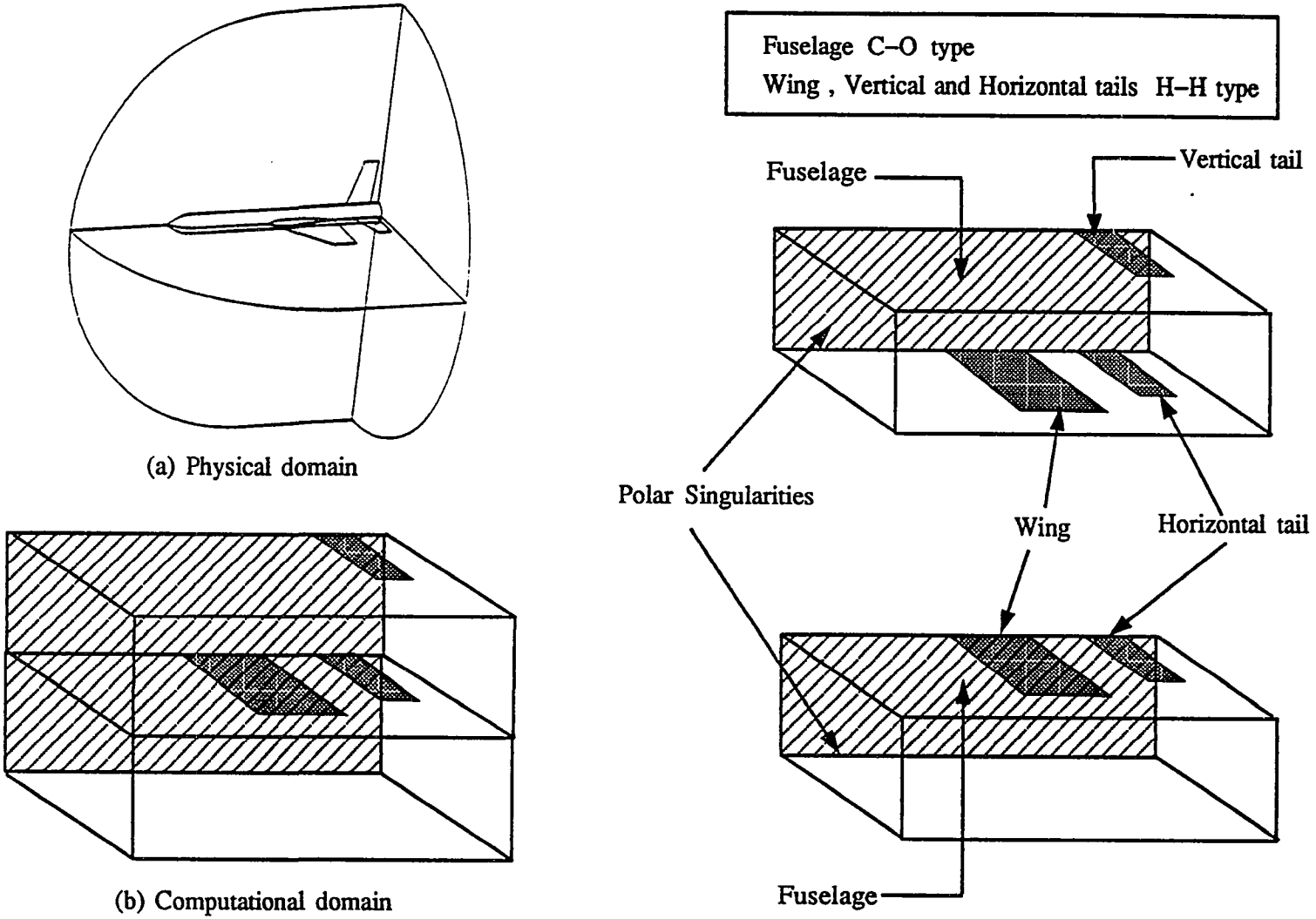

(a) Physical domain

(b) Computational domain

Fig. 3.3 Dual–block grid topology for a generic airplane configuration

can be used for each section [46]. The advantage of analytical functions are their simplicity and the guaranteed monotonicity. Exponentials are the most widely used analytical functions and can be expressed as

$$r(\xi) = Y_{i-1} + [Y_i - Y_{i-1}] \frac{e^{B_{i-1}(\frac{\xi - X_{i-1}}{X_i - X_{i-1}})} - 1}{e^{B_{i-1}} - 1} \quad for \quad X_{i-1} \leq \xi \leq X_i \tag{3.2}$$

where

$$0 \leq X_i, Y_i \leq 1 \quad , \quad 0 \leq \xi, r(\xi) \leq 1 \quad and \quad i = 2, ..., m.$$

The integer m represents number of control points with coordinates $\{X_i, Y_i\}$. The quantity B_{i-1}, called the stretching parameter, is responsible for grid density. Specifying B_1, values of $B_{i \geq 2}$ are obtained by matching the slopes at control points. This, guaranteeing a smooth grid transition between each region, can be accomplished using Newton's iterative scheme which is quadratically convergent.

The exponential function, while reasonable, is not the best choice when the variation in grid spacing is large [35,47]. The truncation error associated with the metric coefficients is proportional to the rate of change of grid spacing. A large variation in grid spacing, such as the one resulting from exponential function, would increase the the truncation error, hence, attributing to the solution inaccuracies [35]. A suggested alternative to exponential function has been the usage of hyperbolic sine function given as

$$r(\xi) = Y_{i-1} + [Y_i - Y_{i-1}] \frac{sinh[B_{i-1}(\frac{\xi - X_{i-1}}{X_i - X_{i-1}})]}{sinh(B_{i-1})} \quad for \quad X_{i-1} \leq \xi \leq X_i \tag{3.3}$$

where

$$0 \leq X_i, Y_i \leq 1 \quad , \quad 0 \leq \xi, r(\xi) \leq 1 \quad and \quad i = 2, ..., m.$$

The hyperbolic sine function gives a more uniform distribution in the immediate vicinity of the boundary, resulting in less truncation error. This criteria makes the hyperbolic sine function an excellent candidate for boundary layer type flows. A more appropriate function for flows with both viscous and non-viscous effect would be the

usage of a hyperbolic tangent function such as

$$r(\xi) = Y_{i-1} + [Y_i - Y_{i-1}] \left\{ 1 + \frac{tanh[\frac{B_{i-1}}{2}(\frac{\xi - X_{i-1}}{X_i - X_{i-1}} - 1)]}{tanh(\frac{B_{i-1}}{2})} \right\} \quad for \quad X_{i-1} \leq \xi \leq X_i \tag{3.4}$$

where

$$0 \leq X_i, Y_i \leq 1 \quad , \quad 0 \leq \xi, r(\xi) \leq 1 \quad and \quad i = 2, ..., m.$$

The hyperbolic tangent gives more uniform distribution on the inside as well as on the outside of the boundary layer to capture the non-viscous effects of the solution. Such overall improvement, makes the hyperbolic tangent a prime candidate for grid point distribution in viscous flow analysis. Figure 3.4 illustrates these distribution functions and the corresponding grids on a unit square.

Similarly, a numerical approximation can be used to compute the grid-point distribution on a boundary curve. This approach is widely used for complex configurations and care must be taken to insure monotonicity of the distribution. For example, the natural cubic spline is C^2 continuous and offers great flexibility in grid spacing control. However, some oscillations can be inadvertently introduced into the control function. The problem can be avoided by using a smoothing cubic spline technique and specifying the amount of smoothing as well as control points [46]. Another choice would be the usage of a lower order polynomial such as Monotonic Rational Quadratic Spline (MRQS) which is always monotonic and smooth [29]. Other advantage of MRQS over cubic spline is that it is an explicit scheme and does not require any matrix inversion.

3.4 Transfinite Interpolation

The dominant algebraic approach for grid generation is the *Transfinite Interpolation* scheme. The general methodology was first described by Gordon [36] , and

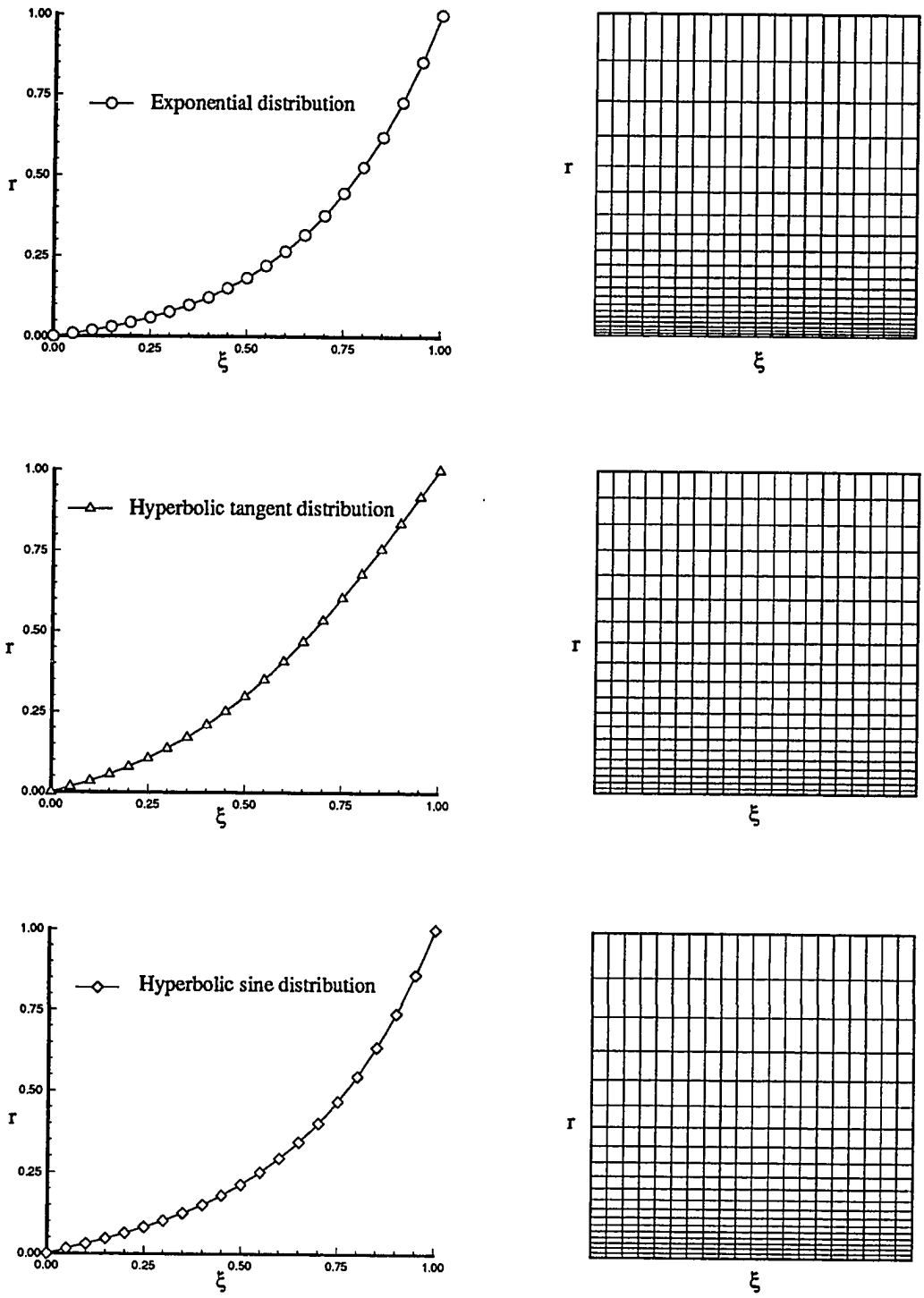

Fig. 3.4 Grid resulting from typical distribution functions.

there have been numerous variations applied to particular problems. The methodology can be presented as recursive formulas composed of univariate interpolations [45] or as the Boolean sum of univariate interpolations [43]. Here, we follow the Boolean sum representation; but, for brevity, we restrict the process to two dimensions and omit some of the details that can be found in [43]. Also, to be consistent with the example considered below, the parameterization is restricted to functions and first derivatives at the boundaries ($\xi = 0, 1$) and ($\eta = 0, 1$) and control in the interpolation functions. The transformation is

$$\mathbf{X}(\xi, \eta, \mathbf{P}) = \mathbf{U} \oplus \mathbf{V} = \mathbf{U} + \mathbf{V} - \mathbf{UV} \tag{3.5}$$

where

$$\mathbf{U} = \sum_{I=1}^{2} \sum_{n=0}^{1} \alpha_I^n(\xi, \mathbf{P}_0^\xi) \frac{\partial^n \mathbf{X}(\xi_I, \eta, \mathbf{P}_I^\eta)}{\partial \xi^n} \tag{3.6}$$

and

$$\mathbf{V} = \sum_{J=1}^{2} \sum_{m=0}^{1} \beta_J^m(\eta, \mathbf{P}_0^\eta) \frac{\partial^m \mathbf{X}(\xi, \eta_J, \mathbf{P}_J^\xi)}{\partial \eta^m}. \tag{3.7}$$

The term $\mathbf{UV}$ is the tenser product of the two univariate interpolations and can be expressed as

$$\mathbf{UV} = \sum_{I=1}^{2} \sum_{J=1}^{2} \sum_{n=0}^{1} \sum_{m=0}^{1} \alpha_I^n(\xi, \mathbf{P}_0^\xi) \beta_J^m(\eta, \mathbf{P}_0^\eta) \frac{\partial^{nm} \mathbf{X}(\xi_I, \eta_J, \mathbf{P}_I^\eta, \mathbf{P}_J^\xi)}{\partial \xi^n \partial \eta^m}. \tag{3.8}$$

The boundary curves and their derivatives ($\frac{\partial^n \mathbf{X}(\xi_I, \eta, \mathbf{P}_I^\eta)}{\partial \eta^n}$ and $\frac{\partial^m \mathbf{X}(\xi, \eta_J, \mathbf{P}_J^\xi)}{\partial \eta^m} I, J = 1, 2\ m$, $n = 0, 1$) are blended into the interior of the physical domain by the interpolation functions $\alpha_I(\xi, \mathbf{P}_0^\xi)$ and $\beta_J(\eta, \mathbf{P}_0^\eta)$. The boundary grid, the derivatives at the boundary grid and the spacing between points are governed by the parameters $\left\{\mathbf{P}_J^\xi\ \mathbf{P}_I^\eta\right\}^T$. The interpolation functions are controlled with the parameters $\left\{\mathbf{P}_0^\xi\ \mathbf{P}_0^\eta\right\}^T$. The entire set of control parameters can be thought of as a vector $\left\{\mathbf{P}_0^\xi\ \mathbf{P}_0^\eta\ \mathbf{P}_J^\xi\ \mathbf{P}_I^\eta\right\}^T \equiv \mathbf{P}$.

There are numerous algebraic grid generation techniques which can be deduced from transfinite interpolation formulation. The most successful techniques, however, have been those that provide adequate othogonality control and grid spacing

control with reasonable function complexity [48]. A prime example of such technique would be the two-boundary technique described by Smith [46], using Hermite cubic interpolation functions in one coordinate direction between two opposing boundaries. In the remaining coordinate direction, linear interpolation between opposing boundaries is specified. This is the technique employed in this study and its development and implementation will be the subject of next section. Another notable technique is the application of transfinite interpolation using Lagrangian interpolation functions, where two, three, or four surfaces are specified in each direction for better grid control [29,49]. Detailed formulation of this technique applied to generic airplane configuration of Fig. 3.3a is outlined in Appendix A. The multi-surface method of Eiseman [48] is also another popular grid generation tool. It is a very flexible univariate scheme and is similar to Bezier and B-Spline approximation, where the parameters defining the surface are not necessarily on the surface itself [50,51].

3.5 Two-Boundary Grid Generation Technique

An interactive univariate version of Eq.(3.5) using only the normal interpolant **V** is developed. This, called *Two-Boundary Grid Generation Technique* (TBGG), matches both the function and its first derivative at two opposing boundaries. An analytical approximation of the physical coordinates can be expressed as

$$x = x_1(r,\mathbf{P}_1^\xi)\beta_1^0(t,\mathbf{P}_0^\eta) + R(r)\frac{\partial x_1(r,\mathbf{P}_1^\xi)}{\partial t}\beta_1^1(t,\mathbf{P}_0^\eta)$$
$$+ x_2(s,\mathbf{P}_2^\xi)\beta_2^0(t,\mathbf{P}_0^\eta) + S(s)\frac{\partial x_2(s,\mathbf{P}_2^\xi)}{\partial t}\beta_2^1(t,\mathbf{P}_0^\eta) \tag{3.9}$$

$$y = y_1(r,\mathbf{P}_1^\xi)\beta_1^0(t,\mathbf{P}_0^\eta) + R(r)\frac{\partial y_1(r,\mathbf{P}_1^\xi)}{\partial t}\beta_1^1(t,\mathbf{P}_0^\eta)$$
$$+ y_2(s,\mathbf{P}_2^\xi)\beta_2^0(t,\mathbf{P}_0^\eta) + S(s)\frac{\partial y_2(s,\mathbf{P}_2^\xi)}{\partial t}\beta_2^1(t,\mathbf{P}_0^\eta) \tag{3.10}$$

where

$$\beta_1^0(t,\mathbf{P}_0^\eta) = 2t^3 - 3t^2 + 1,$$

$$\beta_1^1(t, \mathbf{P}_0^\eta) = t^3 - 2t^2 + t,$$

$$\beta_2^0(t, \mathbf{P}_0^\eta) = -2t^3 + 3t^2,$$

$$\beta_2^1(t, \mathbf{P}_0^\eta) = t^3 - t$$

and

$$0 \leq t \leq 1.$$

Figure 3.5 presents the parametric representation of the boundaries and the cubic connecting function of Eqs.(3.9) and (3.10). The Hermite cubic blending functions are shown in Fig. 3.6.

Five functions $r = f_1(\xi)$, $s = f_2(\xi)$, $R(r) = K_1 f_3(\xi)$, $S(s) = K_2 f_4(\xi)$, $t = f_5(\eta)$, and their implied defining parameters control the grid spacing on the boundaries and the interior grid. Functions r and s define the grid spacing for lower and upper boundaries respectively, while $R(r)$ and $S(s)$ specify the orthogonality along those boundaries. The parameter t defines the grid distribution for the connecting curves between the two boundaries. The quantities K_1 and K_2 are parameters that scale the magnitude of the orthogonality at the boundaries. Increasing K_1 and K_2 extends the orthogonality of the grid into the interior domain. Excessively large values of K_1 and K_2 can also cause the grid lines to intersect themselves, which is not a desirable phenomenon.

For a wing-section example, the domain has been decomposed into an upper and lower section as shown in Fig. 3.7. For the streamwise direction, a bi-exponential distribution function with $B_1 = 4.5$ and inflection point coordinates $\{X = 0.3, Y = 0.2\}$ has been chosen for wing-section surface. The relationship, using Eq. (3.2) for $m = 3$, can be expressed as

$$r_{upper} = r_{lower} = Y\left[\frac{e^{B_1(\frac{\xi}{X})} - 1}{e^{B_1} - 1}\right] \qquad 0 \leq \xi \leq X$$

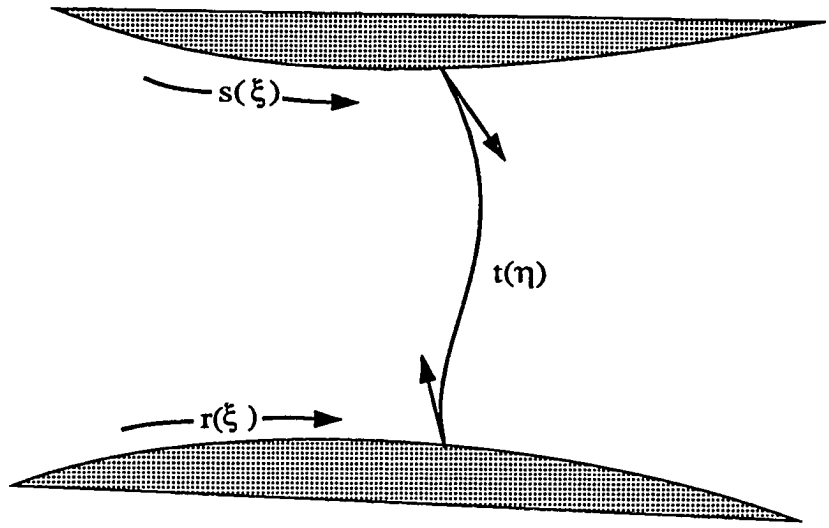

Fig. 3.5 Cubic function connecting upper and lower boundaries.

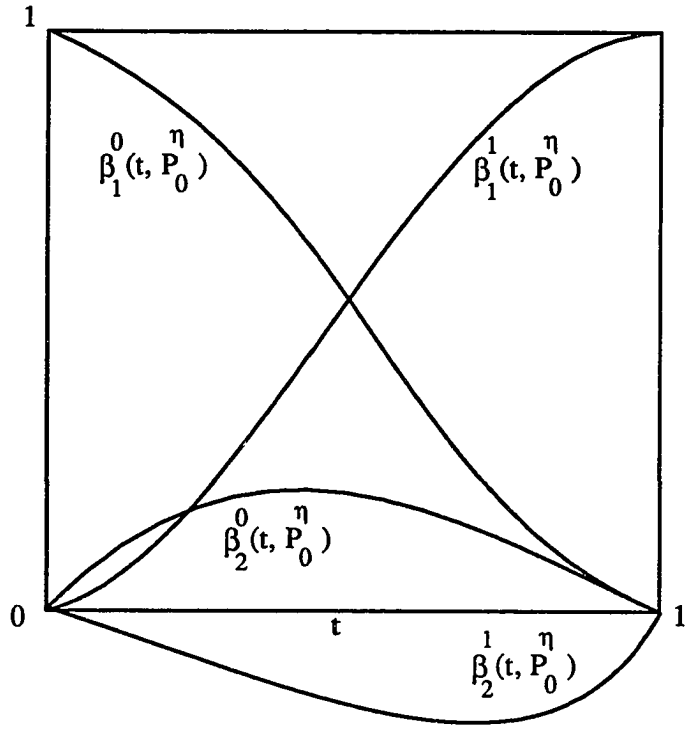

Fig. 3.6 Hermite cubic blending functions.

$$r_{upper} = r_{lower} = Y + (1-Y)\left[\frac{e^{B_2\left(\frac{\xi - X}{1-X}\right)} - 1}{e^{B_2} - 1}\right] \qquad X < \xi \leq 1. \tag{3.11}$$

The stretching parameter, B_2, is obtained by matching the slopes of the two exponential functions at $\{X, Y\}$. For NACA four-digit wing-section , the section coordinate $\{x_1(r, \mathbf{P}_1^\xi), y_1(r, \mathbf{P}_1^\xi)\}$, is acquired by invoking Eqs. (2.1-2.4) with

$$x = r_{upper} = r_{lower}. \tag{3.12}$$

For a geometric NURBS representation, Eq. (2.9) can be used with

$$r = r_{upper} = r_{lower} \tag{3.13}$$

in conjunction with a pre-determined set of control points, $\mathbf{D}_i$, and corresponding weights, ω_i. At the wake region, a single-exponential distribution function ($m = 2$) is chosen and, again, the grid continuity is preserved with matching the slopes of the distribution functions at the interface. Figure 3.8 shows the resultant discretization for upper portion of the domain. For the normal direction, a single hyperbolic tangent function such as

$$t = 1 + \frac{tanh[\frac{B_3}{2}(\eta - 1)]}{tanh(\frac{B_3}{2})} \qquad 0 < \eta \leq 1 \tag{3.14}$$

with $B_3 = 3.0$ is used, concentrating the grid near the wall for capturing the boundary layer effects. The grid orthogonality at surface for this particular example is obtained using the components of unit normal vector

$$\frac{\partial x_1(r, \mathbf{P}_1^\xi)}{\partial t} = \mp sin\theta \qquad \frac{\partial y_1(r, \mathbf{P}_1^\xi)}{\partial t} = \pm cos\theta \qquad \theta = tan^{-1}\left(\frac{\partial y_1(r, \mathbf{P}_1^\xi)}{\partial x_1(r, \mathbf{P}_1^\xi)}\right) \tag{3.15}$$

with a constant scaling parameter, (i.e., $R(r) = K_1 = 2.0$). For far-field boundary $\{x_2(s, \mathbf{P}_2^\xi), y_2(s, \mathbf{P}_2^\xi)\}$, essentially the same distribution as surface boundary can be adopted. The orthogonality at the far-field boundary has been ignored ($S(s) = K_2 = 0.0$). Figures 3.9 and 3.10 show sample grids for NACA 0012 and NACA 8512 sections using this procedure.

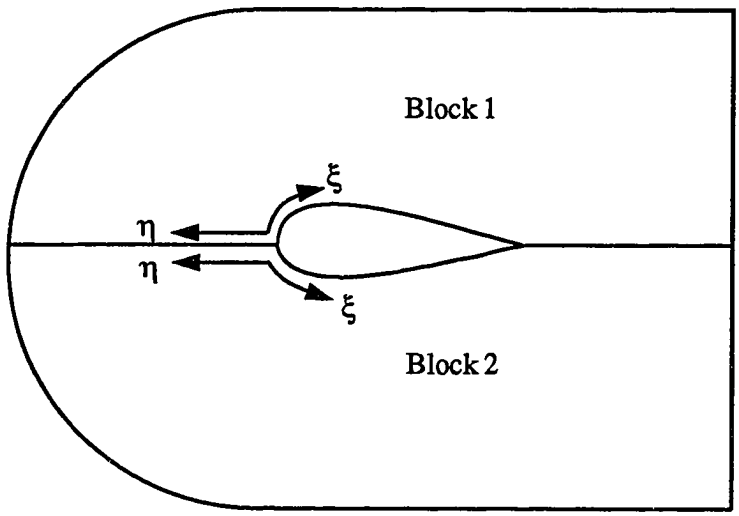

Fig. 3.7 Dual block domain decomposition.

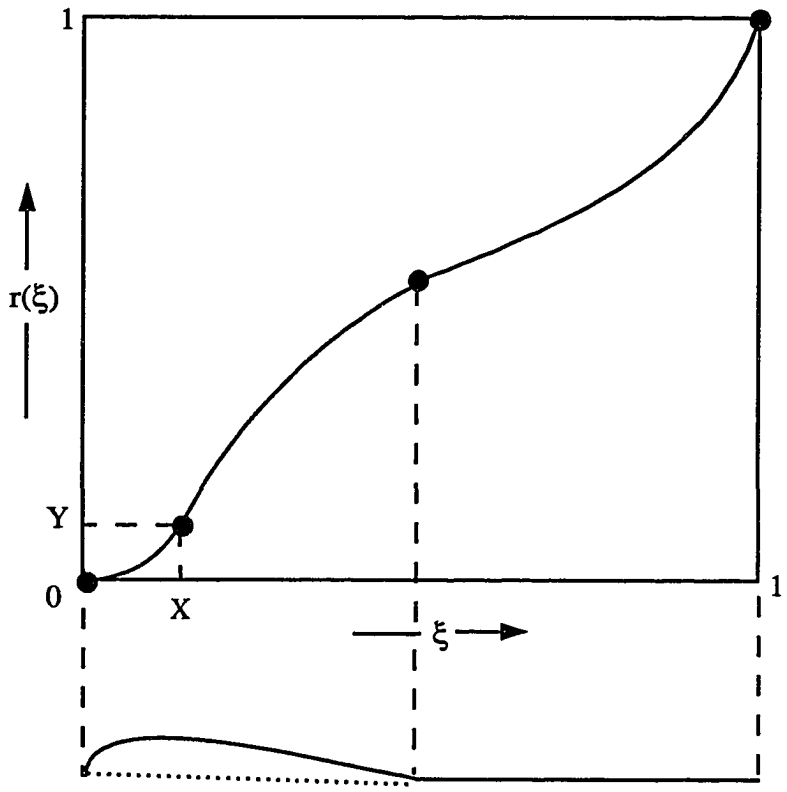

Fig. 3.8 Control domain for lower boundary discretization.

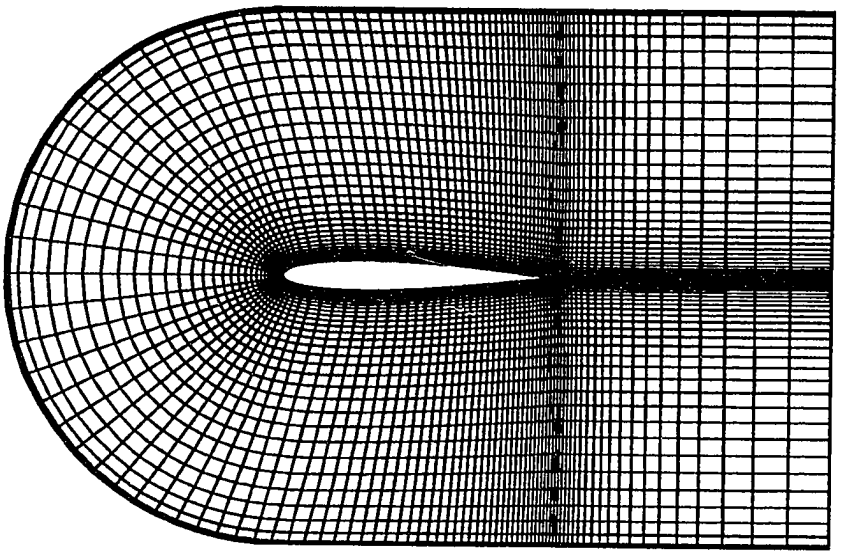

Fig. 3.9 Example grid for NACA 0012 wing-section

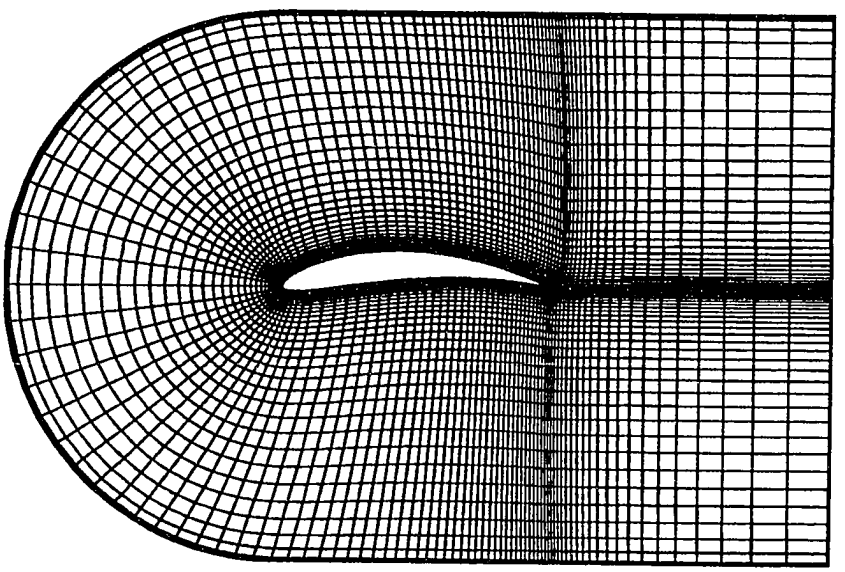

Fig. 3.10 Example grid for NACA 8512 wing-section

Chapter 4

THEORETICAL FORMULATION

4.1 Generic Sensitivity Equation

An implicit representation of a physical system can be modeled mathematically as

$$F(H, G(H)) = 0 \tag{4.1}$$

where G and H are dependent and independent variables, respectively. The function F can have algebraic, differential, integral or integral- differential characteristics. The quantities G and H can be either scalar or vector depending on the nature of the physical model. The sensitivity of G with respect to H can be obtained by implicit differentiation of Eq. (4.1)

$$\left\{\frac{\partial F}{\partial H}\right\} = -\left[\frac{\partial F}{\partial G}\right]\left\{\frac{\partial G}{\partial H}\right\} \tag{4.2}$$

The coefficients, $\left\{\frac{\partial F}{\partial H}\right\}$ and $[\frac{\partial F}{\partial G}]$, can be obtained, provided that the solution to Eq.(4.1) is known. Equation (4.2), now a set of algebraic equations, can be easily solved for the sensitivity derivative, $\left\{\frac{\partial G}{\partial H}\right\}$. If $\left\{\frac{\partial F}{\partial H}\right\}$ and $[\frac{\partial F}{\partial G}]$ are not available, a finite difference approach can be adopted. The central difference approximation of $\left\{\frac{\partial G}{\partial H}\right\}$ can be devised as

$$\left\{\frac{\partial G}{\partial H}\right\} \approx \frac{G(H + \Delta H) - G(H - \Delta H)}{2\Delta H} \tag{4.3}$$

where ΔH is a small perturbation of a specified parameter. Although the implementation of the finite difference approach is comparatively easy, it has the disadvantage

of being computationally expensive. Also, the choice of ΔH is crucial for accuracy of the derivative. A large values of ΔH may lead to inaccurate derivatives while a small value may result in round-off errors.

4.2 Aerodynamic Sensitivity Equation

Let $\mathbf{Q}$ be a solution of the Euler or Navier-Stokes equations on the domain $\mathbf{X}$ and $\mathbf{Q}^*$ be a discrete solution on the grid $\mathbf{X}$ where

$$\mathbf{Q} = \begin{Bmatrix} \rho \\ \rho u \\ \rho v \\ \rho w \\ e \end{Bmatrix}_{i,j,k} \qquad \mathbf{X} = \begin{Bmatrix} x \\ y \\ z \end{Bmatrix}_{i,j,k} \tag{4.4}$$

and

$$\frac{1}{J}\frac{\partial \mathbf{Q}}{\partial t} = \mathbf{R}(\mathbf{Q}). \tag{4.5}$$

Here, $\mathbf{R}$ is the residual and J is the transformation Jacobian

$$J = \frac{\partial(\xi, \eta, \zeta)}{\partial(x, y, z)}. \tag{4.6}$$

For two-dimensional thin-layer Navier-Stokes equations, the residual $\mathbf{R}$ can be expressed in generalized curvilinear coordinates (ξ, η) as [52],

$$\mathbf{R} = -\frac{\partial \bar{\mathbf{F}}}{\partial \xi} - \frac{\partial(\bar{\mathbf{G}} - \bar{\mathbf{G}}_{\mathbf{v}})}{\partial \eta} \tag{4.7}$$

where the inviscid flux vectors $\bar{\mathbf{F}}$ and $\bar{\mathbf{G}}$ are

$$\bar{\mathbf{F}} = \frac{1}{J}\begin{Bmatrix} \rho U \\ \rho U u + \xi_x P \\ \rho U v + \xi_y P \\ (e+P)U \end{Bmatrix} \qquad \bar{\mathbf{G}} = \frac{1}{J}\begin{Bmatrix} \rho V \\ \rho V u + \eta_x P \\ \rho V v + \eta_y P \\ (e+P)V \end{Bmatrix} \tag{4.8}$$

and U, V are the contravariant velocities defined as

$$U = \xi_x u + \xi_y v \qquad V = \eta_x u + \eta_y v. \tag{4.9}$$

The viscous flux vector $\bar{\mathbf{G}}_\mathbf{v}$ is

$$\bar{\mathbf{G}}_\mathbf{v} = \frac{1}{J}\begin{Bmatrix} 0 \\ \eta_x\tau_{xx} + \eta_y\tau_{xy} \\ \eta_x\tau_{xy} + \eta_y\tau_{yy} \\ \eta_x b_x + \eta_y b_y \end{Bmatrix} \tag{4.10}$$

with shear stress, τ, and heat flux, q, are written in indicial notations as

$$\tau_{x_i x_j} = \frac{M_\infty}{Re}\left[\mu\left(\frac{\partial u_i}{\partial x_j} + \frac{\partial u_j}{\partial x_i}\right) + \lambda\frac{\partial u_k}{\partial x_k}\delta_{ij}\right] \tag{4.11}$$

and

$$b_{x_i} = u_j\tau_{x_i x_j} + \left(\frac{M_\infty\mu}{RePr(\gamma-1)}\right)\frac{\partial a^2}{\partial x_i}, \tag{4.12}$$

where a represents the local speed of sound. The pressure is evaluated through the ideal gas law

$$P = (\gamma-1)[e - \rho(u^2+v^2)/2] \tag{4.13}$$

with γ, the specific heat ratio taken to be 1.4. The molecular viscosity, μ, is calculated from the Sutherland's law and Stoke's hypothesis for bulk viscosity, $\lambda = -\frac{2}{3}\mu$, is invoked.

For a steady-state solution (i.e., $t \to \infty$), Eq.(4.5) is reduces to

$$\mathbf{R}(\mathbf{Q}^*(\mathbf{P}), \mathbf{X}(\mathbf{P}), \mathbf{P}) = 0 \tag{4.14}$$

where the explicit dependency of $\mathbf{R}$ on grid and vector of parameters $\mathbf{P}$ is evident. The parameters $\mathbf{P}$ control the grid $\mathbf{X}$ as well as the solution $\mathbf{Q}^*$. The fundamental sensitivity equation containing $\left\{\frac{\partial \mathbf{Q}^*}{\partial \mathbf{P}}\right\}$ and described by Taylor et al. [13] is obtained by direct differentiation of Eq.(4.14) as

$$\left[\frac{\partial \mathbf{R}}{\partial \mathbf{Q}}\right]\left\{\frac{\partial \mathbf{Q}^*}{\partial \mathbf{P}}\right\} + \left[\frac{\partial \mathbf{R}}{\partial \mathbf{X}}\right]\left\{\frac{\partial \mathbf{X}}{\partial \mathbf{P}}\right\} + \left\{\frac{\partial \mathbf{R}}{\partial \mathbf{P}}\right\} = 0. \tag{4.15}$$

For a non-geometric design parameter (e.g. angle of attack or free-stream Mach number), the grid will not be effected by changes in $\mathbf{P}$ and Eq.(4.15) reduces to

$$\left[\frac{\partial \mathbf{R}}{\partial \mathbf{Q}}\right]\left\{\frac{\partial \mathbf{Q}^*}{\partial \mathbf{P}}\right\} + \left\{\frac{\partial \mathbf{R}}{\partial \mathbf{P}}\right\} = 0. \tag{4.16}$$

For a geometric design parameter (e.g. camber of an airfoil), the direct dependency of residual on $\mathbf{P}$ will vanish since the changes in $\mathbf{P}$ would propagate through the grid. Equation (4.15) becomes

$$\left[\frac{\partial \mathbf{R}}{\partial \mathbf{Q}}\right]\left\{\frac{\partial \mathbf{Q}^*}{\partial \mathbf{P}}\right\} + \left[\frac{\partial \mathbf{R}}{\partial \mathbf{X}}\right]\left\{\frac{\partial \mathbf{X}}{\partial \mathbf{P}}\right\} = 0. \tag{4.17}$$

It is important to notice that Eq.(4.17) is a set of linear algebraic equations , and the matrices $[\frac{\partial \mathbf{R}}{\partial \mathbf{Q}}]$ and $[\frac{\partial \mathbf{R}}{\partial \mathbf{X}}]$ are well understood [12]. The vector quantity $\left\{\frac{\partial \mathbf{Q}^*}{\partial \mathbf{P}}\right\}$ is the solution to Eq.(4.17) given the sensitivity of the grid with respect to the parameters,$\left\{\frac{\partial \mathbf{X}}{\partial \mathbf{P}}\right\}$. A direct chain rule differentiation of $\left\{\frac{\partial \mathbf{X}}{\partial \mathbf{P}}\right\}$ results in

$$\left\{\frac{\partial \mathbf{X}}{\partial \mathbf{P}}\right\} = \left[\frac{\partial \mathbf{X}}{\partial \mathbf{X}_B}\right]\left\{\frac{\partial \mathbf{X}_B}{\partial \mathbf{P}}\right\} \tag{4.18}$$

where $\mathbf{X}_B$ designates the boundary coordinates. The vector $\left\{\frac{\partial \mathbf{X}_B}{\partial \mathbf{P}}\right\}$ represents the boundary sensitivity which is directly related to boundary parameterization, discussed in the next section. It has the importance of being one of the dominant factors in calculating the sensitivity of surface forces needed for optimization process. The matrix $[\frac{\partial \mathbf{X}}{\partial \mathbf{X}_B}]$ is responsible for field grid sensitivity with respect to boundary coordinates and it is related to the rules which govern the grid generation algorithm. For algebraic generation systems, the primary components of $[\frac{\partial \mathbf{X}}{\partial \mathbf{X}_B}]$, are the interpolation functions which distribute the interior grid.

An approximate version of Eq. (4.17) is suggested for predicting the steady-state solution changes which occur in response to small but finite boundary changes. The essence of using approximate analysis is to reduce the number of expensive flow analyses required during the optimization process. A Taylor series expansion of the $\mathbf{Q}^*(\mathbf{P}+\Delta\mathbf{P})$ about $\mathbf{P}$ is derived as

$$\mathbf{Q}^*(\mathbf{P}+\Delta\mathbf{P}) \approx \mathbf{Q}^*(\mathbf{P}) + \left(\frac{\partial \mathbf{Q}^*}{\partial \mathbf{P}}\right)\Delta\mathbf{P} + \ldots\ldots \tag{4.19}$$

Disregarding the higher order terms and substituting for $\left\{\frac{\partial \mathbf{Q}^*}{\partial \mathbf{P}}\right\}$ from Eq. (4.17), Eq. (4.19) becomes

$$\frac{\partial \mathbf{R}}{\partial \mathbf{Q}}\Delta\mathbf{Q}^* \approx -\frac{\partial \mathbf{R}}{\partial \mathbf{P}}\Delta\mathbf{P} \tag{4.20}$$

where

$$\Delta \mathbf{Q}^* = \mathbf{Q}^*(\mathbf{P} + \Delta \mathbf{P}) - \mathbf{Q}^*(\mathbf{P})$$

It is essential to understand that the approximate analysis is valid as long as the changes in the boundary shape are small (i.e., $\Delta \mathbf{P} \ll 1$). Figure 4.1 exhibits the non-linear relation between drag coefficient and thickness parameter ($\mathbf{P} = T$) for class of symmetrical wing-sections, enforcing the above argument.

4.3 Surface Parameterization

An integral part of the grid sensitivity analysis is the boundary parameterization. The process is to define the major control surfaces with independent design parameters. The most general parameterization of the boundaries would be to specify every grid point as a parameter. This conceivably could be desirable for the boundaries corresponding to complex geometries to allow a design procedure to have the greatest possible flexibility. However, it is impractical from a computational point of view. Another approach would be a quasi-analytical parameterization in term of design variables. For instance, a class of wing-sections is specified by two camber-line parameters and a thickness distribution parameter; a wing is specified by several wing-sections; and the wing surface is interpolated from the sections. In this manner, an airplane component can be specified by tens of parameters instead of hundreds or thousands of parameters. Such physical parameterization with global boundary control does not possess a great deal of generality necessary for high level design and optimization analysis.

A compromise between totally geometric and physical parameterization is to approximate the desired boundary using a spline function such as NURBS as discussed in Chap. 2. In the design process, using NURBS in conjunction with an interactive Computer Aided Design (CAD) system, would be highly advantageous [24]. After

prescribing an initial set of control points, the designer can pick and drag points while simultaneously observe the change in the shape of the surface. Although there are some qualifications and reservations, this approach is advocated for optimization of aerospace-vehicle configuration designs.

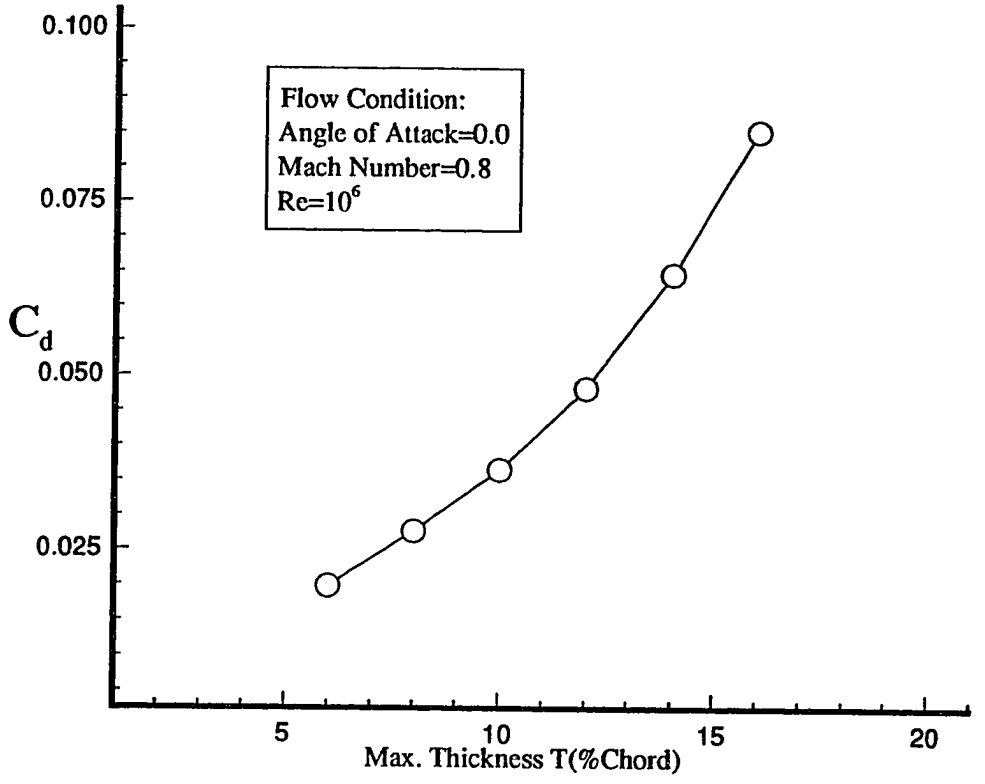

Fig. 4.1 Coefficient of drag versus maximum thickness T for symmetrical wing-section.

Chapter 5

METHOD OF SOLUTION

5.1 Introduction

As stated previously, the simplest way to obtain grid sensitivity is to vary the control parameters, one at a time, and finite difference the results. This, however, is proven to be computationally inefficient compared to analytical or semi-analytical differentiation of the grid equations. Also, the proper choice of a step size is not trivial and an improper choice might result in round-off error accumulation. The finite difference approach should only be used as the last resort when the extreme complexity of the grid equations dictates no other alternatives. For a less complicated grid equations, a semi-analytical approach would be more appropriate. The semi-analytical approach consists of analytical differentiation of the original function with respect to an intermediate function, the derivative of which is then evaluated numerically. It combines the efficiency of the analytical approach with the ease of implementation of the finite difference approach.

The analytical approach to the grid sensitivity problem is evaluation of the grid sensitivity coefficient by direct analytical differentiation of the grid equation. For most cases, the grid equation is not directly differentiable, although there are schemes that such differentiations are feasible. The algebraic grid generation schemes, such as *Two-Boundary Grid Generation* (TBGG) used in this study, fall within that category. The grids are governed by explicit algebraic relations where the direct differentiation of the equations are not complicated. The analytical approach has the advantage of

being exact, thus, avoids the round-off errors associated with numerical approaches.

There are two types of parameters involved in this study. First, there are the design parameters which specify the shape of the primary boundary. For classical NACA four-digit wing-sections, the design parameters are camber, M, location of camber, C, and maximum thickness, T. For a geometric NURBS representation, the design parameters are the control point coordinates, $\mathbf{D}_i = \{X_i, Y_i\}$, and their corresponding weights, ω_i. Secondly, there are grid parameters that define other boundaries and the spacing between grid points. The location of far-field boundary, L, grid stretching parameter normal to the wall, B_3, grid stretching parameter along the wall, B_1, and magnitude of normal derivatives along bottom and top boundaries, K_1 and K_2, are prime examples of such parameters. The two sets of parameters are not functionally dependent and can be treated separately.

5.2 Grid Sensitivity with respect to Design Parameters

Here we express, the sensitivity of the grid with respect to the vector of design parameters $\mathbf{X}_D$. As a consequence of using algebraic grid generation technique in which the boundary grid has the dominant effect on the interior grid, the boundary grid sensitivity coefficient would also be essential in influencing the interior grid sensitivity coefficient. Therefore, evaluation of the surface grid sensitivity coefficients, $\left\{\frac{\partial x_1(r,\mathbf{P}_1^\xi)}{\partial \mathbf{X}_D}\right\}$ and $\left\{\frac{\partial y_1(r,\mathbf{P}_1^\xi)}{\partial \mathbf{X}_D}\right\}$, are the most important part of the analysis and directly dependent to the surface parameterization.

Two distinct techniques are outlined in the Chap. 2 for wing-section parameterization. The first technique, using the analytical relations of Eqs.(2.1-2.4), yields the classical representation of NACA four-digit wing- sections. The second technique, using an approximative (NURBS) relations of Eq.(2.9), would result in defining any free-form surface, although, the focus here would be on a wing-section geometry. For

practical purposes, the grid sensitivity and orthogonality at the far-field boundary has been ignored, (i.e., $\left\{\frac{\partial x_2(s,\mathbf{P}_2^\xi)}{\partial \mathbf{X}_D}\right\} = \left\{\frac{\partial y_2(s,\mathbf{P}_2^\xi)}{\partial \mathbf{X}_D}\right\} = S(s) = 0$). The evaluation of the grid sensitivity using analytical parameterization will be discussed first.

A direct differentiation of Eqs.(3.9) and (3.10) with respect to $\mathbf{X}_D$ results in

$$\frac{\partial x}{\partial \mathbf{X}_D} = \beta_1^0(t,\mathbf{P}_0^\eta)\frac{\partial x_1(r,\mathbf{P}_1^\xi)}{\partial \mathbf{X}_D} + R(r)\beta_1^1(t,\mathbf{P}_0^\eta)\frac{\partial x_1'(r,\mathbf{P}_1^\xi)}{\partial \mathbf{X}_D} \tag{5.1}$$

$$\frac{\partial y}{\partial \mathbf{X}_D} = \beta_1^0(t,\mathbf{P}_0^\eta)\frac{\partial y_1(r,\mathbf{P}_1^\xi)}{\partial \mathbf{X}_D} + R(r)\beta_1^1(t,\mathbf{P}_0^\eta)\frac{\partial y_1'(r,\mathbf{P}_1^\xi)}{\partial \mathbf{X}_D} \tag{5.2}$$

where

$$\mathbf{X}_D = \{T, M, C\}^T. \tag{5.3}$$

The prime indicates differentiation with respect to t and can be substituted from Eq.(3.15). Since $x_1(r,\mathbf{P}_1^\xi)$ is independent of design parameters $\mathbf{X}_D$, then

$$\frac{\partial x_1(r,\mathbf{P}_1^\xi)}{\partial \mathbf{X}_D} = 0. \tag{5.4}$$

The x coordinate sensitivity, Eq.(5.1), can now be reduced to

$$\frac{\partial x}{\partial \mathbf{X}_D} = R(r)\beta_1^1(t,\mathbf{P}_0^\eta)\frac{\partial(\mp sin\theta)}{\partial \mathbf{X}_D}. \tag{5.5}$$

Using the relation

$$\frac{\partial}{\partial \mathbf{X}_D} tan^{-1}u = \frac{1}{1+u^2}\frac{\partial u}{\partial \mathbf{X}_D} \tag{5.6}$$

the x coordinate sensitivity becomes

$$\frac{\partial x}{\partial \mathbf{X}_D} = \mp R(r)\beta_1^1(t,\mathbf{P}_0^\eta)cos\theta \frac{1}{1+\left(\frac{\partial y_1(r,\mathbf{P}_1^\xi)}{\partial x_1(r,\mathbf{P}_1^\xi)}\right)^2}\frac{\partial}{\partial \mathbf{X}_D}\left\{\frac{\partial y_1(r,\mathbf{P}_1^\xi)}{\partial x_1(r,\mathbf{P}_1^\xi)}\right\}. \tag{5.7}$$

The term $\frac{\partial}{\partial \mathbf{X}_D}\left\{\frac{\partial y_1(r,\mathbf{P}_1^\xi)}{\partial x_1(r,\mathbf{P}_1^\xi)}\right\}$ can be evaluated by direct differentiation of Eq.(2.4). The y coordinate sensitivity with respect to design parameters can be obtained using similar procedure. Equation (5.2) can be modified to

$$\frac{\partial y}{\partial \mathbf{X}_D} = \beta_1^0(t,\mathbf{P}_0^\eta)\frac{\partial y_1(r,\mathbf{P}_1^\xi)}{\partial \mathbf{X}_D} \mp R(r)\beta_1^1(t,\mathbf{P}_0^\eta)sin\theta \frac{1}{1+\left(\frac{\partial y_1(r,\mathbf{P}_1^\xi)}{\partial x_1(r,\mathbf{P}_1^\xi)}\right)^2}\frac{\partial}{\partial \mathbf{X}_D}\left\{\frac{\partial y_1(r,\mathbf{P}_1^\xi)}{\partial x_1(r,\mathbf{P}_1^\xi)}\right\}. \tag{5.8}$$

All terms at the right hand side of Eqs.(5.7) and (5.8) can be evaluated explicitly due to analytical parameterization of the surface for this particular geometry.

The grid sensitivity using the NURBS parameterization is established using Eqs.(5.1) and (5.2) where

$$\mathbf{X}_D = \{X_i, Y_i, \omega_i\}^T \qquad i = 0, ..., n. \tag{5.9}$$

The surface grid sensitivity coefficients, $\left\{\frac{\partial x_1(r,\mathbf{P}_1^\xi)}{\partial \mathbf{X}_D}, \frac{\partial y_1(r,\mathbf{P}_1^\xi)}{\partial \mathbf{X}_D}\right\}$, are obtained by direct differentiation of Eq.(2.9) with respect to $\mathbf{X}_D$ as

$$\frac{\partial x_1(r,\mathbf{P}_1^\xi)}{\partial X_i} = \frac{\partial y_1(r,\mathbf{P}_1^\xi)}{\partial Y_i} = R_{i,p}(r) \tag{5.10}$$

$$\frac{\partial x_1(r,\mathbf{P}_1^\xi)}{\partial Y_i} = \frac{\partial y_1(r,\mathbf{P}_1^\xi)}{\partial X_i} = 0. \tag{5.11}$$

For the weight function, we have

$$\frac{\partial \mathbf{X}}{\partial \omega_i} = \sum_{i=0}^{n} \frac{\partial R_{i,p}(r)}{\partial \omega_k}\mathbf{D}_i \tag{5.12}$$

where

$$\mathbf{X} = \begin{Bmatrix} x_1(r,\mathbf{P}_1^\xi) \\ y_1(r,\mathbf{P}_1^\xi) \end{Bmatrix} \quad , \quad \mathbf{D}_i = \begin{Bmatrix} X_i \\ Y_i \end{Bmatrix}$$

and

$$\frac{\partial R_{i,p}(r)}{\partial \omega_k} = \begin{Bmatrix} \frac{-N_{k,p}(r)N_{i,p}(r)\omega_i}{\sum_{j=0}^{n} N_{j,p}(r)\omega_i} & k \neq i \\ \frac{N_{k,p}(r)\sum_{j=0}^{n} N_{j,p}(r)\omega_j - N_{k,p}(r)N_{i,p}(r)\omega_i}{\sum_{j=0}^{n} N_{j,p}(r)\omega_j} & k = i \end{Bmatrix}. \\ k, i = 0, ..., n$$

In the preceding equation, $R_{i,p}(r)$ and $N_{i,p}(r)$ are the basis function of the rational and non-rational B-splines as defined in Chap. 2.

5.3 Grid Sensitivity with respect to Grid Parameters

The sensitivity of grid with respect to vector of grid parameters $\mathbf{X}_G$ has a significant impact on grid optimization and adaption. The $\mathbf{X}_G$ represents, as mentioned earlier, the parameters that govern the surfaces other than vehicle surface and the parameters that control the grid spacing. Among those parameters, grid stretching parameter along the wall B_1 and grid stretching normal to the wall B_3 are of great importance and require more attention. The grid sensitivity with respect to B_1 is obtained as

$$\frac{\partial x}{\partial B_1} = \beta_t^0(t, \mathbf{P}_0^\eta)\frac{\partial x_1(r, \mathbf{P}_1^\xi)}{\partial B_1} + R(r)\beta_1^1(t, \mathbf{P}_1^\xi)\frac{\partial x_1'(r, \mathbf{P}_1^\xi)}{\partial B_1} \tag{5.13}$$

$$\frac{\partial y}{\partial B_1} = \beta_t^0(t, \mathbf{P}_0^\eta)\frac{\partial y_1(r, \mathbf{P}_1^\xi)}{\partial B_1} + R(r)\beta_1^1(t, \mathbf{P}_1^\xi)\frac{\partial y_1'(r, \mathbf{P}_1^\xi)}{\partial B_1} \tag{5.14}$$

The term $\frac{\partial x_1(r,\mathbf{P}_1^\xi)}{\partial B_1}$ can be obtained by direct differentiation of Eq.(3.11) for a bi-exponential distribution function as

$$\frac{\partial x_1(r, \mathbf{P}_1^\xi)}{\partial B_1} = Y\left[\frac{(\frac{\xi}{X}e^{\frac{B_1}{X}\xi})(e^{B_1}-1) - e^{B_1}(e^{\frac{B_1}{X}\xi}-1)}{(e^{B_1}-1)^2}\right] \qquad 0 \le \xi \le X \tag{5.15}$$

and

$$\frac{\partial x_1(r, \mathbf{P}_1^\xi)}{\partial B_1} = (1-Y)\left(\frac{\partial B_2}{\partial B_1}\right)\left[\frac{A(e^{B_2}-1)e^{B_2 A} - e^{B_2}(e^{B_2 A}-1)}{(e^{B_2}-1)^2}\right] \qquad X \le \xi \le 1 \tag{5.16}$$

where $A = \frac{\xi - X}{1-X}$ and X and Y are the inflection point coordinates for a bi-exponential distribution function. The quantities B_2 and $\left\{\frac{\partial B_2}{\partial B_1}\right\}$ can be determined using Newton's iterative scheme. The term $\left\{\frac{\partial y_1(r,\mathbf{P}_1^\xi)}{\partial B_1}\right\}$ can be evaluated using the chain rule differentiation

$$\frac{\partial y_1(r, \mathbf{P}_1^\xi)}{\partial B_1} = \left\{\frac{\partial y_1(r, \mathbf{P}_1^\xi)}{\partial x_1(r, \mathbf{P}_1^\xi)}\right\}\left\{\frac{\partial x_1(r, \mathbf{P}_1^\xi)}{\partial B_1}\right\}. \tag{5.17}$$

The grid sensitivity with respect to the stretching parameter normal to wall ,B_3, is

$$\frac{\partial x}{\partial B_3} = x_1(r, \mathbf{P}_1^\xi)\frac{\partial \beta_1^0(t, \mathbf{P}_0^\eta)}{\partial t}\frac{\partial t}{\partial B_3} + R(r)x_1'(r, \mathbf{P}_1^\xi)\frac{\partial \beta_1^1(t, \mathbf{P}_0^\eta)}{\partial t}\frac{\partial t}{\partial B_3}$$

$$+ x_2(r, \mathbf{P}_2^\xi)\frac{\partial \beta_2^0(t, \mathbf{P}_0^\eta)}{\partial t}\frac{\partial t}{\partial B_3} + S(s)x_2'(s, \mathbf{P}_2^\xi)\frac{\partial \beta_2^1(t, \mathbf{P}_0^\eta)}{\partial t}\frac{\partial t}{\partial B_3} \tag{5.18}$$

and

$$\frac{\partial y}{\partial B_3} = y_1(r, \mathbf{P}_1^\xi)\frac{\partial \beta_1^0(t, \mathbf{P}_0^\eta)}{\partial t}\frac{\partial t}{\partial B_3} + R(r)y_1'(r, \mathbf{P}_1^\xi)\frac{\partial \beta_1^1(t, \mathbf{P}_0^\eta)}{\partial t}\frac{\partial t}{\partial B_3}$$
$$+ y_2(r, \mathbf{P}_2^\xi)\frac{\partial \beta_2^0(t, \mathbf{P}_0^\eta)}{\partial t}\frac{\partial t}{\partial B_3} + S(s)y_2'(s, \mathbf{P}_2^\xi)\frac{\partial \beta_2^1(t, \mathbf{P}_0^\eta)}{\partial t}\frac{\partial t}{\partial B_3} \tag{5.19}$$

where

$$\frac{\partial \beta_1^0(t, \mathbf{P}_0^\eta)}{\partial t} = 6t^2 - 6t \quad \frac{\partial \beta_1^1(t, \mathbf{P}_0^\eta)}{\partial t} = 3t^2 - 4t + 1$$
$$\frac{\partial \beta_2^0(t, \mathbf{P}_0^\eta)}{\partial t} = -6t^2 + 6t \quad \frac{\partial \beta_2^2(t, \mathbf{P}_0^\eta)}{\partial t} = 3t^2 - 1.$$

Differentiating of Eq.(3.14) for a hyperbolic tangent stretching function yields to

$$\frac{\partial t}{\partial B_3} = \frac{(\eta - 1)sech^2[\frac{B_3}{2}(\eta - 1)]tanh(\frac{B_3}{2}) - sech^2(\frac{B_3}{2})tanh[\frac{B_3}{2}(\eta - 1)]}{2[tanh(\frac{B_3}{2})]^2} \tag{5.20}$$

Similar developments can be extended to other grid control parameters such as the far-field boundary location, L, and the magnitude of orthogonality vector at the boundaries, K_1 and K_2.

5.4 Flow Analysis and Boundary Conditions

The two-dimensional thin-layer Navier-Stokes equations are solved in their conservation form using an upwind cell-centered finite-volume formulation. A third-order accurate upwind biased inviscid flux balance is used in both streamwise and normal directions. The finite-volume equivalent of second-order accurate central differences is used for viscous terms. The resulting discretization represents the residual, $\mathbf{R}(\mathbf{Q})$, at each cell depending locally on values of $\mathbf{Q}$ at nine neighboring cells such that

$$\mathbf{R}_{i,j}(\mathbf{Q}) = \mathbf{R}_{i,j}(\mathbf{Q}_{i,j}, \mathbf{Q}_{i,j-1}, \mathbf{Q}_{i,j+1}, \mathbf{Q}_{i,j-2}, \mathbf{Q}_{i,j+2}, \mathbf{Q}_{i-1,j}, \mathbf{Q}_{i+1,j}, \mathbf{Q}_{i-2,j}, \mathbf{Q}_{i+2,j}). \tag{5.21}$$

The discretized governing equations are implicitly advanced in time using Euler implicit method which is unconditionally stable for all time steps according to Fourier stability analysis [52]. A first-order Taylor's series expansion of the right hand side of Eq.(4.5) results in

$$\left[\frac{1}{J\Delta t} - \frac{\partial \mathbf{R}^n}{\partial \mathbf{Q}}\right]\Delta\mathbf{Q} = \mathbf{R}^n(\mathbf{Q}) \tag{5.22}$$

$$\Delta\mathbf{Q} = \mathbf{Q}^{n+1} - \mathbf{Q}^n \quad n = 1, 2, 3....$$

where n represents the time level. The field variables for the new time level, $\mathbf{Q}^{n+1}$, can be obtained by solving Eq.(5.22) for $\Delta\mathbf{Q}$. The coefficient matrix, $\left[\frac{\partial \mathbf{R}}{\partial \mathbf{Q}}\right]$, is a sparse square matrix with a block-banded structure of at most nine 4x4 block diagonals. An iterative approximate factorization (AF) algorithm have been chosen to advance the solution in time until

$$\mathbf{R}(\mathbf{Q}^*) \approx 0 \tag{5.23}$$

where $\mathbf{Q}^*$ are the steady-state values of the field variables. The inviscid flux vectors are evaluated using the upwind flux vector splitting of Van Leer [53]. For an infinitely large time steps, (i.e., $\Delta t \rightarrow \infty$) the non-linear system of Eq.(5.22) may be directly solved using Newton's method [14,54]. The boundary conditions are implicitly implemented within the governing equations. The airfoil surface is considered to be impermeable and adiabatic. A standard no-slip boundary condition with zero surface velocity has been selected. The pressure at the surface is evaluated using a zeroth-order extrapolation from the interior cells. The density is then calculated using the state equation, Eq.(4.13). Consequently,

$$u = 0, \quad v = 0, \quad \frac{\partial \bar{T}}{\partial \mathbf{n}} = 0, \quad \frac{\partial P}{\partial \mathbf{n}} = 0 \tag{5.24}$$

where $\bar{T}$ represents the adiabatic surface temperature and $\mathbf{n}$ is the unit normal vector of the surface. In the far-field, assuming a locally one-dimensional flow, Riemann invariants are employed as

$$R^{\pm} = U \pm \frac{2a}{\gamma - 1}. \tag{5.25}$$

Adding and subtracting these two equations would yield to local normal velocity and speed of sound. A periodic boundary condition is applied along the wake-cut which resulted from a C-type grid. The effects of different boundary conditions on the coefficient matrix $\left[\frac{\partial \mathbf{R}}{\partial \mathbf{Q}}\right]$ are extremely important as outline in [13,54]. For example, the periodic boundary condition will cause the matrix $\left[\frac{\partial \mathbf{R}}{\partial \mathbf{Q}}\right]$ to deviate from its original neat banded structure with some non-zero coefficients outside of central bandwidth [54]. This restructuring will greatly effect the procedure for solving the aerodynamic sensitivity equation to be discussed in the next section.

5.5 Flow Sensitivity Analysis

The flow sensitivity coefficient $\left\{\frac{\partial \mathbf{Q}^*}{\partial \mathbf{P}}\right\}$ can now be directly obtained using the fundamental sensitivity equation, Eq.(4.17), as

$$\left\{\frac{\partial \mathbf{Q}^*}{\partial \mathbf{P}}\right\} = -\left[\frac{\partial \mathbf{R}}{\partial \mathbf{Q}}\right]^{-1}\left[\frac{\partial \mathbf{R}}{\partial \mathbf{X}}\right]\left\{\frac{\partial \mathbf{X}}{\partial \mathbf{P}}\right\} \tag{5.26}$$

provided that grid sensitivity, $\left\{\frac{\partial \mathbf{X}}{\partial \mathbf{P}}\right\}$, is known. The Jacobian matrix, $\left[\frac{\partial \mathbf{R}}{\partial \mathbf{X}}\right]$, can be evaluated by differentiating the discrete residuals $\mathbf{R}_{i,j}$ with respect to four vertices of each cell. Since for a typical C-type grid, the stream-wise (I-dimension) of the grid is significantly larger than normal (J-dimension), a J-ordering of the Eq.(5.26) will be implemented. This, will substantially reduce the memory requirements due to smaller central bandwidth of $\left[\frac{\partial \mathbf{R}}{\partial \mathbf{Q}}\right]$. The quantity $\left[\frac{\partial \mathbf{R}}{\partial \mathbf{Q}}\right]^{-1}$ can be obtained using a full matrix solver to account for all the non-zero contributions outside of central bandwidth. This, although convenient, is not practical for Navier-Stokes equations due to large storage requirements. An alternative would be the use of a hybrid direct solver with conventional relaxation strategy implemented in two steps. The coefficient matrix $\left[\frac{\partial \mathbf{R}}{\partial \mathbf{Q}}\right]$ can be splitted into two matrices as

$$-\left[\frac{\partial \mathbf{R}}{\partial \mathbf{Q}}\right] = [\mathbf{M}] + [\mathbf{N}] \tag{5.27}$$

where [M] represents the banded part of the $\left[\frac{\partial \mathbf{R}}{\partial \mathbf{Q}}\right]$ and [N] represents entries outside the band. The linear system of Eq.(5.26) can now be solved using the Richardson's iteration

$$\left\{\frac{\partial \mathbf{Q}^*}{\partial \mathbf{P}}\right\}^k = +[\mathrm{M}]^{-1}\left[\frac{\partial \mathbf{R}}{\partial \mathbf{X}}\right]\left\{\frac{\partial \mathbf{X}}{\partial \mathbf{P}}\right\} - [\mathrm{M}]^{-1}[\mathrm{N}]\left\{\frac{\partial \mathbf{Q}^*}{\partial \mathbf{P}}\right\}^{k-1} \qquad (5.28)$$

$$k = 1, kmax$$

where $\left\{\frac{\partial \mathbf{Q}^*}{\partial \mathbf{P}}\right\}^0$ is assumed to be zero and $[\mathrm{M}]^{-1}$ can be determined by a simple conventional banded matrix solver. It is evident that matrices $[\mathrm{M}]^{-1}$, [N], and $\left[\frac{\partial \mathbf{R}}{\partial \mathbf{X}}\right]$ are invariant with respect to iteration index k, so they only need to be computed once. A single conventional under-relaxiation parameter has been used to assure the convergence of Eq. (5.28). For a typical design analysis of an airfoil, $\left\{\frac{\partial \mathbf{Q}^*}{\partial \mathbf{P}}\right\}$ provides far more information than needed [13]. In most cases, the sensitivity of aerodynamic forces on the surface, such as lift and drag coefficients, are sought. The drag and lift coefficients are given as

$$C_L = C_Y cos\alpha - C_X sin\alpha \qquad (5.29)$$

$$C_D = C_Y sin\alpha + C_X cos\alpha \qquad (5.30)$$

where α is the angle of attack. The quantities C_X and C_Y are the total force coefficients along x and y directions, respectively, and can be expressed as

$$C_X = \sum_{i=1}^{J} C_{p_i}(y_{i+1} - y_i) + C_{f_i}(x_{i+1} - x_i) \qquad (5.31)$$

$$C_Y = \sum_{i=1}^{J} C_{p_i}(x_{i+1} - x_i) + C_{f_i}(y_{i+1} - y_i) \qquad (5.32)$$

where C_{pi} and C_{f_i} are pressure and skin friction coefficients respectively defined as

$$C_{p_i} = \frac{P_i}{\frac{1}{2}\rho_\infty U_\infty^2} \qquad C_{f_i} = \frac{\tau_i}{\frac{1}{2}\rho_\infty U_\infty^2} \qquad (5.33)$$

and J represents total number of boundary cells along the airfoil surface. The terms P_i and τ_i are pressure and shear stress associated with boundary cell i and the quantity $\frac{1}{2}\rho_\infty U_\infty^2$is known as dynamic pressure of the free stream. Finally, the drag and lift

sensitivity coefficients with respect to $\mathbf{X}_D$ are obtained by differentiating Eqs.(5.21) and (5.22) as

$$\frac{\partial C_L}{\partial \mathbf{X}_D} = \frac{\partial C_Y}{\partial \mathbf{X}_D} cos\alpha - \frac{\partial C_X}{\partial \mathbf{X}_D} sin\alpha \tag{5.34}$$

$$\frac{\partial C_D}{\partial \mathbf{X}_D} = \frac{\partial C_Y}{\partial \mathbf{X}_D} sin\alpha - \frac{\partial C_X}{\partial \mathbf{X}_D} cos\alpha. \tag{5.35}$$

5.6 Optimization Problem

An objective of a multidisciplinary optimization of a vehicle design is to extremize a payoff function combining dependent parameters from several disciplines. Most optimization techniques require the sensitivity of the payoff function with respect to free parameters of the system. For a fixed grid and solution conditions, the only free parameters are the surface design parameters. Therefore, the sensitivity of the payoff function with respect to design parameters are needed.

The optimization problem is based on the method of *feasible directions* [55,56] and the generalized reduced gradient method. This method has the advantage of progressing rapidly to a near-optimum design with only gradient information of the objective and constrained functions required. The problem can be defined as finding the vector of design parameters $\mathbf{X}_D$, which will minimize the objective function $f(\mathbf{X}_D)$ subjected to constraints

$$g_j(\mathbf{X}_D) \leq 0 \qquad j = 1, m \tag{5.36}$$

and

$$\mathbf{X}_D^l \leq \mathbf{X}_D \leq \mathbf{X}_D^u \tag{5.37}$$

where superscripts denote the upper and lower bounds for each design parameter. The optimization process proceeds iteratively as

$$\mathbf{X}_D^n = \mathbf{X}_D^{n-1} + \gamma \bar{\mathbf{S}}^n \tag{5.38}$$

where n is the iteration number, $\bar{\mathbf{S}}^n$ the vector of search direction, and γ a scalar move parameter. The first step is to determine a feasible search direction $\bar{\mathbf{S}}^n$, and then perform a one-dimensional search in this direction to reduce the objective function as much as possible, subjected to the constraints.

The present optimization strategy is based on maximizing the lift coefficient, C_L, in response to surface perturbation, subject to pre-determined design constraints. Upper and lower bounds set for each design parameter and the sensitivity derivatives of the objective function, $\frac{\partial C_L}{\partial \mathbf{X}_D}$, and the constraint, $\frac{\partial C_D}{\partial \mathbf{X}_D}$, are obtained as previously described. Throughout the analysis, the drag coefficient, C_D, is to be no greater than the value of the initial design. The strategy, illustrated in Fig. 5.1, requires that the grid and grid sensitivity derivatives be provided dynamically during the automated optimization process.

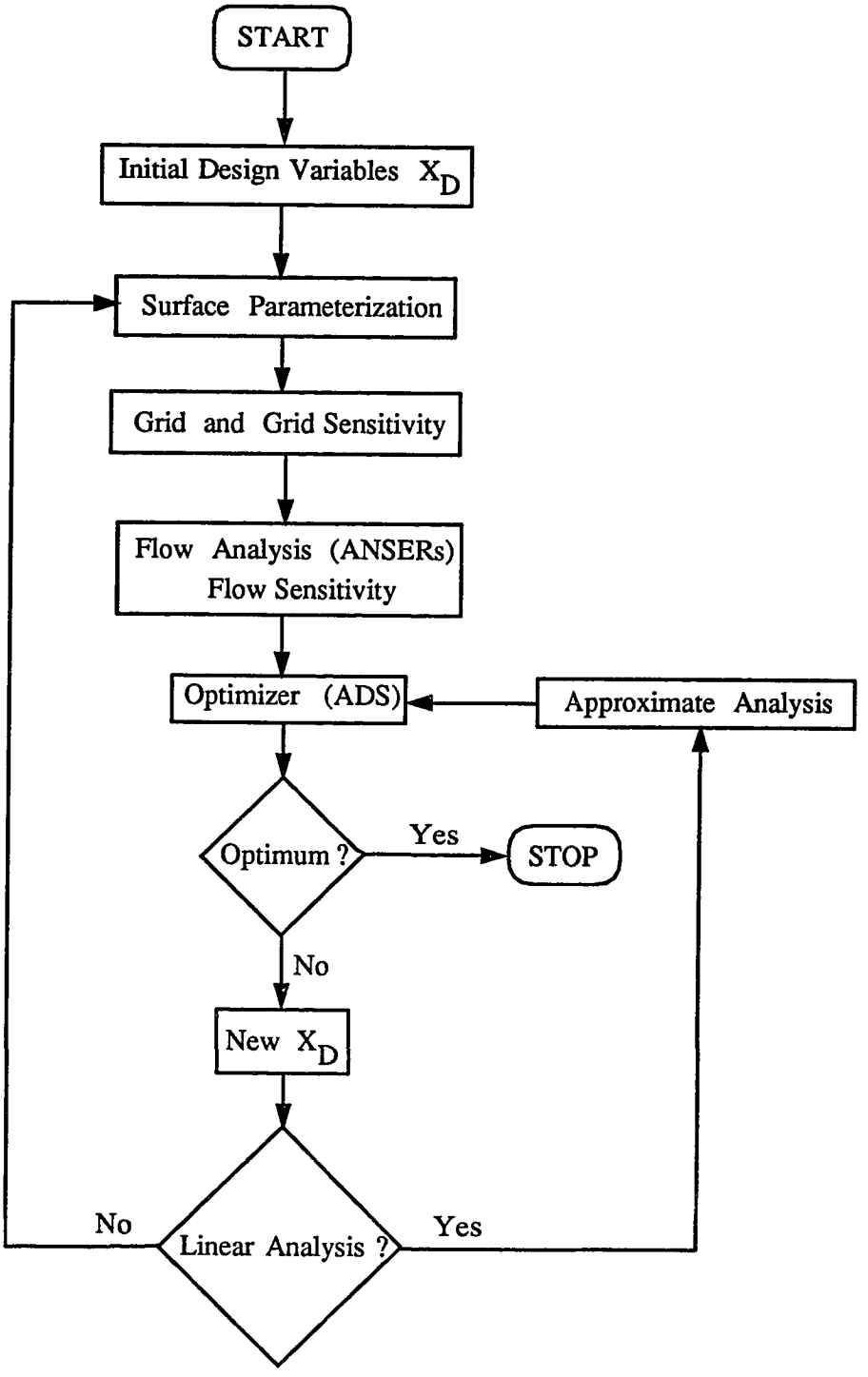

Fig. 5.1 Design optimization strategy loop.

Chapter 6

RESULTS AND DISCUSSION

Three test cases are considered to demonstrate the feasibility of current procedure. For each case, the grid and flow sensitivity coefficients of the field have been obtained. The sensitivities of the total surface forces (i.e., Lift and Drag coefficients) are tabulated for optimization purposes. The first test case, a symmetrical NACA 0012 wing-section, has been used mainly to exhibit the accuracy of the grid sensitivity coefficients with those obtained using the finite difference approach before proceeding to more challenging problems. The second test case, a NACA 8512 wing-section, has been used to extend the analysis to a more demanding problem involving three design parameters. An optimization module has been integrated into the overall procedure to optimize the geometry using the resultant sensitivity coefficients. Also for this case, some aspects of grid sensitivity with respect to grid parameters are investigated for grid optimization problem. The last case involves a generic representation of a wing-section using NURBS for surface definition. The improved design has been obtained employing sensitivity coefficients of the domain with respect to previously chosen design control points. Due to flexibility of NURBS in representing any surface, the generic wing-section test case has been used to manifest the extension of this approach to almost any desired geometry.

6.1 Case 1: NACA 0012 Wing-Section

6.1.1 Grid Sensitivity

The previously obtained grid, as shown in Fig.3.9, is considered for grid sensitivity analysis of this test case. The grid sensitivity with respect to the vector of design parameters $\mathbf{X}_D$, are obtained using Eqs.(5.1) and (5.2) where the maximum thickness T is the only design parameter.

Figure 6.1a shows the contour levels of the y-coordinate sensitivity with respect to the thickness parameter, T. The highest contour levels are, understandably, located in the vicinity of the chordwise location for the maximum thickness of the wing section. For a NACA four-digit wing section, this is positioned at about 0.3 of the chord length from the leading edge [25]. The positive and negative contour levels corresponding to the upper and lower surfaces are the direct consequence of Eq.(2.4) and the second term on the right hand side of Eq.(5.8). The sensitivity levels decrease when approaching the far-field boundary due to diminishing effects of the interpolation function $\beta_1^0(t, \mathbf{P}_0^\eta)$. The second term on the right hand side of Eq.(5.8) is responsible for the sensitivity effects due to orthogonality on the surface, and it is directly proportional to the magnitude of the orthogonality vector K_1. The wake region is not sufficiently affected by any of the design parameters, and no major sensitivity gradient should be expected there.

Figure 6.1b exhibits the contour levels of the x-coordinate sensitivity with respect to thickness parameter, T. An interesting observation can be made here regarding the contour levels adjacent to the surface. Unlike the y-coordinate sensitivity, the x-coordinate sensitivity is independent of design parameters at surface as indicated by Eq.(5.4). The contour levels resulting from Eq.(5.7) are solely due to or-

thogonality effects. There are some negative pockets of contour levels on the forward section and some corresponding positive pockets on the rear section. The dividing line between these pockets is located near the location of the maximum thickness (i.e., 0.3 of the chord from the leading edge). A simple conclusion from Fig. 6.1b is that by increasing the thickness parameter, T, points on the forward section will move to the left, while at the same time, points at rear section will move to the right.

For comparative purposes, the grid sensitivity for this case is obtained using the finite difference approach. The design parameters(i.e. T for this case) are perturbed, one at a time, and a new grid is obtained using Eqs. (3.9) and (3.10). The sensitivity is then computed using a central difference approximation and the results are presented in Fig. 6.2 . A side by side comparison of both results indicates good agreement between the two approaches.

6.1.2 Flow Sensitivity

The second phase of the problem is obtaining the flow sensitivity coefficients using the previously obtained grid sensitivity coefficients. In order to achieve this, according to Eq.(4.17), a converged flow field solution about a fixed design point should be obtained. The computation is performed on a C-type grid composed of 141 points in the streamwise direction with 101 points on the wing-section surface, and 31 points in the normal direction. The far-field and outer boundary were placed about 20 chord-length away from the airfoil. It is apparent that such a coarse grid is inadequate for capturing the full physics of the viscous flow over an airfoil. Therefore, it should be understood that the main objective here is not to produce a highly accurate flow field solution rather than to demonstrate the feasibility of the approach.

The two-dimensional, compressible, thin-layer Navier-Stokes equations are solved for a free stream Mach number of $M_\infty = 0.8$, Reynolds number $Re_\infty = 10^6$, and angle of attack $\alpha = 0°$. The solution is implicitly advanced in time using local

time stepping as a means of promoting convergence toward the steady-state. The residual is reduced by ten orders of magnitude as illustrated in Fig. 6.3. All computations are performed on NASA Langley's Cray-2 mainframe with a computation cost of $0.1209\text{x}10^{-3}$ CPU seconds/iteration/grid point. Figures 6.4 and 6.5 demonstrate the pressure and Mach number contours of the converged solution with lift and drag coefficients of $C_L = 1.53\text{x}10^{-8}$ and $C_D = 4.82\text{x}10^{-2}$. Due to surface curvature, the flow accelerates along the the upper and lower surfaces to supersonic speeds, terminated by a weak shock wave behind which it becomes subsonic.

The sensitivity coefficient, $\left\{\frac{\partial \mathbf{Q}^*}{\partial T}\right\}$, is obtained by previously described iterative strategy of Eq.(5.28). The average error has been reduced by three orders of magnitude and the convergence history is shown in Fig. 6.6. The sensitivities of the aerodynamic forces, such as drag and lift coefficients with respect to thickness parameter T, are obtained utilizing Eqs.(5.29-5.35) with results presented in Table 6.1. Again, for comparison , a finite difference approximation has been implemented to validate the results. A nominal perturbation of 10^{-4} for design parameter T has been chosen and the corresponding results are included in Table 6.1. The good agreement between the two sets of numbers verifies the accuracy of the approach. It is apparent from Table 6.1 that while drag is extremely sensitive to the changes in wing-section thickness, the lift is almost insensitive, due to symmetrical nature of flow for this case.

Table 6.1 Lift and Drag sensitivities with respect to design parameter T

NACA 0012	Direct Approach		Finite Difference	
Design Parameters	$\frac{\partial C_L}{\partial X_D}$	$\frac{\partial C_D}{\partial X_D}$	$\frac{\partial C_L}{\partial X_D}$	$\frac{\partial C_D}{\partial X_D}$
Maximum Thickness	$-2.68\text{x}10^{-6}$	0.709	$-4.75\text{x}10^{-6}$	0.707

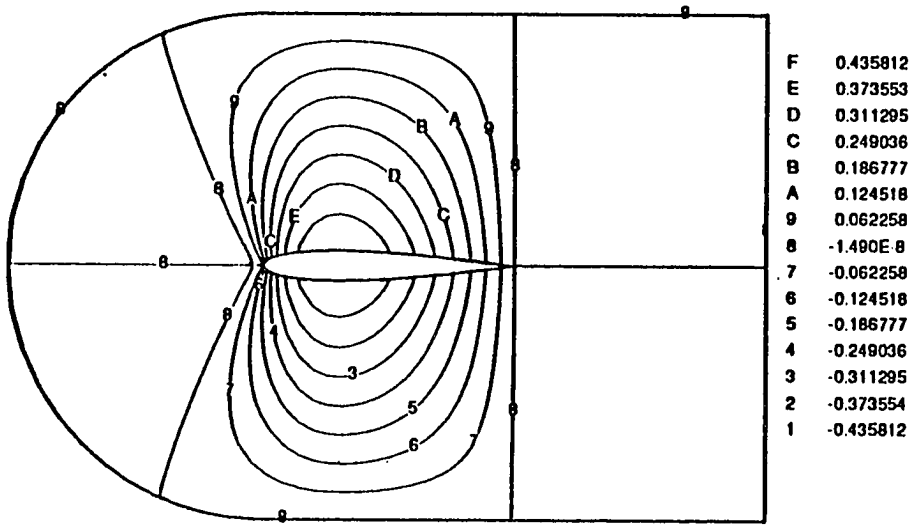

(a) Y-Coordinate

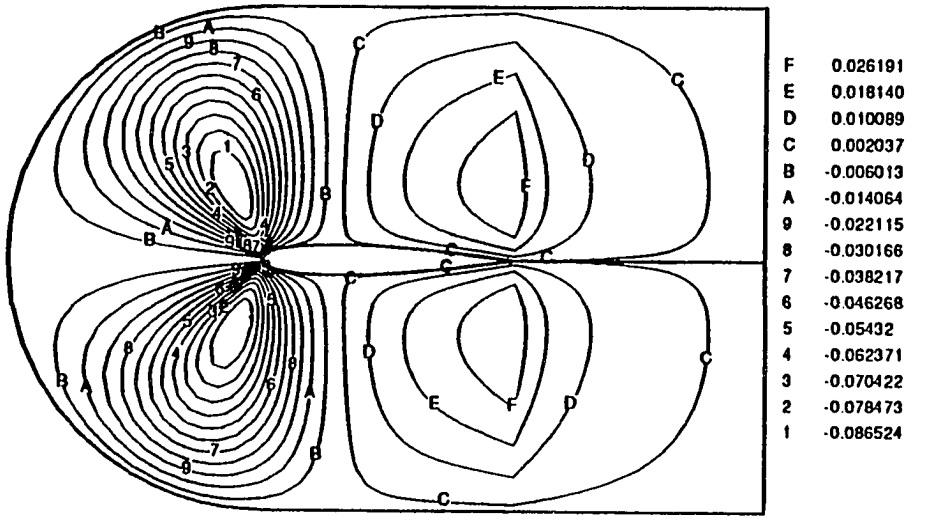

(b) X-Coordinate

Fig. 6.1 Coordinate sensitivity with respect to maximum thickness T (DD).

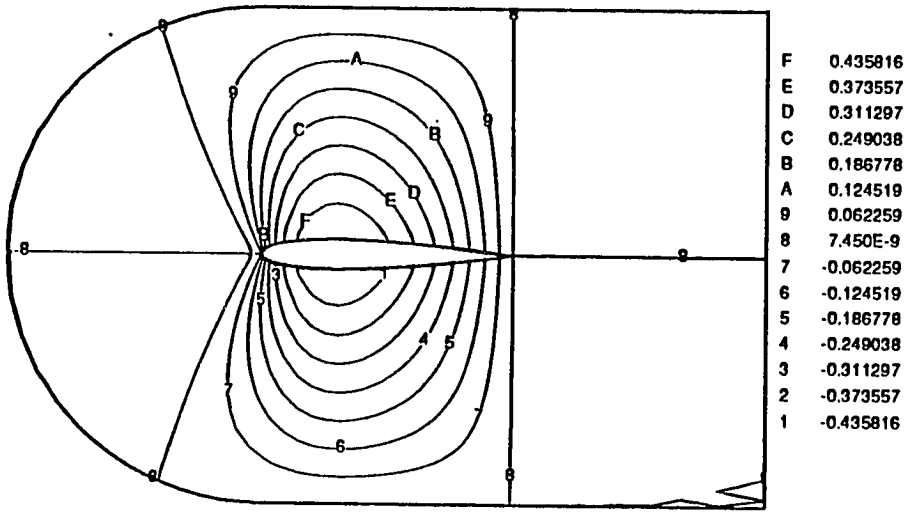

(a) Y-Coordinate

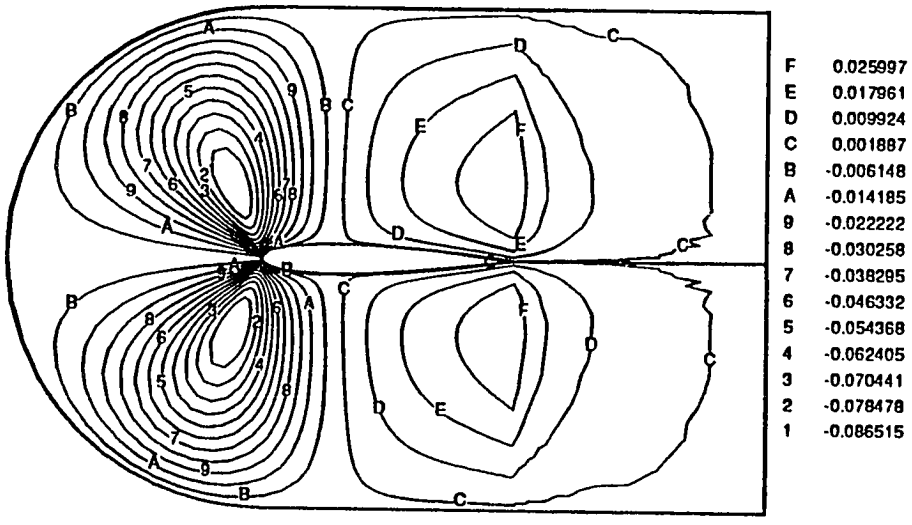

(b) X-Coordinate

Fig. 6.2 Coordinate sensitivity with respect to maximum thickness T (FD).

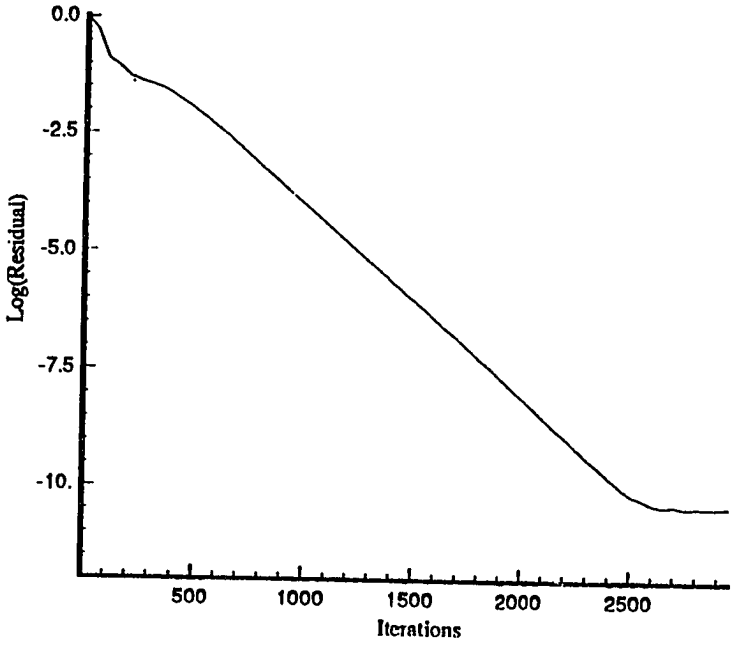

Fig. 6.3 Residual convergence history.

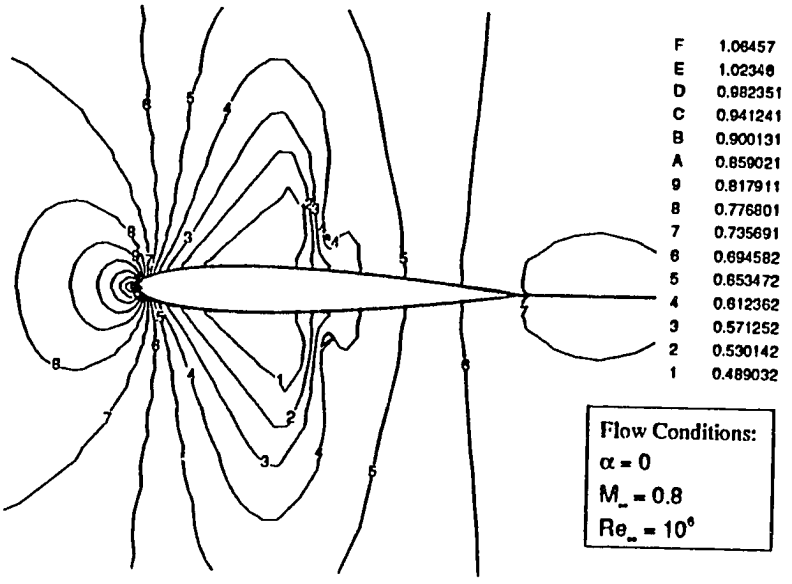

Fig. 6.4 Pressure contours for NACA 0012 wing-section.

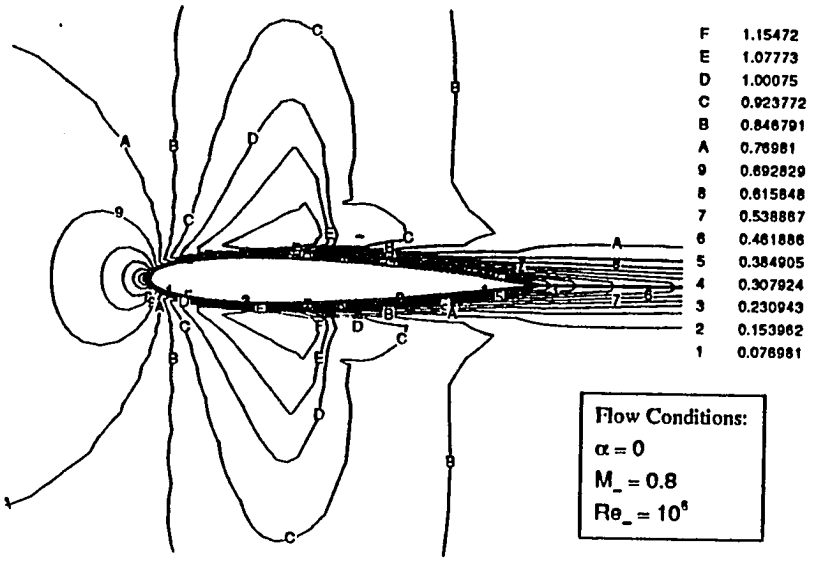

Fig. 6.5 Mach number contours for NACA 0012 wing-section.

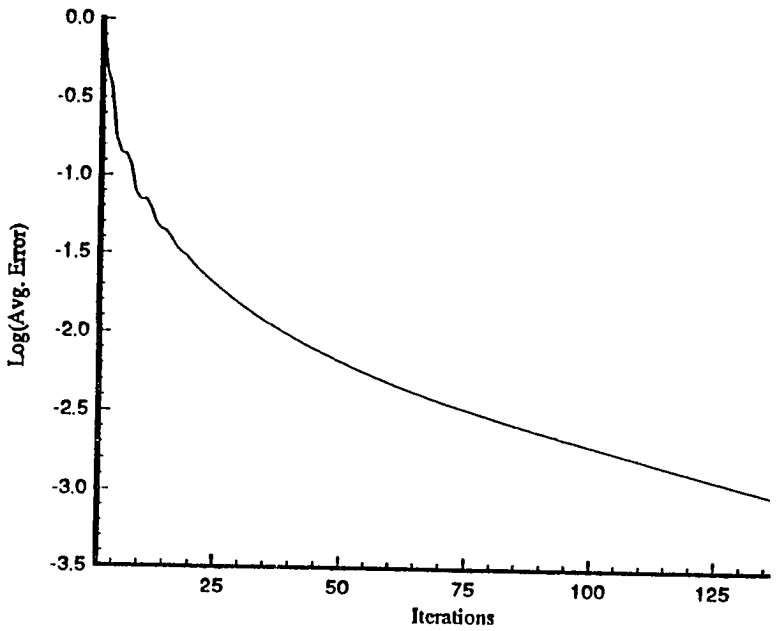

Fig. 6.6 Sensitivity equation convergence history.

6.2 Case 2: NACA 8512 Wing-Section

6.2.1 Grid Sensitivity

The second test case considered is the NACA 8512 cambered airfoil. Again, the previously obtained grid, as shown in Fig. 3.10, is considered for grid sensitivity analysis. Figure 6.7 shows the coordinate sensitivity with respect to parameter T with characteristics similar to the previous symmetrical airfoil case. Figure 6.8a represents the y-coordinate sensitivity with respect to camber, M. It appears that the highest sensitivity contour levels are located at the chordwise location of camber, C (i.e., 0.5 of the chord-length). The contour levels decrease toward the far-field boundary, again as a consequence of interpolation function. However, unlike Fig. 6.7a, they possess positive values on both upper and lower surfaces. Consequently, an increase in camber, M, shifts all the points upward. Again, minimum activity can be detected in the wake region. Figure 6.8b shows the x-coordinate sensitivity contours with respect to camber, M. Here, as in Fig. 6.7b, the sensitivities are minimum on the surface of the wing-section. There is a small gradient on the forward section, but by far the strongest gradient is in the rearward section due to orthogonality effects.

Figure 6.9a illustrates the y-coordinate sensitivity with respect to camber location, C. A dividing line between positive and negative contour levels appears near the chordwise position of the camber. Like previous cases, there is no significant activity in the wake region. The result indicates that a positive change of C will cause the movement of points downward on the forward section, while at the same time, the points on the rear section will respond by moving upward. Figure 6.9b illustrates the x-coordinate sensitivity with respect to camber location C. The two major features are attributed to chordwise location of the camber and the orthogonality effects on

the tail section. It is interesting to notice that the sensitivity level for camber location is considerably less than the other two design parameters.

Another important aspect of grid sensitivity analysis is to investigate the sensitivity of a grid with respect to grid parameters. Such information would be most helpful in grid optimization, therefore, improving the flow solution and overall optimization process. Figure 6.10 illustrates the grid sensitivity with respect to stretching parameter, B_3, where the hyperbolic behavior of contour levels are apparent. The sensitivity of grid with respect to grid distribution parameter around an airfoil, B_1, is shown in Fig. 6.11. The y-coordinate sensitivity does not register any large gradient field except on the front. The x-coordinate, being the distribution axes, do however show some interesting contour levels on the surface. The sensitivities with respect to orthogonality parameter at the surface, K_1, are presented on Fig. 6.12. Figure 6.13 exhibits the grid sensitivity of the domain with respect to the outer boundary location, L. The effect of outer boundary location on the solution is a subject of extensive research and deserves a more comprehensive investigation [33].

6.2.2 Flow Sensitivity and Optimization

Using free stream conditions of $M_\infty = 0.7$, $Re_\infty = 10^6$, and $\alpha = 0°$, a converged flow field solution is obtained. As in the previous case, a C-type grid of 141x31 is used and the far-field boundary is placed about twenty chord-length away from the surface. The residual is reduced by ten orders of magnitude using 3000 implicit Euler time iterations. Figures 6.14 and 6.15 illustrate the resulting pressure and Mach number contours. As a consequence of camber, flow accelerates along the upper surface to supersonic speeds. As the flow travels further, it encounters an adverse pressure gradient due to decreasing curvature, resulting in a weak shock and subsonic flow. Figure 6.16 shows the surface pressure coefficient C_p, where lift and drag coefficients are $C_L = 0.611$, and $C_D = 0.094$.

The surface aerodynamic sensitivity coefficients with respect to the vector of design parameters $\mathbf{X}_D$, are obtained and presented in Table 6.2. Figure 6.17 demonstrates the convergence behavior of Eq. (5.28) for $\mathbf{P} = \{T, M, C\}^T$. It is apparent that a combination of increasing camber and decreasing thickness would greatly improve the Lift/Drag ratio for this particular problem. The effects of camber location C is almost negligible and might be ignored in optimization process in order to decrease the computational costs. A comparison with finite difference approximation s reveals the accuracy of the this direct approach. It is imperative to understand that due to the non-linear nature of Navier-Stokes equations, the results of Table 6.2 is only valid for current specified wing-section and flow condition. Extrapolating from these coefficients to predict flow solutions for different families of wing-sections would be greatly erroneous and unreliable. Such predictions are only valid as long as the design perturbations are in the same order as the finite-difference step size used in Table 6.2.

Table 6.3 displays similar results for the vector of grid parameters, $\mathbf{X}_G$. The far-field boundary location L has the greatest effect on lift and drag, followed by surface grid orthogonality parameter, K_1. An underlying effort in generating a suitable grid for flow analysis is to minimize the gridding effects on the solution. Inspecting Table 6.3 reveals that the solution is apparently grid sensitive; therefore, not particularly suitable for this geometry. This grid dependency of solution may be mainly blamed on the coarseness of the grid and the location of far-field boundary. Infact, according to Table 6.3, the far-field boundary should be placed further away from wing-section in order to achieve better Lift/Drag ratio. This, will undoubtedly contribute to the coarseness of the grid, and ultimately to solution instability. Increasing the grid density, although may alleviate the problem, but will cause a surge in computational costs. Another improvement may be to modify the orthogonality vector in response to high slope regions of the surface. Also, a modest increase in

stretching parameter might produce better results as indicated in Table 6.3. The grid distribution on the surface appears to be sufficient due to small value of its sensitivity coefficients. An ideal situation would be to alter the grid parameters until the sensitivity coefficients of Table 6.3 all approach to zero. A combination of the above recommendations although might produce such grid, but would be tedious and time consuming. An alternative is to optimize each of these grid parameters using similar optimization techniques as devised for design parameters. In this respect, an optimum grid can be constructed for this particular example which also can be used in design optimization cycles. Since the main objective here is to demonstrate the validity of grid sensitivity module and its integration into the optimization loop, these deficiencies will be overlooked for the present time.

The design optimization strategy of Fig. 5.1 is applied to three design parameters of T, M, and C. The intention is to maximize the Lift/Drag ratio subjected to appropriate boundary perturbation. The upper and lower bounds for design parameters are assigned as

$$0.08 \leq T \leq 0.16, \quad 0.04 \leq M \leq 0.12, \quad 0.3 \leq C \leq 0.7. \tag{6.1}$$

The computation is performed dynamically using the design optimization module of ADS (Automated Design Synthesis) as outlined in [56]. The optimum design is achieved after 11 non-linear optimization cycles and a total of 6800 CPU seconds on Cray-2 mainframe. A simple break down of computational costs indicates that about 80% of this processing time is spent on flow analyses , as is the case for most flow solvers. Table 6.4 shows the improvement in Lift/Drag ratio for this particular wing-section. The corresponding design parameters and their optimum values are included in Table 6.5. As expected from sensitivity coefficients, maximum thickness T, and maximum camber M, had the greatest effect on this optimization process. Figure 6.18 illustrates the comparison between initial and optimized wing-section.

Table 6.2 Lift and Drag sensitivities with respect to vector design parameter $\mathbf{X}_D$

NACA 8512	Direct Approach		Finite Difference	
Design Parameters	$\frac{\partial C_L}{\partial X_D}$	$\frac{\partial C_D}{\partial X_D}$	$\frac{\partial C_L}{\partial X_D}$	$\frac{\partial C_D}{\partial X_D}$
Maximum Thickness T	-4.23	0.442	-4.23	0.442
Maximum Camber M	+7.84	0.322	+7.83	0.322
Maximum Camber location C	$-8.34\text{x}10^{-3}$	$-4.3\text{x}10^{-3}$	$-8.5\text{x}10^{-3}$	$-4.1\text{x}10^{-3}$

Table 6.3 Lift and Drag sensitivities with respect to vector of grid parameters $\mathbf{X}_G$

NACA 8512	Direct Approach		Finite Difference	
Grid Parameters	$\frac{\partial C_L}{\partial X_G}$	$\frac{\partial C_D}{\partial X_G}$	$\frac{\partial C_L}{\partial X_G}$	$\frac{\partial C_D}{\partial X_G}$
Grid Stretching	$1.1\text{x}10^{-2}$	$1.5\text{x}10^{-3}$	$1.08\text{x}10^{-2}$	$1.5\text{x}10^{-3}$
Grid Distribution	$-2.2\text{x}10^{-3}$	$-8.6\text{x}10^{-4}$	$-2.2\text{x}10^{-3}$	$-8.58\text{x}10^{-4}$
Surface Orthogonality	$+3.2\text{x}10^{-2}$	$8.13\text{x}10^{-3}$	$+3.2\text{x}10^{-2}$	$8.15\text{x}10^{-3}$
Far-field Boundary Location	$1.7\text{x}10^{-1}$	$5.43\text{x}10^{-3}$	$1.7\text{x}10^{-1}$	$5.45\text{x}10^{-3}$

Table 6.4 Comparison of initial and optimized performance variables

Performance Variables	Initial Design	Optimum Design	Percent Change
C_L	0.611	0.746	+22
C_D	0.094	0.089	−5.3
Lift/Drag Ratio	6.5	8.38	+28.9

Table 6.5 Comparison of initial and optimized design parameters

Design Parameters	Initial Design	Optimum Design	Percent Change
Max. Thickness T	0.12	0.08	−33.33
Max. Camber M	0.08	0.098	+22.5
Location of Camber C	0.5	0.55	+10

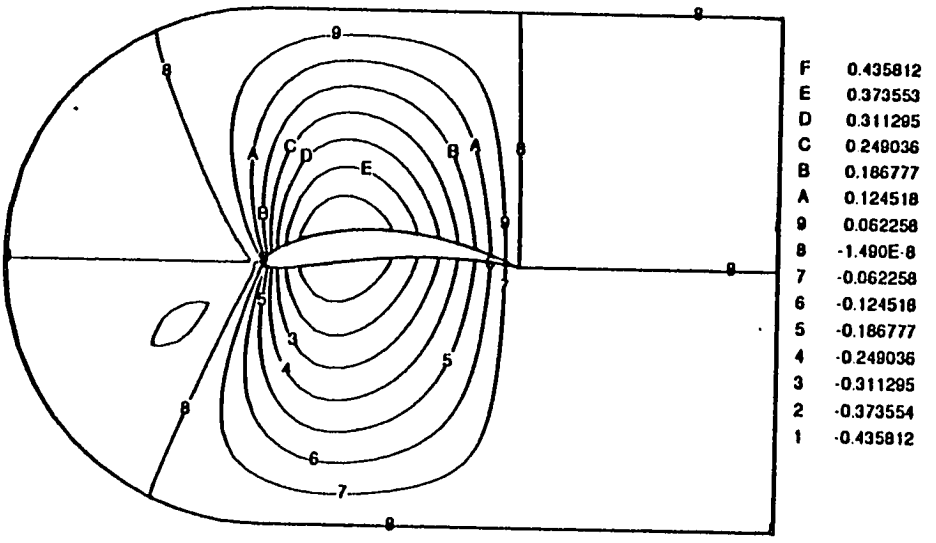

(a) Y-Coordinate

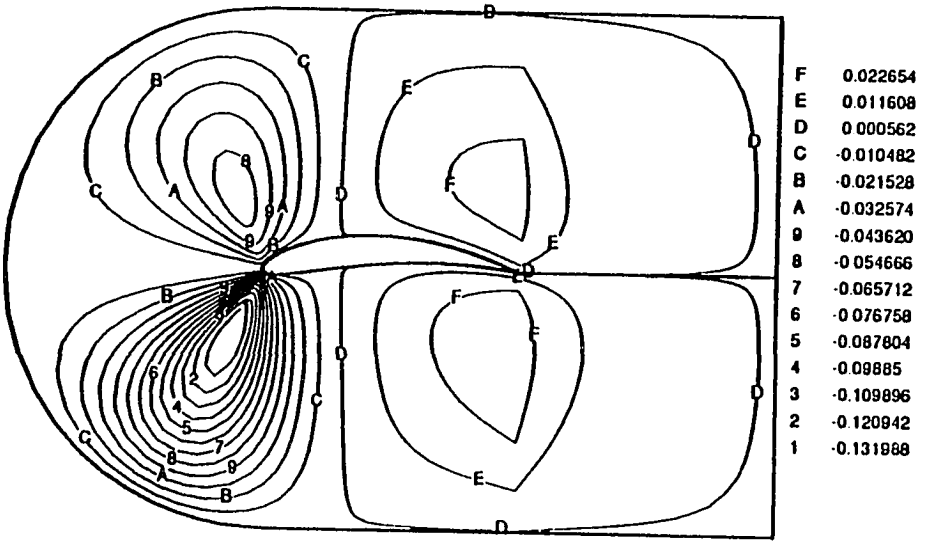

(b) X-Coordinate

Fig. 6.7 Coordinate sensitivity with respect to maximum thickness T.

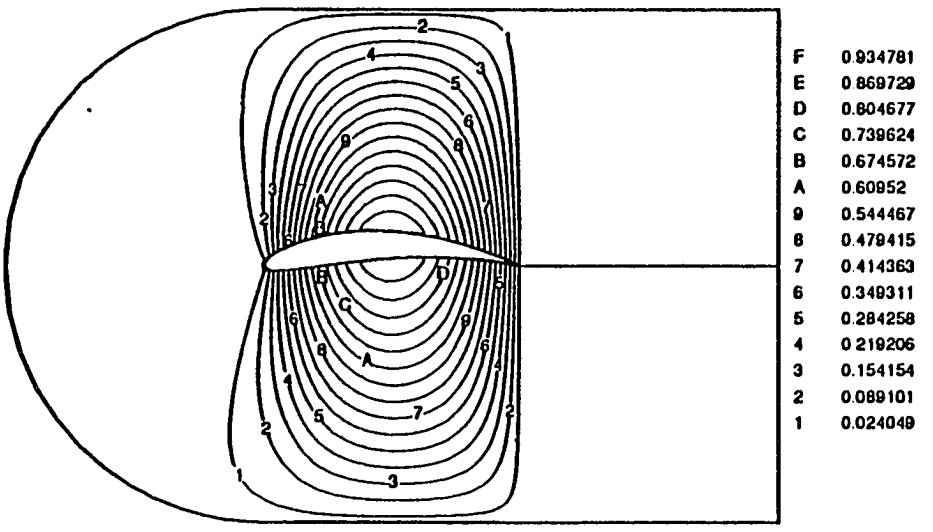

(a) Y-Coordinate

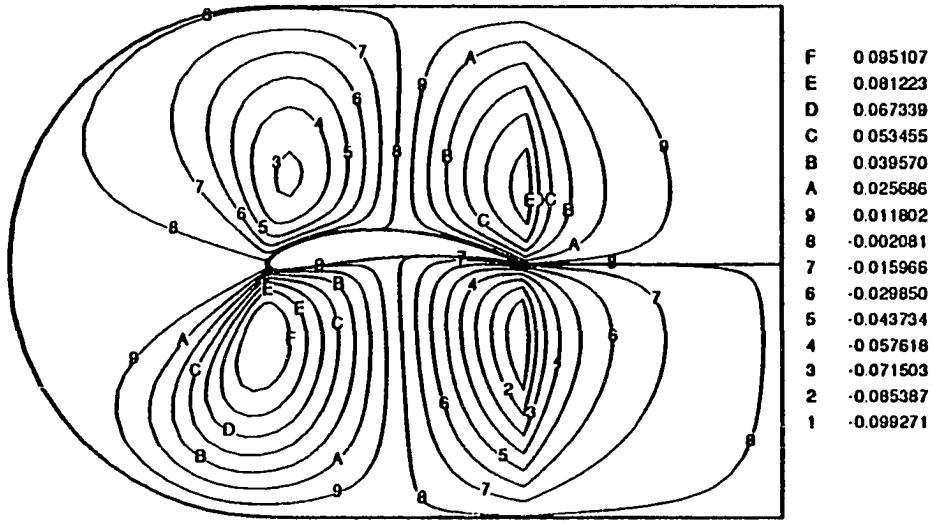

(b) X-Coordinate

Fig. 6.8 Coordinate sensitivity with respect to maximum camber M.

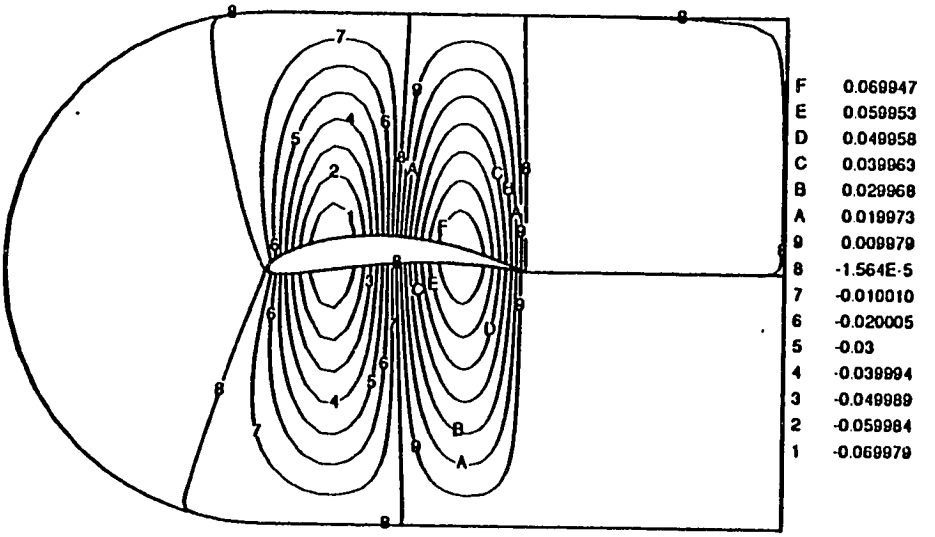

(a) Y-Coordinate

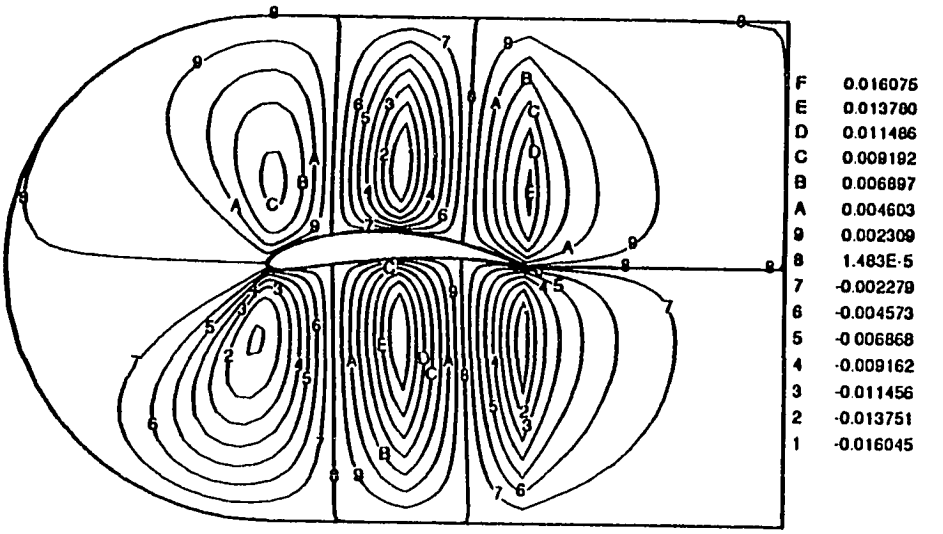

(b) X-Coordinate

Fig. 6.9 Coordinate sensitivity with respect to location of maximum camber C.

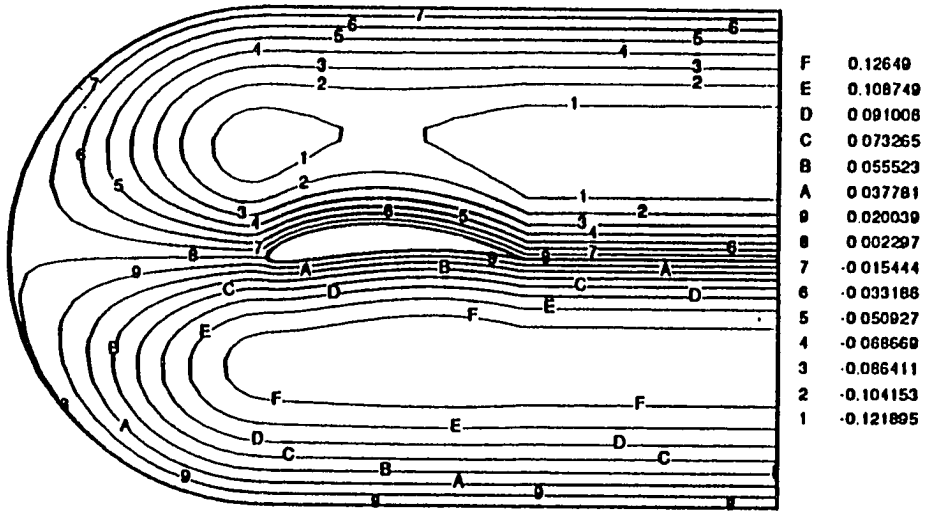

(a) Y-Coordinate

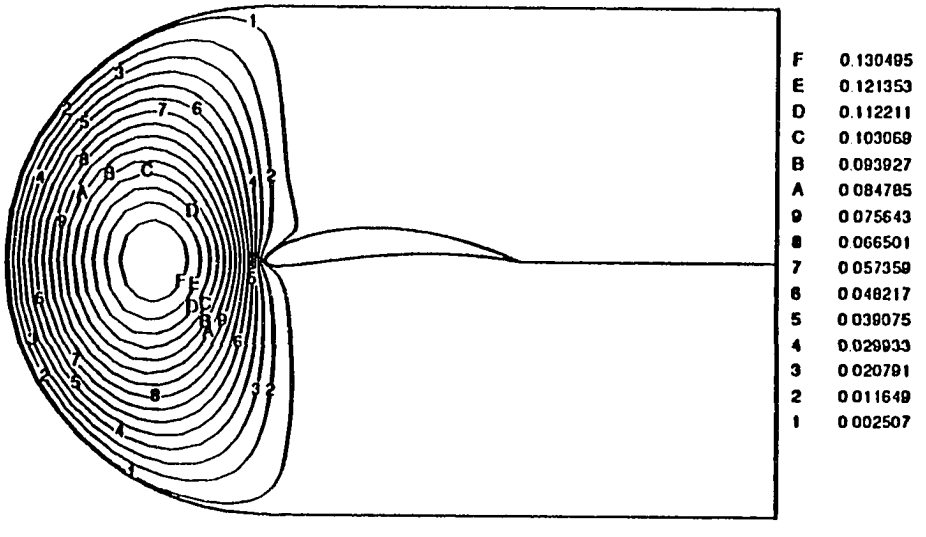

(b) X-Coordinate

Fig. 6.10 Coordinate sensitivity with respect to grid stretching parameter B_3.

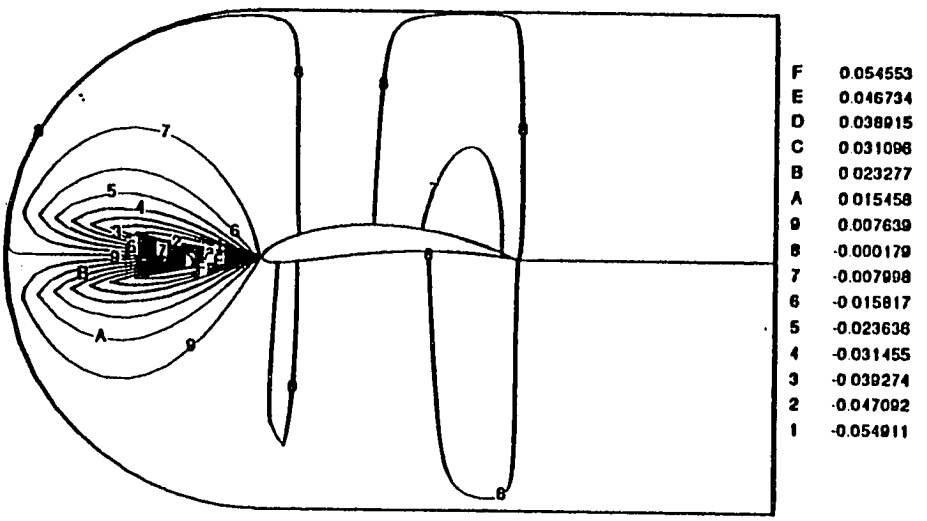

(a) Y-Coordinate

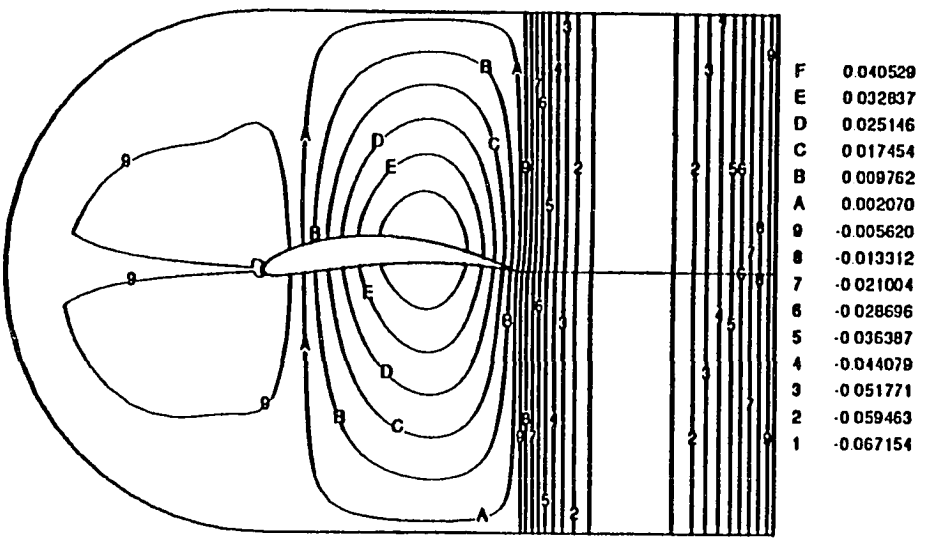

(b) X-Coordinate

Fig. 6.11 Coordinate sensitivity with respect to grid distribution parameter B_1.

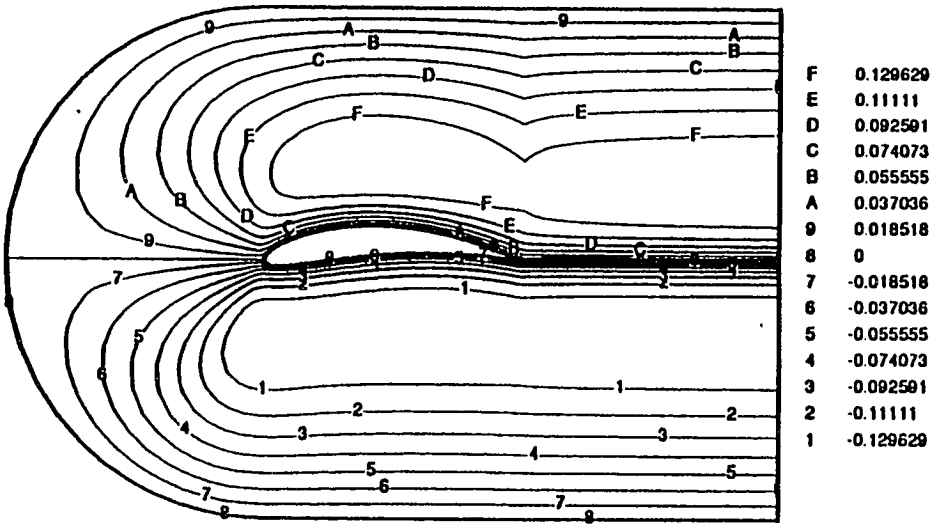

(a) Y-Coordinate

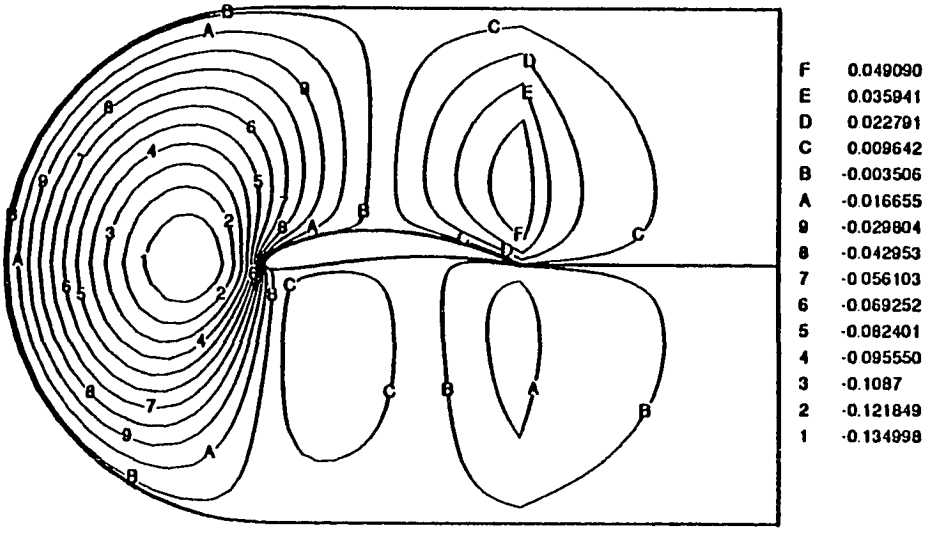

(b) X-Coordinate

Fig. 6.12 Coordinate sensitivity with respect to grid orthogonality. parameter K_1.

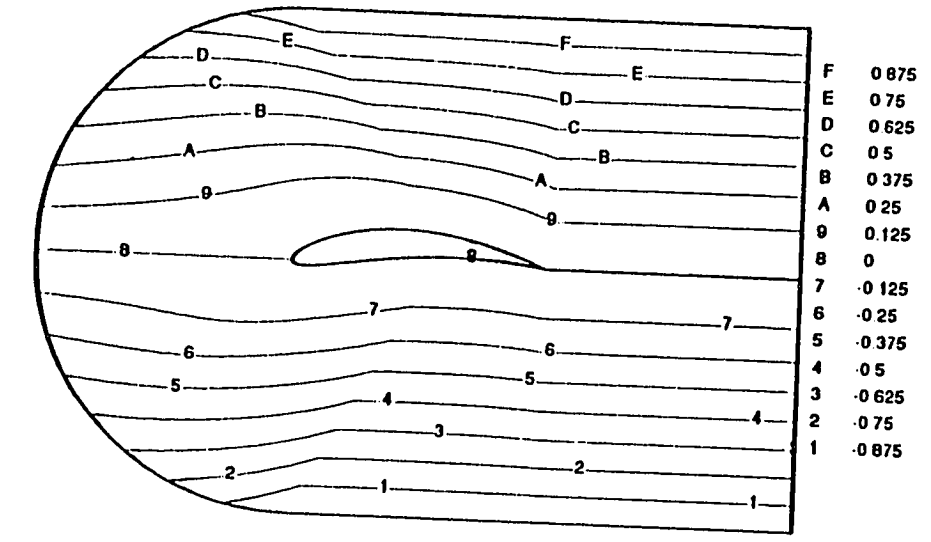

Y-coordinate

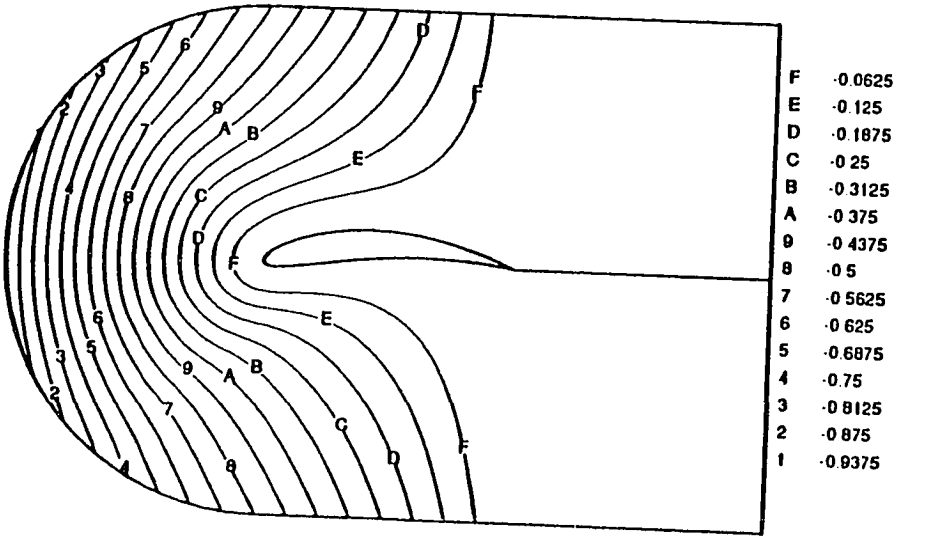

X-coordinate

Fig. 6.13 Coordinate sensitivity with respect to outer boundary location L.

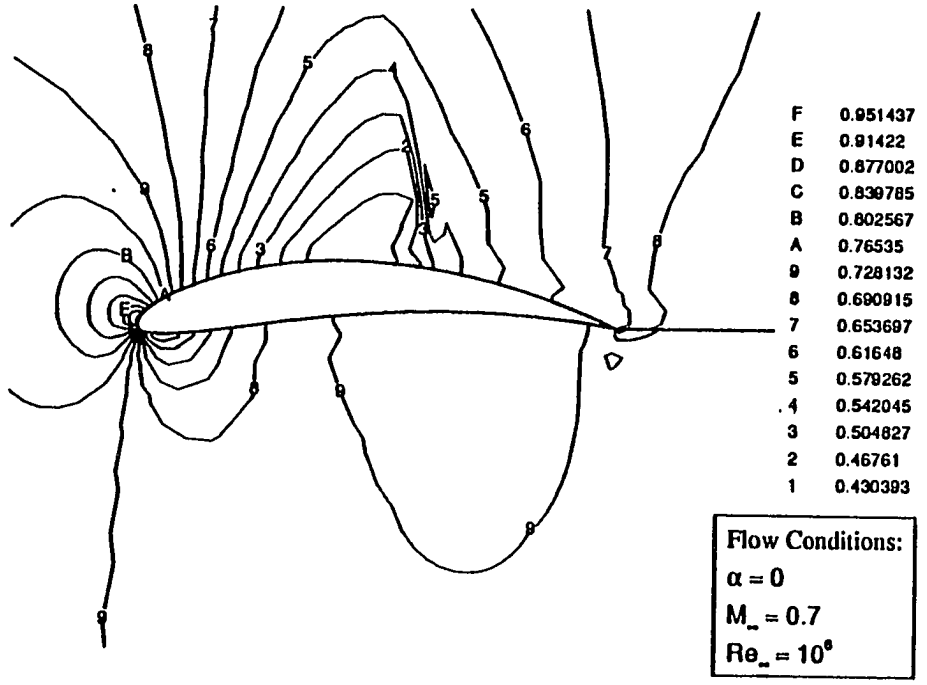

Fig. 6.14 Pressure contours for NACA 8512 wing-section.

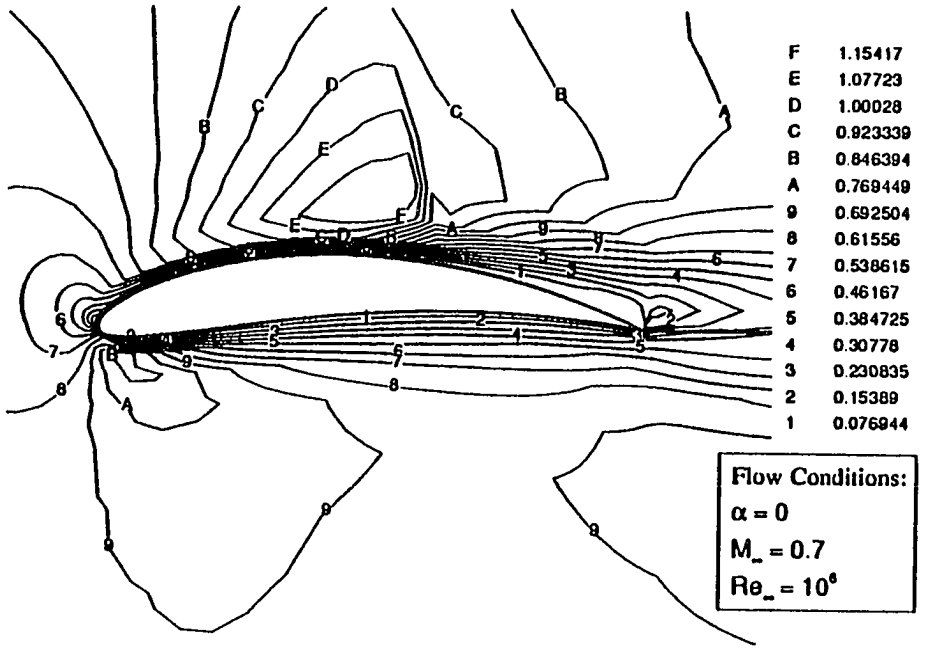

Fig. 6.15 Mach number contours for NACA 8512 wing-section.

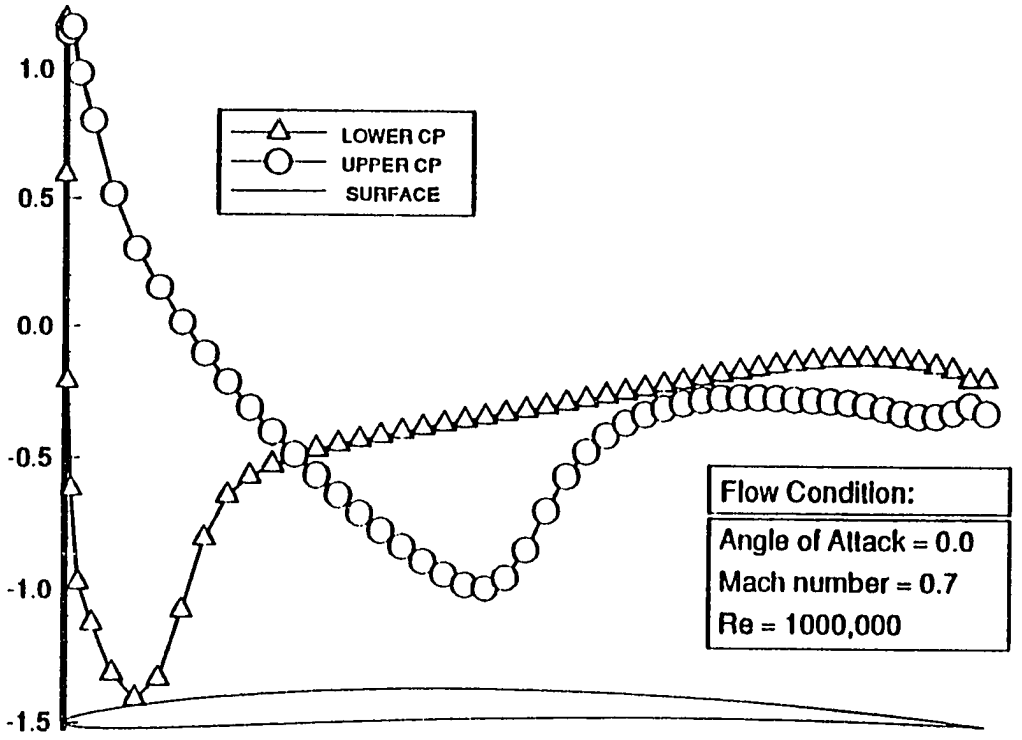

Fig. 6.16 Surface pressure coefficient for NACA 8512 wing-section.

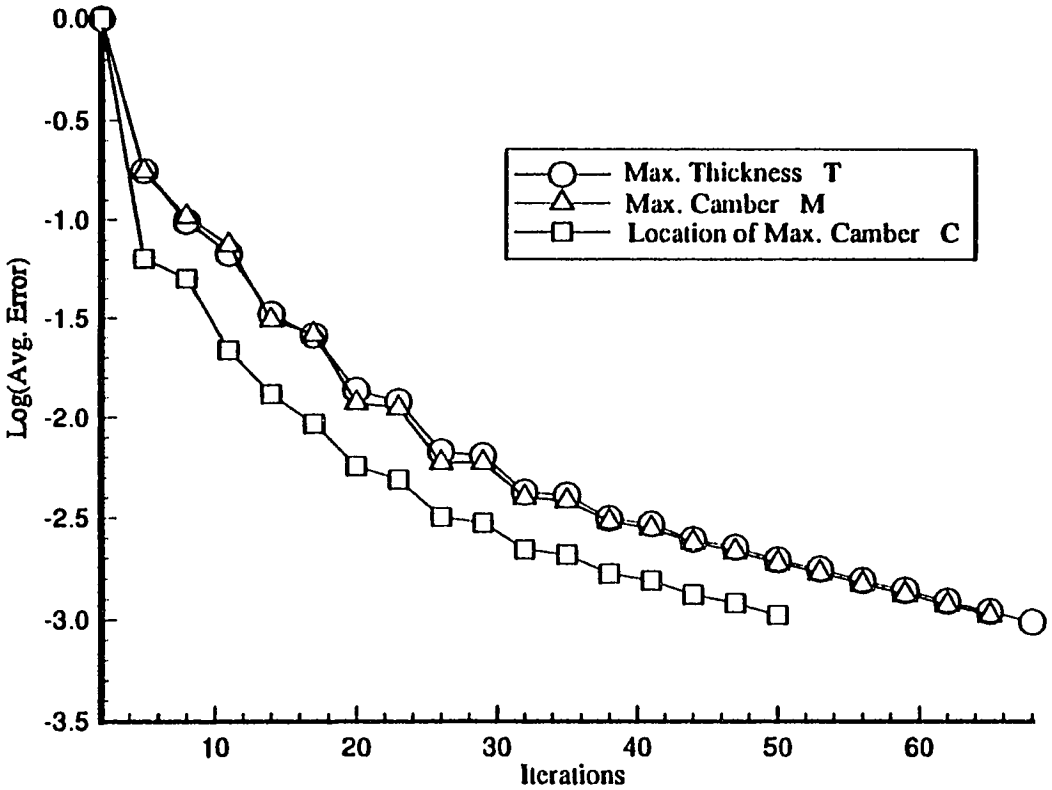

Fig. 6.17 Sensitivity equation convergence history.

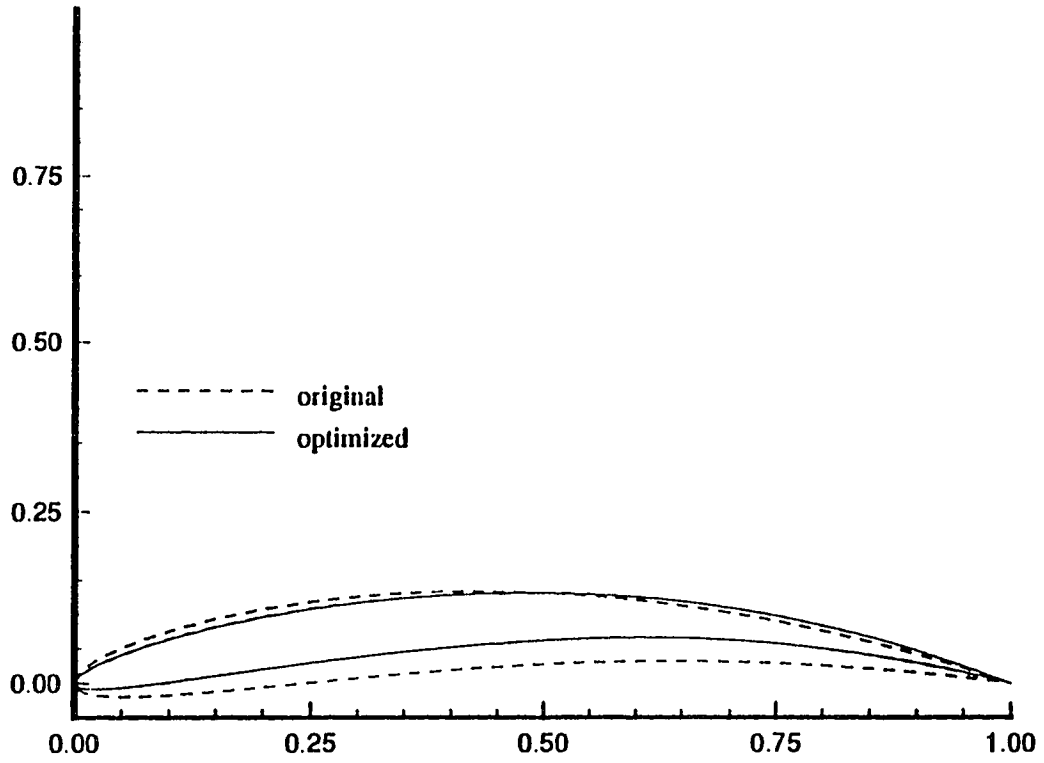

Fig. 6.18 Original and optimized wing-section.

6.3 Case 3: Generic Wing-Section

6.3.1 Grid Sensitivity

The grid sensitivity with respect to design parameters using the NURBS parameterization is discussed in this section. A generic wing-section is devised by employing Eq.(2.9) and seven pre-specified control points and weights (option 3). Figure 6.19 represents the wing-section and the control polygon using cubic basis functions of Fig. 2.9. The control points are numbered counter-clockwise, starting and ending with control points (0 and 6), assigned to the tail of the wing-section. As a consequence of Eq.(5.9), the total number of design parameters now jumps to 21 (i.e., three design parameters/control point). Depending on desired accuracy and degree of freedom for optimization, the number of design parameters could be reduced for each particular problem. For the present case, such reduction is achieved by considering fixed weights and chord-length. Out of the remaining four control points with two degrees of freedom for each, control points 1 and 5 would probably have the greatest impact due to their camber-like positions. The number of design parameters now reduced to four with $\mathbf{X}_D = \{X_1, Y_1, X_5, Y_5\}^T$ with initial values specified in Fig. 6.19. In accordance with Eq.(5.10), the non-zero contribution to the surface grid sensitivity coefficients of these control points, are the basis functions $R_{1,3}(r)$ and $R_{5,3}(r)$, shown in Fig. 6.20. Figure 6.21 illustrates the field-grid sensitivity with respect to design parameter Y_1. It is interesting to notice the similarities between contour patterns of Fig. 6.21a and 6.8a with one obvious difference. The sensitivity gradients are restricted only to the region influenced by the elected control point. This locality feature of the NURBS parameterization makes it a desirable tool for complex design and optimization when sometimes only a local perturbation of the geometry is warranted.

Figure 6.22 represents similar results for design control point 5 where the sensitivity gradients are restricted to the lower portion of domain.

6.3.2 Flow Sensitivity and Optimization

The previous free-stream conditions of case 2 has been used to advance the solution in time. The far-field boundary is again placed at 20 chord-length away with specified boundary conditions outlined in section 5.4. The previously defined C-type grid of 141x31 grid points is used and the residual is reduced by ten orders of magnitude. Flow characteristics similar to case 2 are detected with lift and drag coefficients of $C_L = 0.402$ and $C_D = 0.063$. The lift and drag sensitivities with respect to $\mathbf{X}_D$ are presented in Table 6.6. The finite -difference comparison of sensitivity coefficients has been avoided due to already verified sensitivity module. An inspection of Table 6.6 indicates the substantial influence of parameters Y_1 and Y_5 on the aerodynamic forces acting on the surface. The upper and lower bounds for these design parameters are assigned as

$$0.2 \leq X_1 \leq 0.7, \quad -0.1 \leq Y_1 \leq 0.5, \quad 0.2 \leq X_5 \leq 0.7, \quad -0.1 \leq Y_5 \leq 0.2. \quad (6.2)$$

The optimum design is achieved after 17 optimization cycles and total of 8807 Cray-2 CPU seconds. Comparing with case 2, an almost 30% CPU increase can be attributed to the addition of extra design parameter. These computational cost overruns make minimizing the number of design parameters in CFD optimization essential. Table 6.7 highlights the initial and final values of lift and drag coefficients with a 208% improvement in their ratio. Table 6.8 represents the initial and optimum design parameters with parameters Y_1 and Y_5 having the largest change as expected. The history of design parameters deformation during the optimization cycles appears in Fig. 6.23, where the oscillatory nature of design perturbations during the early cycles are clearly visible. Figure 6.24 compares the initial and optimum geometry of the wing-section.

Several observations should be made at this point. First, although control points 1 and 5 demonstrated to have substantial influence on the design of the wing-section, they are not the only control points affecting the design. Infact, control points 2 and 4 near the nose might have greater affect due to sensitive nature of lift and drag forces on this region. The choice of control points 1 and 5 here was largely based on their camber like behavior. A complete design and optimization should include all the relevant control points (e.g., control points 1, 2, 4, and 5). For geometries with large number of control points, in order to contain the computational costs within a reasonable range, a criteria for selecting the most influential control points for optimization purposes should be implemented. This decision could be based on the already known sensitivity coefficients, where control points having the largest coefficients could be chosen as design parameters. Secondly, the optimum wing-section of Fig. 6.24 is only valid for this particular example and design range. As a direct consequence of the non-linear nature of governing equations and their sensitivity coefficients, the validity of this optimum design would be restricted to a very small range of the original design parameters. The best estimate for this range would be the finite-difference step size used to validate the sensitivity coefficients (i.e., 10^{-3} or less). All the wing-sections with the original control points within this range should conform to the optimum design of the Fig. 6.24, while keeping the grid and flow conditions fixed.

Table 6.6 Lift and Drag sensitivities with respect to vector of grid parameters $\mathbf{X}_D$

Generic Wing-Section	Direct Approach	
Design Parameters:	$\frac{\partial C_L}{\partial X_G}$	$\frac{\partial C_D}{\partial X_G}$
X_1	-0.297	$-3.63\text{x}10^{-2}$
Y_1	-5.107	0.549
X_5	0.15	$-2.04\text{x}10^{-2}$
Y_5	2.609	0.287

Table 6.7 Comparison of initial and optimized performance variables

Performance Variables	Initial Design	Optimum Design	Percent Change
C_L	0.402	0.845	+110.1
C_D	0.063	0.043	−31.7
Lift/Drag Ratio	6.38	19.65	+208

Table 6.8 Comparison of initial and optimized design parameters

Design Parameters	Initial Design	Optimum Design	Percent Change
X_1	0.5	0.374	−25.2
Y_1	0.2	0.134	−33
X_5	0.5	0.414	−17.2
Y_5	0.05	0.069	+38

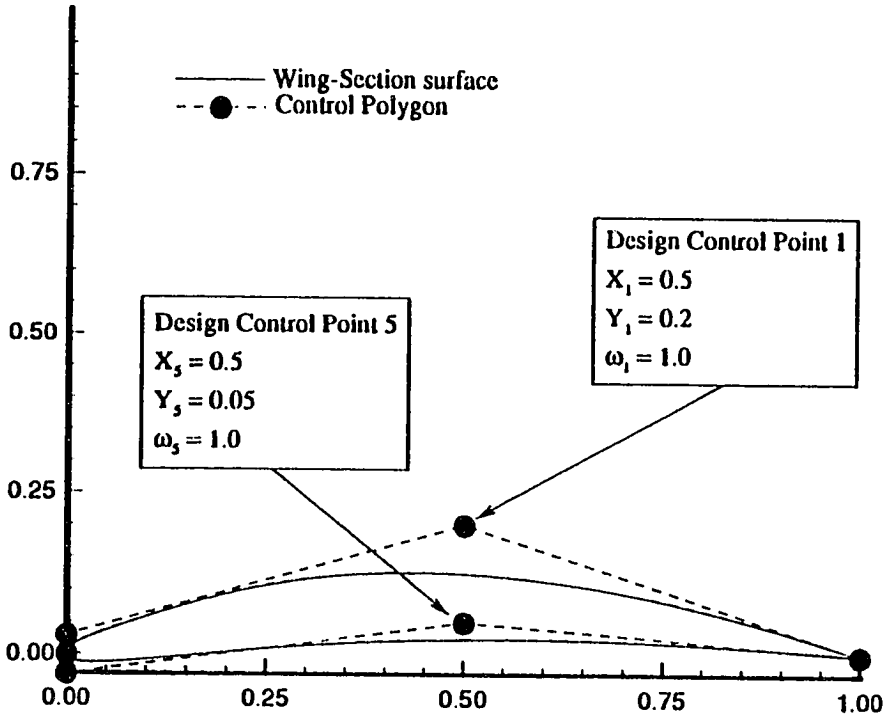

Fig. 6.19 Design parameters using seven control points NURBS representation of wing-section (option 3).

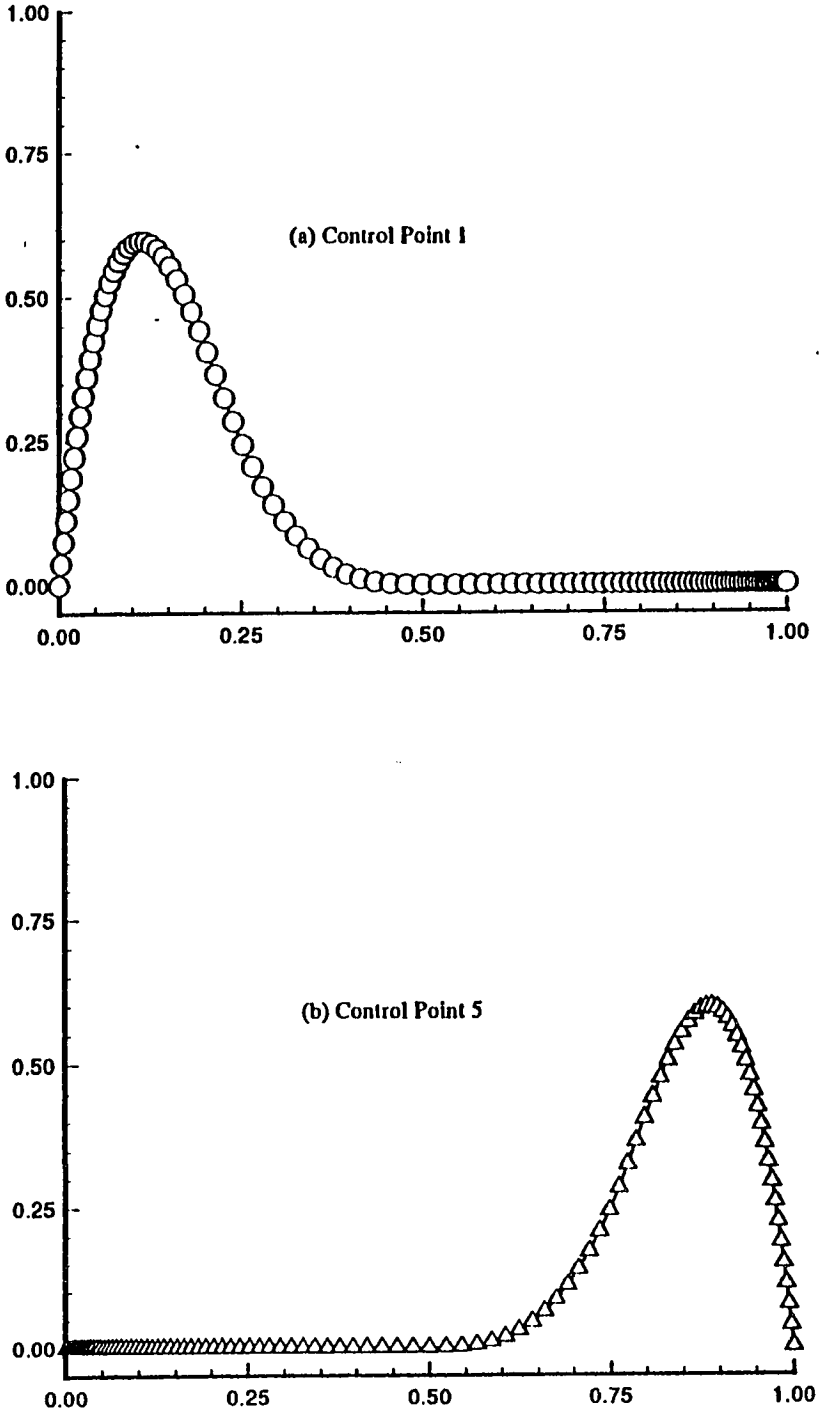

Fig. 6.20 Cubic basis function for control points 1 and 5.

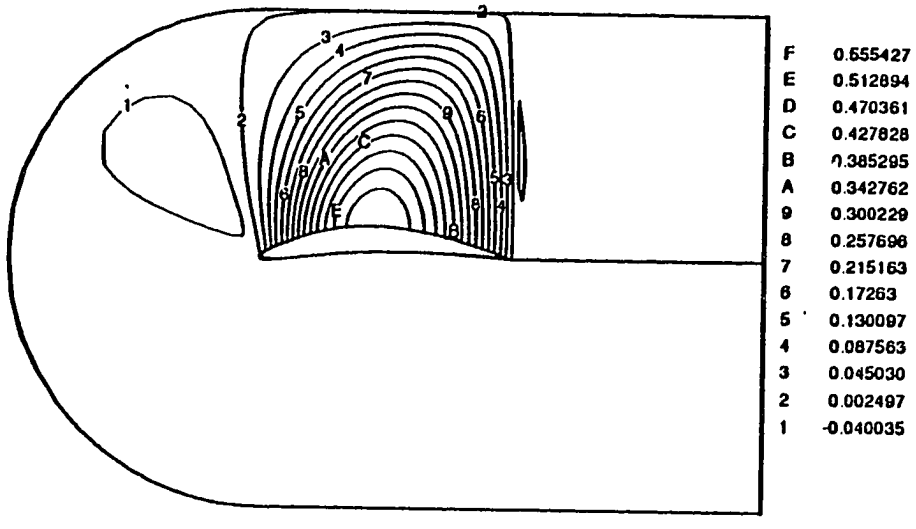

(a) Y-Coordinate

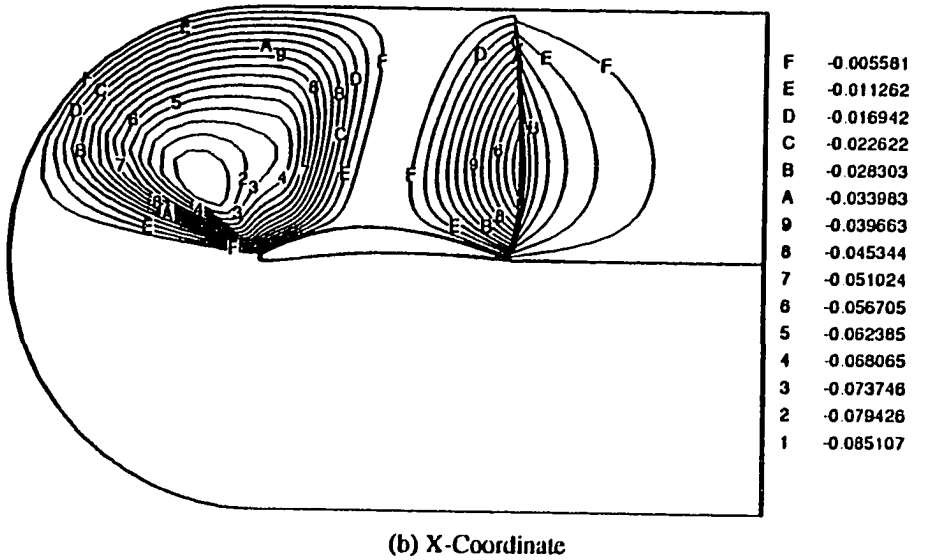

(b) X-Coordinate

Fig. 6.21 Coordinate sensitivity with respect to Y_1.

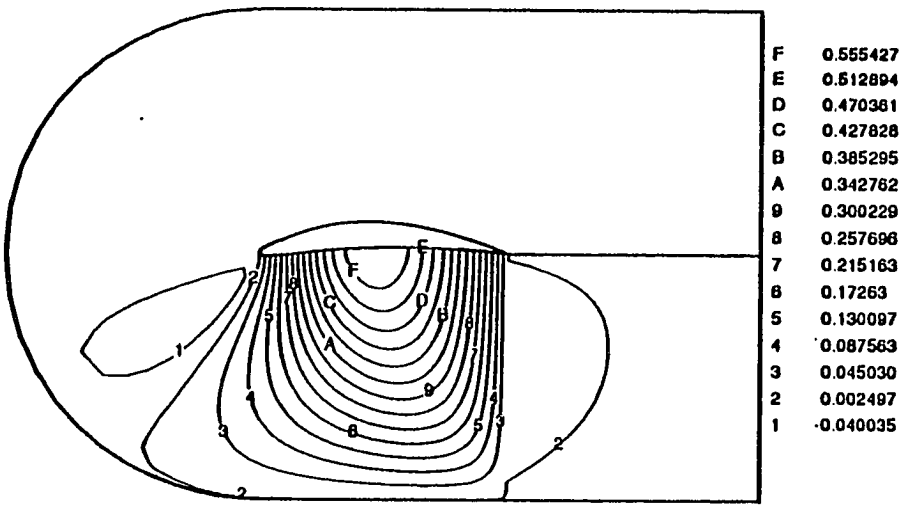

(a) Y-Coordinate

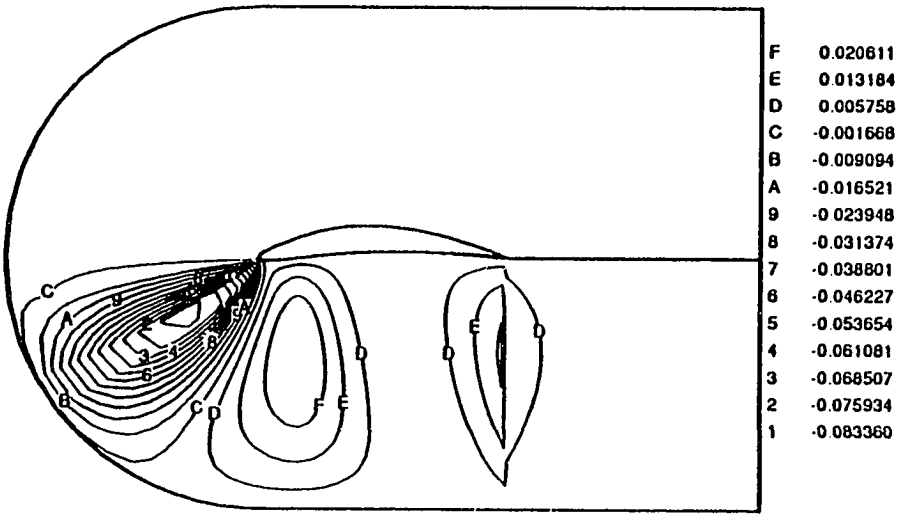

(b) X-Coordinate

Fig. 6.22 Coordinate sensitivity with respect to Y_5.

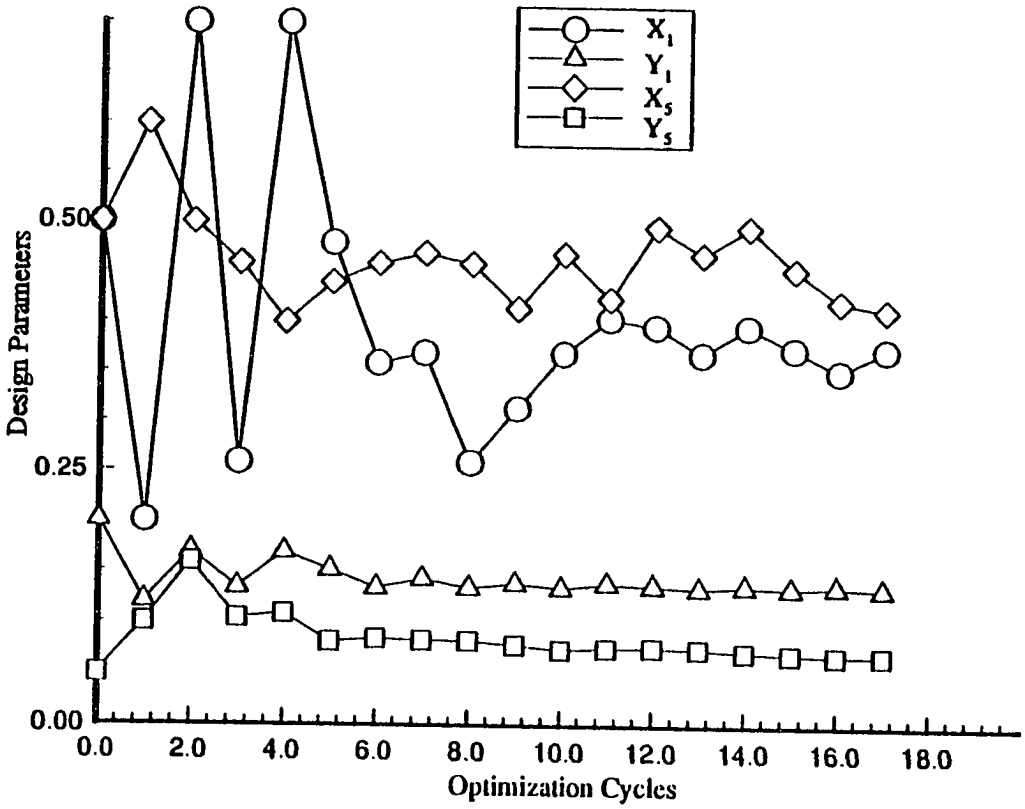

Fig. 6.23 Optimization cycle convergence history.

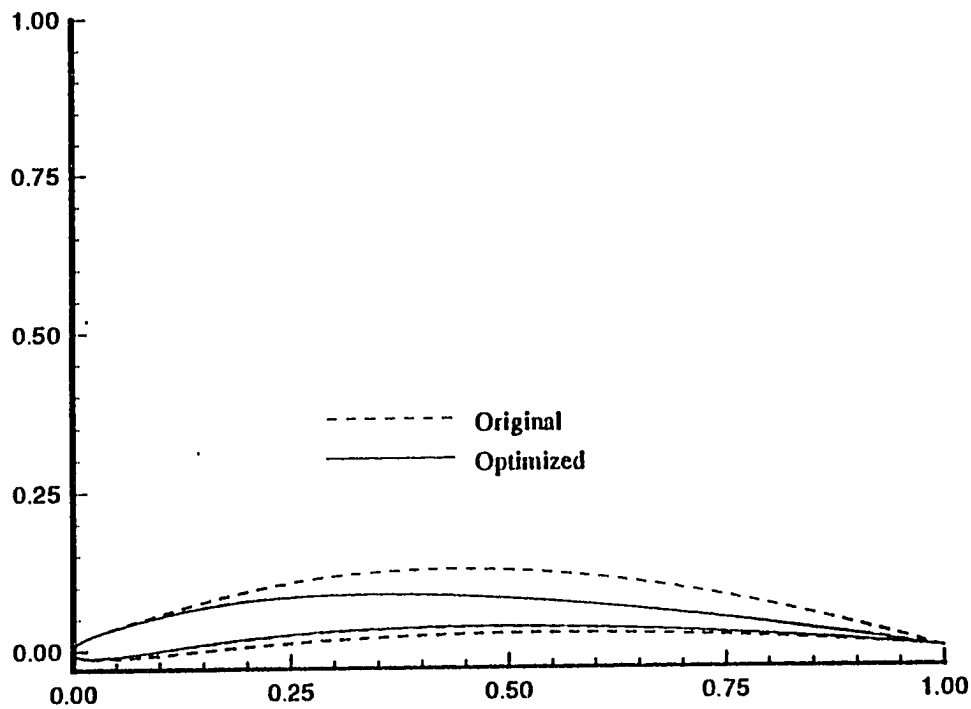

Fig. 6.24 Original and optimized wing-section.

Chapter 7

CONCLUSIONS AND RECOMMENDATIONS

An algorithm is developed to obtain the grid sensitivity with respect to design parameters for aerodynamic optimization. The algebraic Two-Boundary Grid Generation (TBGG) scheme has been directly differentiated with respect to design parameters. This formulation has the benefits of being exact, efficient, and inexpensive. The methodology is applied first to a symmetrical wing-section where the grid sensitivity coefficients have been validated by comparing well with finite difference approach (case 1). The wing-section geometry is defined either analytically using a combination of camber and thickness distributions, or geometrically using the NURBS approximation of the surface. The next test case involving a cambered wing-section is devised to couple the present grid sensitivity module with the newly developed flow analysis and sensitivity module of Taylor et al. [13], case 2. The aerodynamic sensitivity coefficients again compared well with finite difference results verifying the accuracy of grid sensitivity coefficients and their flow counterparts. Another application of this scheme, grid sensitivity with respect to grid parameters, has been obtained for grid-optimization purposes. The algorithm is then used for the main application, which is to optimize a generic wing-section using geometric NURBS parameterization of the surface (case 3). A substantial increase in aerodynamic performance variables enforces the feasibility of this approach for high level design and optimization.

It is evident that grid sensitivity plays a significant role in the aerodynamic optimization process. The algebraic grid generation scheme presented here intended

to demonstrate the elements involved in obtaining the grid sensitivity from an algebraic grid generation system. Each grid generation formulation requires considerable analytical differentiation with respect to parameters which control the boundaries as well as the interior grid. It is implied that aerodynamic surfaces, such as a wing-section considered here, should be parameterized in terms of design parameters. Due to the high cost of aerodynamic optimization process, it is imperative to keep the number of design parameters as low as possible. Analytical parameterization, although facilitates this notion, has the disadvantage of being restricted to simple geometries. A geometric parameterization such as NURBS, with local sensitivity, has been advocated for more complex geometries.

Future investigations should include the implementation of present approach using larger grid dimensions, adequate to resolve full physics of viscous flow analysis. A grid optimization mechanism based on grid sensitivity coefficients with respect to grid parameters should be included in the overall optimization process. An optimized grid applied to present geometry, should increase the quality and convergence rate of flow analysis within optimization cycles. Other directions could be establishing a link between geometric design parameters (e.g., control points and weights) and basic physical design parameters (e.g., camber, thickness). This would provide a consistent model throughout the analysis which could easily be modified for optimization. Also, the effects of including all the relevant control points on the design cycles should be investigated. Another contribution would be the extension of the current algorithm to three-dimensional space for complex applications. For three-dimensional applications, even a geometric parameterization of a complete aerodynamic surface can require a large number of parameters for its definition. A hybrid approach can be selected when certain sections or skeletal parts of a surface are specified analytically or with NURBS and interpolation formulas are used for intermediate surfaces.

REFRENCES

1. Sobieszczanski-Sobieski, J. "The Case for Aerodynamic Sensitivity Analysis," Paper presented to NASA/VPI SSY Symposium on Sensitivity Analysis in Engineering, September 25-26, 1986.

2. Sobieszczanski-Sobieski, J. "Sensitivity Analysis and Multidisciplinary Optimization for Aircraft Design : Recent Advances and Results," NASA TM-100630, July 1988.

3. Yates, E.C., "Aerodynamic Sensitivities from Subsonic, Sonic, and Supersonic Unsteady, Nonplanar Lifting-Surface Theory," NASA TM-100502, September 1987.

4. Murthy, D.V., and Kaza, K.V., "Application of a Semianalytical Techniques for Sensitivity Analysis of Unsteady Aerodynamic Computations," AIAA Paper 88-2377, April 1988.

5. Grossman, B., Haftka, R.T., Kao, P.J., Polen, D.M., Rais-Rohani, M., Sobieszcz anski-Sobieski, J., "Integrated Aerodynamic-Structural Design of a Transport Wing," AIAA Paper 89-2129, AIAA/AHS/ASEE Aircraft Design, Systems and Operations Conference, Seattle, WA, July 31 - August 2, 1989.

6. Livne, E., Schmit, L.A., and Friedmann, P., "An Integrated Approach to the Optimum Design of Actively Controlled Composite Wings," AIAA Paper 89-1268, *Proceedings of the AIAA/ASME/ASCE/AHS/ASC 30th Structural, Structural Dynamics and Materials Conference*, Mobile AL, April 3-5, 1989, Part II, pp. 933-945.

7. Elbanna, H., and Carlson, L., "Determination of Aerodynamic Sensitivity Coefficients in the Transonic and Supersonic Regimes," AIAA Paper 89-0532, January 1989.

8. Elbanna, H., and Carlson, L., "Determination of Aerodynamic Sensitivity Based on the Three-Dimensional Full Potential Equations," AIAA Paper 92-2670, January 1992.

9. Baysal, O., and Eleshaky, M. E., "Aerodynamic Sensitivity Analysis Methods for the Compressible Euler Equations,"Recent Advances in Computational Fluid Dynamics, (ed. O. Baysal), ASME-FED Vol. 103, 11th Winter Annual Meeting, November, 1990, pp. 191-202. Also appeared in *Journal of Fluids Engineering*, Volume 113, December 1991, pp. 681-688.

10. Baysal, O., and Eleshaky, M. E., "Aerodynamic Design Optimization Using Sensitivity Analysis and Computational Fluid Dynamics," AIAA Paper 91-0471, January 1991. Also appeared in *AIAA Journal*, Volume 30, Number 3, March 1992, pp.718-725.

11. Eleshaky, M.E., and Baysal, O., "Aerodynamic Shape Optimization Via Sensitivity Analysis on Decomposed Computational Domains," 4th AIAA/USAF/NASA/OAI Symposium on Multidisciplinary Analysis and Optimization, Part 1, September 21-23, 1992, Cleveland, OH, pp. 98-109.

12. Taylor, A. C., III, Hou, G. W., and Korivi, V. M., "Sensitivity Analysis Applied to the Euler Equations : A Feasibility Study with Emphasis on Variation of Geometric Shape," AIAA Paper 91-0173, January 1991.

13. Taylor, A. C., III, Hou, G. W., and Korivi, V. M., " Sensitivity Analysis, and Design Optimization For Internal and External Viscous Flows," AIAA Paper 91-3083, September 23-25, 1991, Baltimore, MD.

14. Burgreen, G.W., Baysal, O., and Eleshaky, M. E., "Improving the Efficiency of Aerodynamic Shape Optimization Procedures ," AIAA Paper 92-4697, 4th AIAA/USAF/NASA/OAI Symposium on Multidisciplinary Analysis and Optimization, Part 1,September 21-23, 1992, Cleveland, OH, pp. 87-97.

15. Hutchison, M., Unger, E., Mason, W., Grossman, B., and Haftka, R., "Variable-Complexity Aerodynamic Optimization of an HSCT Wing using Structural Wing-Weight Equations," AIAA Paper 92-0212, 30th Aerospace Sciences Meeting and Exhibit, Reno, NV, January 6-9, 1992.

16. Hutchison, M.G. , Mason, W.H., Grossman, B., and Haftka, R.T., "Aerodynamic Optimization of an HSCT Configuration Using Variable-Complexity Modeling," AIAA Paper 93-0101, 31th Aerospace Sciences Meeting and Exhibit, Reno, NV, January 11-14, 1993.

17. Verhoff, A., Stookesberry, D., and Cain, A.B., "An Efficient Approach to Optimal Aerodynamic Design Part 1: Analytic Geometry and Aerodynamic Sensitivities," AIAA Paper 93-0099, 31th Aerospace Sciences Meeting and Exhibit, Reno, NV, January 11-14, 1993.

18. Verhoff, A., Stookesberry, D., and Cain, A.B., "An Efficient Approach to Optimal Aerodynamic Design Part 2: Implementation and Evaluation," AIAA Paper 93-0100, 31th Aerospace Sciences Meeting and Exhibit, Reno, NV, January 11-14, 1993.

19. Shubin, G.R., "Obtaining Cheap Optimization Gradients from Computational Aerodynamics Codes," *Applied Mathematics and Statics Technical Report*, AMS-TR-164, Boeing Computer Services, Seattle, WA, June 1991.

20. Somayajula, G., "Grid sensitivity analysis," *Finite Element in Analysis and Design*, Elsevier Science Publishers B.V., 1991, pp. 307-315.

21. Sadrehaghighi, I., Smith, R.E., Tiwari, S.N., "An Analytical Approach To Grid Sensitivity Analysis," AIAA Paper 92-0660, 30th Aerospace Sciences Meeting and Exhibit, Reno, NV, January 6-9, 1992.

22. Sadrehaghighi, I., Smith, R.E., Tiwari, S.N., "Grid and Design Variables Sensitivity Analysis For NACA Four-Digit Wing-Sections," AIAA Paper 93-0195, 30th Aerospace Sciences Meeting and Exhibit, Reno, NV, January 11-14, 1993.

23. Smith, R. E., and Sadrehaghighi, I., "Grid Sensitivity in Airplane Design," *Proceedings of the fourth International Symposium on Computational Fluid Dynamics*, Vol. 1, September 9-12, 1991, Davis, California, pp. 1071-1076.

24. Smith, R.E., and Kerr, P.A., "Geometric Requirements for Multidisciplinary Analysis of Aerospace-Vehicle Design," 4th Symposium on Multidisciplinary Analysis and Optimization, AIAA Paper 92-4773, Cleveland, OH, September 21-23, 1992.

25. Abbott, I.H., and Von Doenhoff, A.E., *Theory of Wing Sections*, Dover, NewYork., 1959.

26. Piegle, L., "On NURBS: A Survey," *IEEE Computer Graphic and Application*, Volume II, No. 1, January 1991, pp. 55-71.

27. Atwood, C.A., and Vogel, J.M., "Surface Grid Generation for Flowfield Applications Using B-Spline Surfaces," AIAA Paper 89-2177, 1989.

28. Tiller, W., "Rational B-Splines for Curve and Surface Representation," *Computer Graphics and Applications*, Volume 3, N0. 10, September 1983, pp. 61-69.

29. Abolhassani, J.S., Sadrehaghighi, I., Smith, R.E., and Tiwari, S.N., "Application of Lagrangian Blending Function for Grid Generation Around Airplane Geometries," *Journal of Aircraft*, Volume 27, No. 10, October 1990, pp. 873-877.

30. Huband, G. W., Shang, J. S., and Aftosmis, M. J., "Numerical Simulation of an F-16A at Angle of Attack," *J. Aircraft*, Vol. 27, pp. 886-892, October 1990.

31. Corcoran, E., "Calculating Reality," *Scientific American*, pp. 101-109, January 1990.

32. Eriksson, L.E., "Three-Dimensional Spline-Generated Coordinate Transformation for Grids Around Wing-Body Configurations," Numerical Grid Generation Techniques, NASA CP 2166, March 1980.

33. Thomas, J.L., and Salas, M.D., "Far-Field Boundary Conditions for Transonic Lifting Solutions to the Euler Equations," AIAA Paper 85-0020, AIAA 23rd Aerospace Sciences Meeting, Reno NV, January 14-17, 1985.

34. Kathong, M., "Application of Advanced Grid Generation Techniques for Flow Field Computations about Complex Configurations," Ph.D. Dissertation, Old Dominion University, Norfolk, VA, July 1988.

35. Thompson, J.F., Warsi, Z.U.A., and Mastin, C.W., *Numerical Grid Generation: Foundations and Applications*, North-Holland, NewYork, 1985.

36. Gordon, W. N., and Hall, C. A., "Construction of Curvilinear Coordinate Systems and Application to Mesh Generation," *International Journal for Numerical Methods in Engineering*, Vol. 7, pp 461-477, 1973.

37. Eiseman, P.R., "A Multi-Surface Method of Coordinate Generation," *Journal of Computational Physics*, Volume 33, No. 1, pp. 118-150, 1979.

38. Smith, R.E., "Two-Boundary Grid Generation for Solution of the Three - Dimensional Navier-Stokes Equations," NASA TM-83123, May 1981.

39. Sorenson, R., "A Computer Program to Generate Two-Dimensional Grids About Airfoils and Other Shapes by the use of Poisson's Equation," NASA TM-81198, May 1980.

40. Thompson, J., "A Composite Grid Generation Code for General 3D Regions-the EAGLE Code," *AIAA Journal*, Volume 26, No. 3, March 1988.

41. Steinbrenner, J., Chawner, J., and Fouts, C., "The GRIDGEN 3D Multiple Block Grid Generation System," WRDC TR 90-3022, July 1990.

42. Akdag, V., and Wulf, A., "Integrated Geomtery and Grid Generation System for Complex Configurations," NASA CP 3143, Apri 1992.

43. Eiseman, P. R., and Smith, R. E., "Applications of Algebraic Grid Generation , Applications of Mesh Generation to Complex 3-D Configurations," *Advisory Group for Aerospace Research and Development* (AGARD)-CP-464, pp. 4-1-12, 1989.

44. Abolhassani, J.S., and Smith, R.E., "Three-Dimensional Grid Generation About a Submarine," *Numerical Grid Generation in Computational Fluid Mechanics*, Pineridge Press Limited, Swansea, UK, pp. 505-515,1988.

45. Smith, R. E., and Eriksson, L. E., "Algebraic Grid Generation," *Computational Methods in Applied Mechanics Engineering*, Vol. 64, pp 285-300 ,June 1987.

46. Smith, R. E., and Wiese, M. R., "Interactive Algebraic Grid-Generation Technique," NASA Technical Paper 2533, March 1986.

47. Vinokur, M., "On One-Dimensional Stretching Functions for Finite-D ifference Calculations," *Journal of Computational Physics*, No. 50, April 1983, pp. 215-234.

48. Eiseman, P.R., "Grid Generation for Fluid Mechanics Computations," *Annual Review of Fluid Mechanics*, Volume 17, May 1985, pp.487-522.

49. Erickson, L.E., "Flow Solutions on a Dual-Block Grid Around an Airplane," *Computational Methods in Applied Mechanics Engineering*, Volume 64, June 1987, pp.79-93.

50. Bezier, P., "*Numerical Control: Mathematics and Applications*," John Wiley and Son, 1970.

51. Rogers, D.F. and Adams, J.A., "*Mathematical Elements for Computer Graphics*", Mc Graw-Hill, 1976.

52. Anderson, D.A., Tannehill, J.C., and Pletcher, R.H., " *Computational Fluid Mechanics and Heat Transfer*," Hemisphere Publishing Corporation, New York, 1984.

53. Van Leer, B., " Flux-Vector Splitting for the Euler Equations," *Institute for Computer Applications in Science and Engineering* (ICASE) Report 82-30, September 1982.

54. Venkatakrishnan, V., " Newton Solution of Inviscid and Viscous Problems," *AIAA Journal*, Volume 27, No. 7, July 1989, also AIAA Paper 88-0413, January 1989.

55. Vanderplaats, G.N., " An Efficient Feasible Direction Algorithm for Design Synthesis," *AIAA Journal*, Volume 22, No. 11, October 1984, pp. 1633-1640.

56. Vanderplaats, G.N., " ADS - A Fortran Program for Authomated Design Synthesis," NASA CR-177985, September 1985.

APPENDIX A

TRANSFINITE INTERPOLATION WITH LAGRANGIAN BLENDING FUNCTION

A.1 Surface Grid Generation

The dual-block grid topology of Fig. 3.3 has been selected and applied to a generic airplane configuration. The next step is to generate the solid surfaces either by a set of analytical functions or by a set of cross-sections. The former requires no interpolation while the latter requires some sort of bi-directional interpolation. A powerful interpolation choice would be the use of the NURBS function for intermediate surfaces. For this geometry, a fuselage with circular cross-section has been devised using polar coordinates. The wing and tails are derived by using NACA four-digit wing-sections as a selection of cross-sections and then interpolate for intermediate surfaces. Figure A.1 shows the corresponding surface grid. For remaining non-physical surfaces, the best approach is to decompose the region to a number of sub-regions as illustrated in Fig. A.2. Although this sub-division is arbitrary, it is a good idea to sub-divide along computational coordinates. The grid for each sub-region, $\vec{F}(\xi,\eta) = \{x(\xi,\eta), y(\xi,\eta)\}^T$, can be computed using a two-step Transfinite Interpolation as

$$\vec{F}_1(\xi,\eta) = \sum_{\ell=1}^{L}\sum_{n=0}^{P} \alpha_\ell^{(n)}(\xi)\vec{A}_\ell^{(n)}(\eta), \qquad (A.1)$$

$$\vec{F}(\xi,\eta) = \vec{F}_1(\xi,\eta) + \sum_{\ell=1}^{M}\sum_{n=0}^{Q} \beta_\ell^{(n)}(\eta)\left[\vec{B}_\ell^{(n)}(\xi) - \frac{\partial^n \vec{F}_1}{\partial \eta^n}(\xi,\eta_\ell)\right], \qquad (A.2)$$

where the $\vec{A}_\ell^n$ and $\vec{B}_\ell^n$ are the known coordinate lines on the surface with their derivatives,

$$\frac{\partial^n \vec{F}}{\partial \xi^n}(\xi_\ell, \eta) = \vec{A}_\ell^n(\eta), \quad \ell = 1, 2, \ldots, L, \quad n = 0, 1, \ldots, P, \tag{A.3}$$

$$\frac{\partial^n \vec{F}}{\partial \eta^n}(\xi, \eta_\ell) = \vec{B}_\ell^n(\xi), \quad \ell = 1, 2, \ldots, M, \quad n = 0, 1, \ldots, Q, \tag{A.4}$$

and $\alpha_\ell^{(n)}(\xi)$ and $\beta_\ell^{(n)}(\eta)$ are the univariant blending functions,

$$\alpha_\ell^{(n)}(\xi), \quad \ell = 1, 2, \ldots, L, \quad n = 0, 1, \ldots, P, \tag{A.5}$$

$$\beta_\ell^{(n)}(\eta), \quad \ell = 1, 2, \ldots, M, \quad n = 0, 1, \ldots, Q. \tag{A.6}$$

These functions are subjected to the following conditions

$$\frac{\partial^m \alpha_\ell^{(n)}(\xi_i)}{\partial \xi^m} = \delta_{\ell,i}\delta_{n,m}, \tag{A.7}$$

$$\frac{\partial^m \beta_\ell^{(n)}(\eta_i)}{\partial \eta^m} = \delta_{\ell,i}\delta_{n,m}. \tag{A.8}$$

These conditions permit to reproduce the input boundaries.

Selection of the blending function depends on the number of specified boundaries. One choice for the blending function is the Lagrangian interpolation which satisfies the Cardinal conditions. For example, if some lines in the ξ- direction are given at $\xi_1, \xi_2, \ldots, \xi_n$, then the blending function α can be defined as,

$$\alpha_\ell(\xi) = \prod_{\substack{j=1 \\ j \neq \ell}}^{n} \frac{(\xi - \xi_j)}{(\xi_\ell - \xi_j)}. \tag{A.9}$$

If only two boundaries are defined in one computational direction, then the Lagrangian interpolation would convert to a simple linear interpolation

$$\alpha_1(\xi) = \frac{(\xi_2 - \xi)}{(\xi_2 - \xi_1)}, \qquad \alpha_2(\xi) = \frac{(\xi - \xi_1)}{(\xi_2 - \xi_1)}. \tag{A.10}$$

This works if the boundaries do not contain sharp discontinuities. Otherwise, these discontinuities will propagate into the interior regions. One way to solve this problem

is to construct a blending function that has very small value away from the boundaries. For example, the following blending functions have these criteria.

$$\alpha_1(\xi) = \frac{e^{K\frac{(\xi_2-\xi)}{(\xi_2-\xi_1)}} - 1}{e^K - 1}, \qquad \alpha_2(\xi) = \frac{e^{K\frac{(\xi-\xi_1)}{(\xi_2-\xi_1)}} - 1}{e^K - 1} \tag{A.11}$$

where K is a negative number greater than one. The larger the K is the lesser the discontinuity will propagate. A similar blending function can be constructed for the η direction. Some results of this formulation applied to symmetry and outer boundary planes are shown in Figs. A.3 and A.4.

A.2 Volume Grid Generation

In general, decomposition of the physical domain produces several blocks. Each block is usually defined by six sides, and each side can be defined by either a surface, plane, line, or a point. If one side of a block collapses to a line or a point, then there would be a singularity in the block. In some instances, a block may have been defined by more or less than six surfaces. Once the surface are defined, the interior grid can be computed by any standard grid generation technique. In this study, an oscillatory- transfinite interpolation has been used to generate the interior grid points.

Once the boundary surfaces ($\vec{F}(\xi,\eta,\zeta)$) are known, then it is possible to generate the interior grid by transfinite interpolations. In a general form, the transfinite interpolation (or univariant interpolation) can be expressed by a vector $\vec{F}(\xi,\eta,\zeta)$ as

$$\vec{F}(\xi,\eta,\zeta) = \{x(\xi,\eta,\zeta), \quad y(\xi,\eta,\zeta), \quad z(\xi,\eta,\zeta)\}^T, \tag{A.12}$$

$$\vec{F}_1(\xi,\eta,\zeta) = \sum_{\ell=1}^{L}\sum_{n=0}^{P} \alpha_\ell^{(n)}(\xi)\vec{A}_\ell^{(n)}(\eta,\zeta), \tag{A.13}$$

$$\vec{F}_2(\xi,\eta,\zeta) = \vec{F}_1(\xi,\eta,\zeta) + \sum_{\ell=1}^{M}\sum_{n=0}^{Q} \beta_\ell^{(n)}(\eta)\left[\vec{B}_\ell^{(n)}(\xi,\zeta) - \frac{\partial^n \vec{F}_1}{\partial\eta^n}(\xi,\eta_\ell,\zeta)\right], \tag{A.14}$$

$$\vec{F}(\xi,\eta,\zeta) = \vec{F}_2(\xi,\eta,\zeta) + \sum_{\ell=1}^{N}\sum_{n=0}^{R} \gamma_\ell^{(n)}(\zeta)\left[\vec{C}_\ell^{(n)}(\xi,\eta) - \frac{\partial^n \vec{F}_2}{\partial\zeta^n}(\xi,\eta,\zeta_\ell)\right], \qquad (A.15)$$

where the $\vec{A}_\ell^n$, $\vec{B}_\ell^n$ and $\vec{C}_\ell^n$ are the known surface location and their derivatives. Figure A.5 displays the interior grid for a constant-I surface.

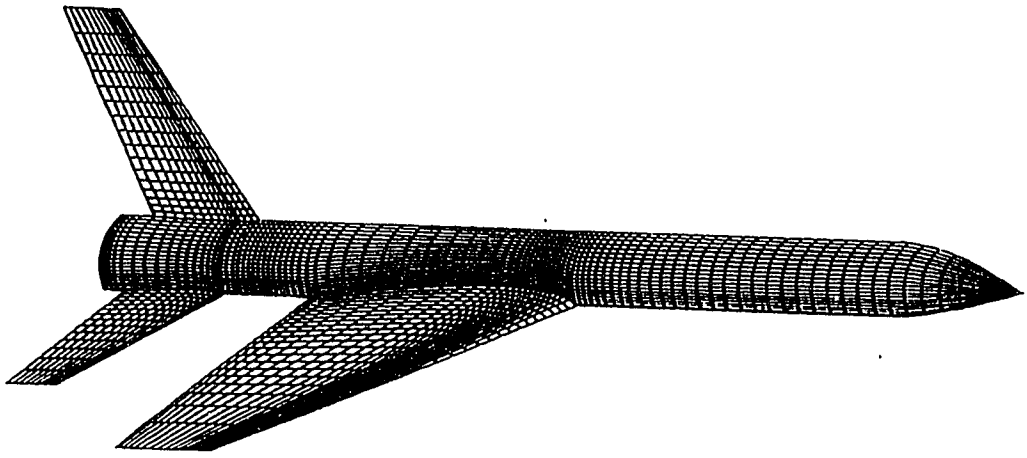

Fig. A.1 Grid on the solid (physical) surfaces.

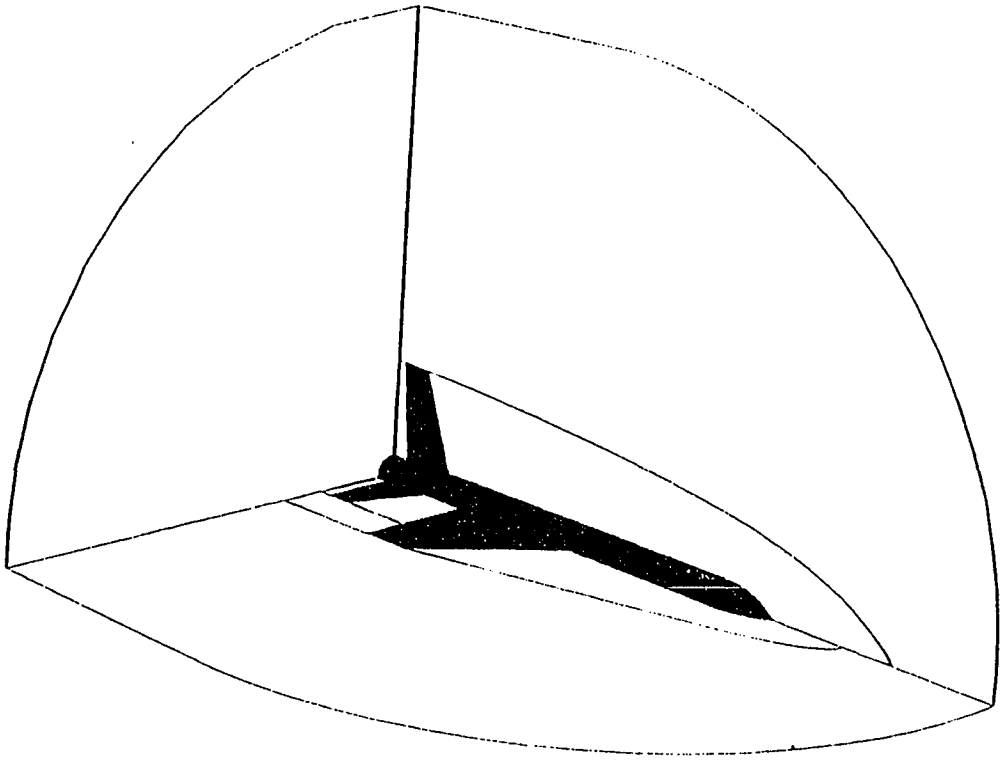

Fig. A.2 Domain decomposition.

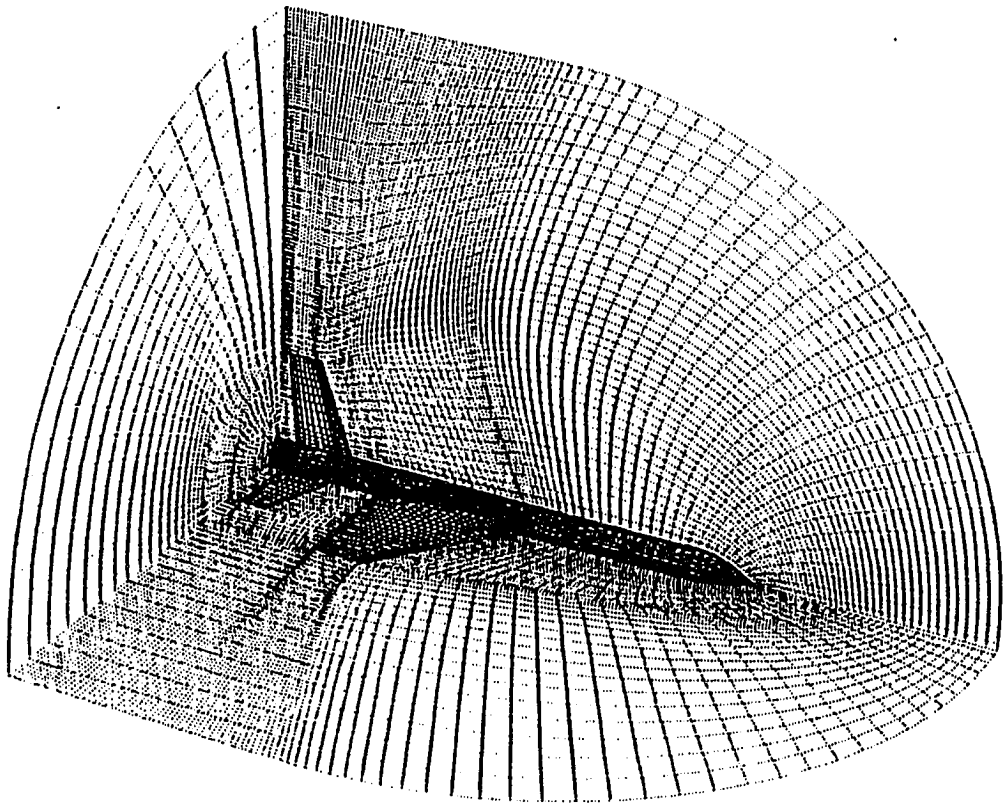

Fig. A.3 Grid on the physical and non-physical surfaces.

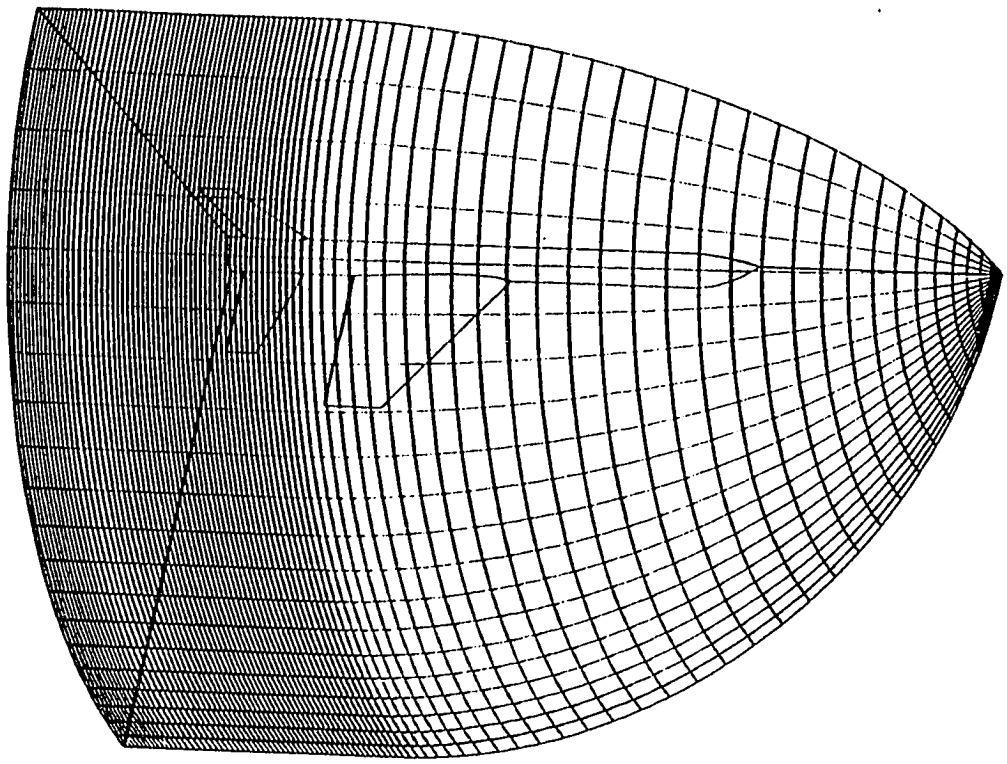

Fig. A.4 Grid on the outer boundary.

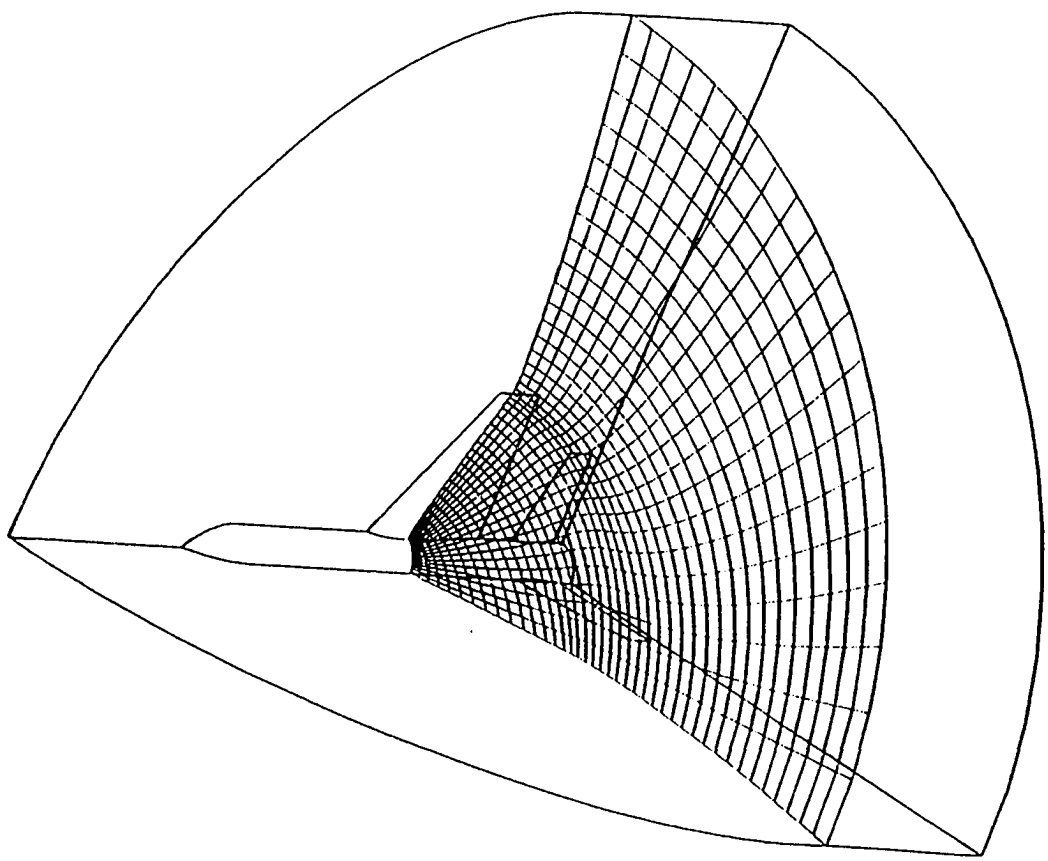

Fig. A.5 Volume grid (constant-I) surface.